THREE DIMENSIONAL CELL CULTURE:

A WINDOW INTO TRANSPORT OF

NANOMEDICINE IN TUMOR TISSUE

by

Yichun Wang

A dissertation submitted in partial fulfillment
of the requirements for the degree of
Doctor of Philosophy
(Biomedical Engineering)
in the University of Michigan
2016

Doctoral committee:

Professor Nicholas A. Kotov, Chair

Professor Henry Y. Wang

Associate Professor Xueding Wang

Associate Professor Zhen Xu

Dedication

To my mother, Cuihong Zhu, and my husband, Philip Lindh

for their unconditional love

ACKNOWLEDGEMENTS

This dissertation would not have been possible without the support and guidance from many individuals. I would like to express the appreciation to all of them.

First, I would like to thank my advisor, Professor Nicholas Kotov, for his support and guidance. He is a tremendous mentor with deep thoughts, creativity and enthusiasm. His intelligence and knowledge have always given the endless inspiration to me. I deeply appreciate his encouragements and understanding throughout the time when I'm in the University of Michigan and will always appreciate the opportunity to do Ph.D. here.

I would also like to thank my committee, Prof. Henry Wang, Zhen Xu and Xueding Wang for taking time to discuss my research. I am very grateful for their advice and assistance not only on my dissertation but also the future career.

I would like to thank the current and past members of the Kotov group for their friendship and scientific advice. I would especially thank Joong Hwan, Terry and Carlos who have shared so many laughs with me. I thank all the Chinese friends in Ann Arbor who always provided the warmth and help, which made me feel this

is my hometown. I also express the gratitude to my best friends in China, Jing, Jiawei, Lin and Cuihua in China who always listened to me and encouraged me.

Lastly, I would like to thank my mother and my husband. Your support and love have been always so sweet and encouraging throughout the years. I am lucky and grateful to have both of you in my life.

PREFACE

This dissertation contains the following published articles and manuscript in preparation:

- **Yichun Wang**, Joong Hwan Bahng, Quantong Che, Jishu Han and Nicholas A. Kotov. Anomalous Diffusion of Targeted Carbon Nanotubes in Cellular Spheroids. ACS Nano 2015 9(8):8231-8
- **Yichun Wang** and Nicholas A. Kotov. Transport of Carbon Nanotubes in Cellular Spheroid: A Simulation Study. In preparation.
- **Yichun Wang**, Joong Hwan Bahng and Nicholas A. Kotov. Hepatic differentiation of controlled-size embryoid bodies derived by inverted colloidal crystal scaffolds. In preparation to submit to Organ-on-a-chip.
- **Yichun Wang**, Meghan Cuddihy, Edward Jan and Nicholas A. Kotov. Layer-by-Layer Bone Mimetic Coating of Three-Dimensional Scaffolds Stimulated Chondrogenic Differentiation of Bone Marrow Stromal Cells. In preparation to submit to Biomaterials.
- Meghan J. Cuddihy, **Yichun Wang**, Charles Machi, Joong Hwan Bahng, Nicholas A. Kotov. Replication of Bone Marrow Differentiation Niche: Comparative Evaluation of Different Three-Dimensional Matrices. Small 2013 Volume 9, Issue 7, 1008–1015.

TABLE OF CONTENTS

LIST OF FIGURES

LIST OF TABLES

LIST OF ABBREBATIONS

AuNR Gold nanorod

CNT Carbon nanotube

EB Embryoid Body

ESC Embryonic Stem Cell

FITC Fluorescein isothiocyanate

GQD Graphene quantum dot

HF Hydrogen fluoride

ICC Inverted colloidal crystal

LBL Layer-by-layer

BMSC Bone marrow stromal cell

MC Monte carlo

NP Nanoparticle

PAS Periodic acid–Schiff

PDDA Poly diallyldimethylammonium –chloride

RhB Rhodamine B

SEM Scanning electron microscope

TGFβ1 Transforming growth factor beta 1

ABSTRACT

Recent growth in nanotechnology has been accelerating the identification and evaluation of new drug candidates. The development, optimization of nanomedicine and preclinical assessment of drug-induced toxicity as well as efficacy, is critical, but long and expensive. These studies are challenging due to the lack of test platforms that can incorporate sufficient human-relevant physiological complexity for reliable and standardized prediction of drug effects. Current preclinical drug testing, which rely predominantly on animal models, is expensive and has poor predictivity due to the variety of animals and limitation of imaging technologies. Two-dimensional (2D) cell cultures have also been used in the preclinical phase drug screening, however, they cannot adequately restore original cellular behaviors to nanomedicine in three-dimensional (3D) tissues. 3D cell culture techniques have enabled the real-time study of mammalian tissues within *ex vivo* models. These models with the ability to independently manipulate microenvironmental factors can be used to explore fundamental biological response to novel therapeutic nanoparticles and enable testing of novel therapeutic approaches.

Drug delivery and transport of nanomedicine through complex 3D tissues such as solid tumors can be adequately evaluated in specially prepared 3D cell culture as platform. This is an important consideration for pharmacodynamics

analysis to validate drug doses and administration regimens required to achieve desired therapeutic effects. In coupling with computational Monte-Carlo sampling and analysis of conditioned microenvironment, the standardized and uniform-sized liver tumor spheroids culture model in Inverted Colloidal Crystal (ICC) scaffolds *in vitro* could be used to identify or validate predictive drug transport and efficacy, while the transparency of the platform allowed convenient real-time monitoring of drug-cellular interaction. As a potential solution to improve the predictive power of *ex vivo* screening procedures, this dissertation established the experimental and conceptual framework for quantitative evaluation of drug delivery and transport in the tumor tissue *ex vivo* as a part of drug discovery, and explored a new opportunity of carbon nanotubes as a promising nano-sized carrier for drug delivery.

Besides the primary goal of drug delivery and transport in 3D complex, these models have been studied to generate replacement human tissues using patient-derived cells and/or stem cell. This is essential for future personalized drug screening and personalized medicine, as well as co-clinical trial applications with a patient's own cells adapted with stem cell techniques. It is able to develop patient-specific model for individualized study of drug safety and efficacy or drug–drug interactions. In this part of dissertation, ICC scaffolds with uniformly, controllable porous structure combined with a layer-by-layer (LBL) bone mimetic modification technique served as a platform for engineered stem cells towards optimal hepatic differentiation and hepatocyte formation for discovery of personalized drug testing.

Bone marrow stromal cells as supporting layer for stem cell culture was found interacting and influenced by surface properties of 3D matrices.

Overall this dissertation introduces a promising and standardized 3D cell culture platform established in ICC scaffolds coupling with computational simulation which substantiate the capability in a range of areas in preclinical drug discovery. This platform is a window to fundamental understanding of nanomedicine, as well as a practical and valuable tool for drug discovery regarding drug delivery and transport through complex 3D tissues, as well as development of personalized drug screening.

Chapter I

Introduction

1.1 Motivation

Nanotechnologies have been recognized as successful therapeutic interventions including various aspects from engineered drug delivery and localization to personalized medicine[1–4,5,6]. The advances such as unique optical properties and surface chemistry in nanomedicine are accelerating the identification and evaluation of these drug candidates[7,8,9–11]. Yet, as nanomedicine is developing, the concerns of drug side effect and failures associated with the new technology that are involved in the therapeutic procedure have been brought to public attentions. To transform these new therapeutic technologies into medical reality, explosive efforts have been accumulated on preclinical assessment and prediction regarding effectiveness and toxicities.[12] Whereas, the pharmaceutical industry is facing unprecedented challenges due to high costs and the inefficiency of novel drug research and development. [13] In addition, attrition aroused out of safety liabilities

observed in the clinical application are the major contributor to the rising costs and reduced productivity in the industry [14] because potential issues cannot be identified during preclinical development. These are the consequences of the long process[15] (**Figure 1.1a**) and poor prediction of existing preclinical models[16] (**Figure 1.1b**) which have led to demands for more accurate predictive tools.

Two-dimensional (2D) cell cultures as a conventional and convenient tool were therefore often accepted for toxicity and targeting studies[17,18]. However, they are not able to adequately represent tissue morphology to replicate realistic conditions. Test Animal models, such as rats, mice and hamsters, have been widely used regarding different nanoparticles (NPs). The existing data were obtained for

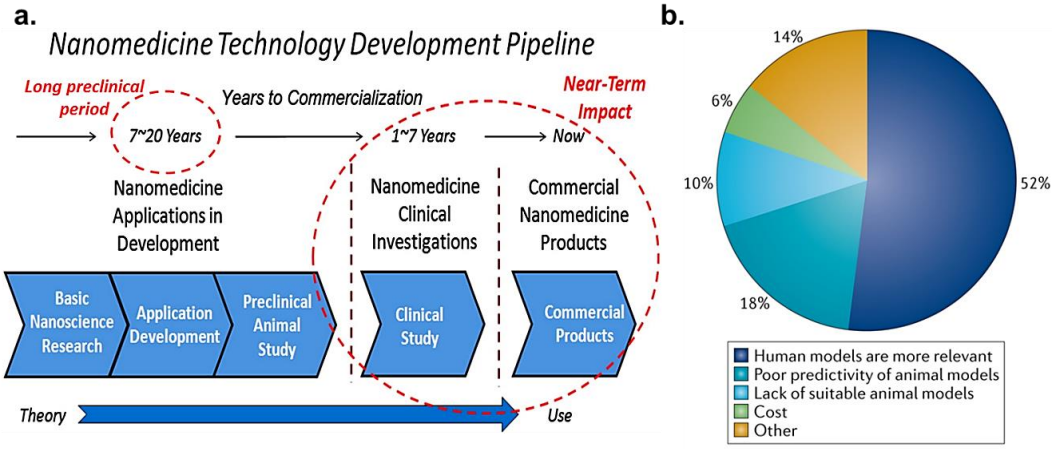

Figure 1.1 The predictivity of preclinical models including human tissue-based approaches instead of animal models shows the necessarity of new preclinical approaches for pharmacology studies.[15,16,19]

various tumors, therapeutic, modalities, administration routes, doses, however, quantification methods and numerous unexpected properties of NPs cannot be reliably measured and standardized by such animal models[18,19]. For instance, the numbers of mice in published studies are too small, making it difficult to obtain statistically significant comparisons; the experimental conditions, such as relative tumor size at the start of treatment, are not comparable to those in the human population; moreover, the drug doses used and tolerated in mice are also too divergent for use in people. Therefore, the results from classic tests of toxicity and efficiency is questionable and may potentially lead to unjustified conclusions of the conducted tests to humans. Moreover, numerous the experimental therapies of nanomedicine were found lack of therapeutic efficacy. This is due to the poor prediction from mouse models of cancer that does not apply to human trials. (**Figure 1.1b**) To sum up, the preclinical models which can be systematically identified to generate standardized and reliable predictions for novel drug efficacy and safety in humans in preclinical process has been critically needed for application of nanomedicine.[20]

What features should an ideal preclinical model have? A list of potential advantages or disadvantages should be considered: Is the model convenient to work with? Does it model the complexities of the genetic background of the patient population and the mutational load and heterogeneity observed in human tumors? Does it model the tumor environment and functions? How stable the model is in long-term study? Can we extract quantitative data from the model and can these

data be generalized? Recent advances in microfabrication, microfluidics and stem cell technologies have enabled the development of preclinical models *ex-vivo* that could provide the basis for preclinical assays and standard with greater predictive power. These *ex-vivo* models such as three-dimensional (3D) cell cultures [21,22], ranged from functional units of human organs (Organ-on-a-chip)[14,23] to explant tissue culture[24–26]. New opportunities have emerged for the application of these models in preclinical drug discovery[27], such as target identification and validation, target-based screening, and phenotypic screening in a standardized, statistical, reproducible and personalized manner.

1.2 Current *ex-vivo* 3D culture models for drug discovery

For the discovery and evaluation of new drugs, nowadays *ex-vivo* models such as 3D cell cultures provide various advantages over conventional 2D cell cultures. These models can represent complex physiology *in vivo* to evaluate drug responses, and at the same time they are able to provide large amounts of relatively inexpensive but significant data as 2D models for prediction of therapeutic properties incorporated with computational modelling and systematical approaches.

3D cell culture systems have first drawn much attention and gained increased recognition as important drug evaluation tools a decade ago [28]. For instance, early-developed 3D culture systems have been applied to study phenomena[29–31], such as drug resistance and cell invasion [32]. *Ex vivo* cultures of

primary tissues are also to be included as 3D culture systems, however, the variety of tissue samples are difficult to standardized or to achieve the statistical significance for drug screening.[32,33] 3D cell cultures embedded in matrix and scaffolds are increasingly utilized because the potential of high throughput testing enable the large quantitative data to investigate differentiation and invasion processes of tumor cells triggered by factors from extracellular matrix.[34,35] Much progress of drug testing in 3D models has been made in natural and artificial matrices based on scaffolds (**Table 1.1**) [36,14]. These promising methods improve reproducibility, ease of use and reliability of 3D model systems tremendously.

Table 1.1 Three-dimensional cell culture matrices based on scaffolds [14]

Matrix or scaffold	Cells	Application
Collagen	Lung cancer cells	Epithelial–mesenchymal transition
	Breast cancer cells	Invasion
	Breast cancer cells, bone-differentiated mesenchymal stem cells	Invasion, metastasis
	Vascular endothelial cells, endothelial pericytes	Tubulogenesis
	Cardiomyocytes	Cardiac contraction
Matrigel	Hepatocytes, colon tumour cells	Drug metabolism, anticancer activity
	Hepatocytes, embryonic fibroblasts	Aggregate formation
Fibrin	Vascular endothelial cells, mesenchymal stem cells	Vasculogenesis
Alginate	Myeloblasts	Drug metabolism, anticancer activity
Poly(lactide-co-glycolide)	Oral squamous cell carcinoma	Tumour angiogenesis, anticancer activity
Foamed polylactic acid	Hepatocytes, brain cancer cells	Anticancer activity
Poly(ethylene) glycol	Hepatocytes	Drug metabolism

These *ex-vivo* tissue-like matrices have been largely used to establish 3D spheroid-based models to recapitulate the structural and functional complexity of human organs[37] (**Figure 1.2**) such as the liver, heart, lung, intestine, kidney, brain and bone [36].

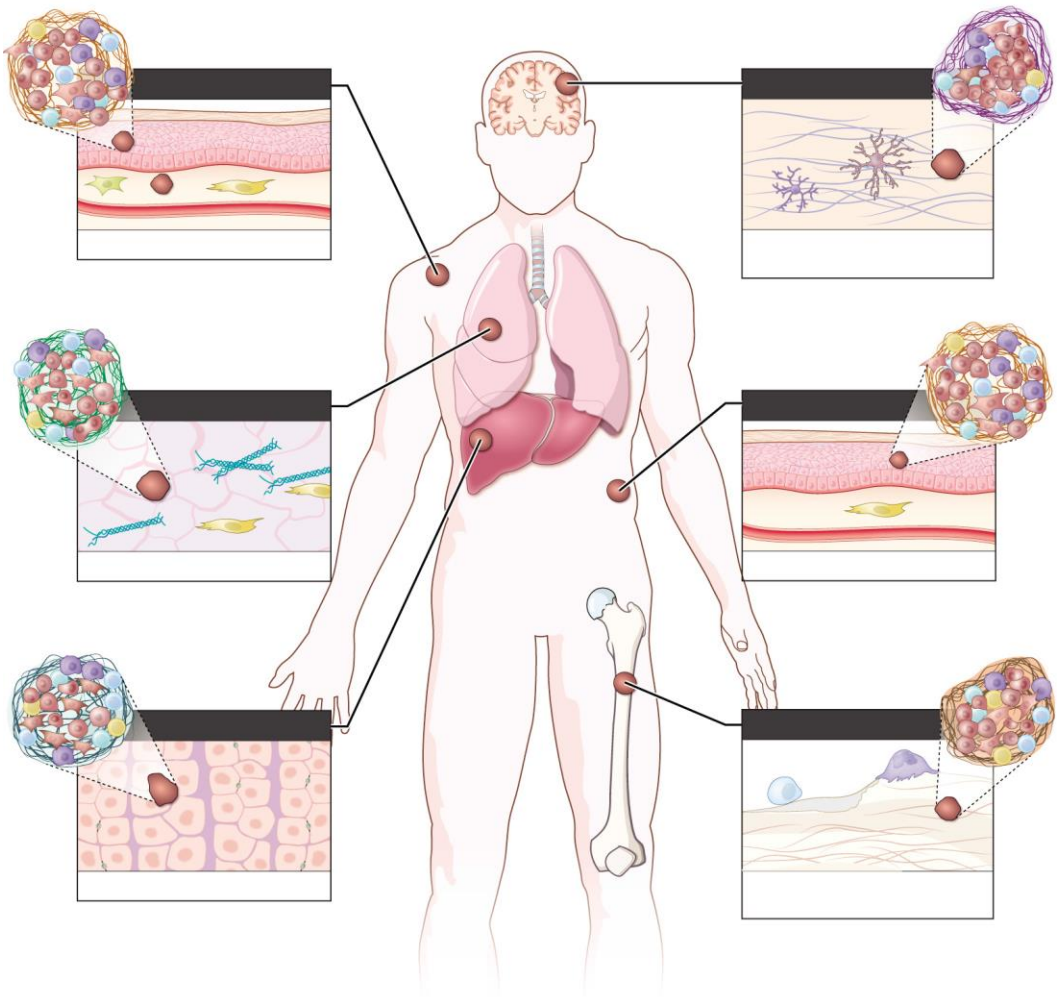

Figure 1.2 Designing spheroid-based *ex-vivo* platforms mimicking different *in-vivo* microenvironments. Here shows the architectural complexity at each of the diverse microenvironments in which both cell type and extracellular environment might affect treatment efficacy. [36, 37]

These can also reconstitute complex organ-level physiological functions, clinically relevant disease phenotypes and pharmacological responses that arise from structural and functional integration of multiple tissue or organ types. This characteristic allows more comprehensive and accurate preclinical predictions *ex vivo* for complex problems. To better mimic the physiological conditions *in vivo*,

fluid motions and cell culture substrates can also be controlled to reproduce various types of cues in the spheroid-based models[38,39] However, while designing 3D culture models with optional conditions, the increasing complexity have caused expensive and sometimes unnecessary procedures. Therefore, the specific 3D *ex-vivo* cell culture model based on needs are the future direction in preclinical models.

1.3 Challenges for NP transport in tumor for drug delivery

NPs, such as gold nanoparticles (AuNPs) and carbon nanotubes (CNTs), have been widely studied as promising vehicles for drug delivery and localization due to their unique properties enabling localization and targeted therapy of many diseases[40–42]. Large amount of work has focused on the targeting of NPs to specific cells and their blood circulation[43,44]. However, little is known about their transport within the tissues after being released from blood vessels, while limited delivery of drugs in dense tissues has been identified as one of the primary reasons for inefficient cancer therapy (**Figure 1.3**) [45,46]. Understanding the fundamental of NP transport in tissue will facilitate the development and discovery of nanomedicine for solid tumors as well as other diseases. It will also provide the medical and pharmaceutical community the reference while applying the drugs to clinical trials.

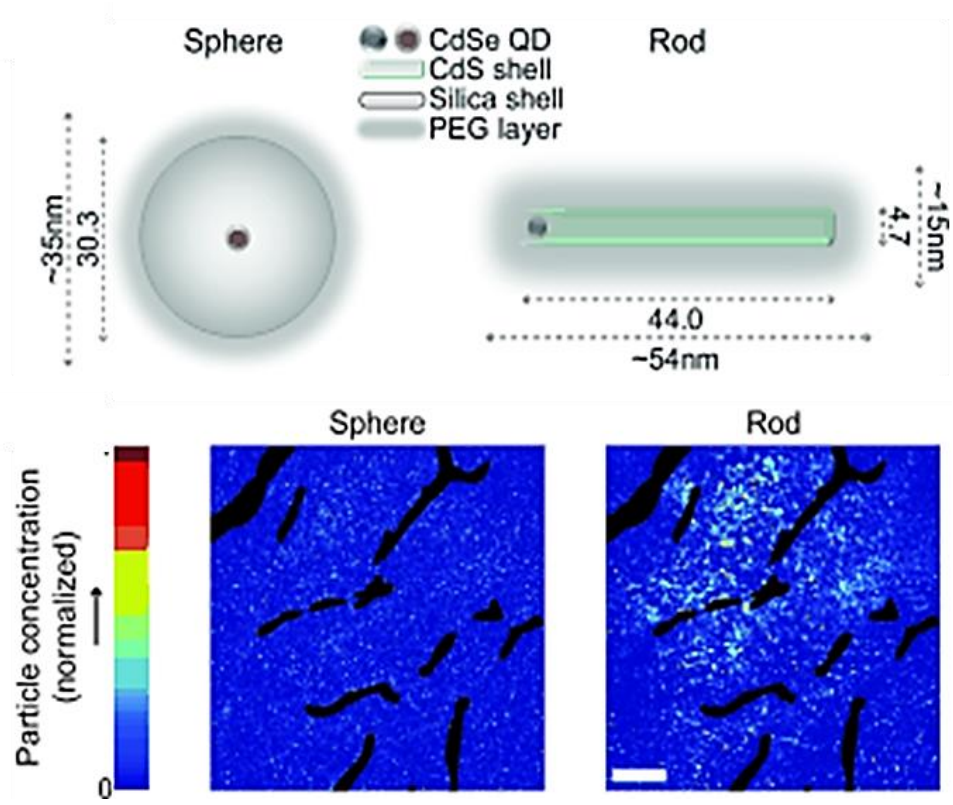

Figure 1.3 Distribution of NPs in tumors in vivo. Blood vessels are shown in black.[46]

Unfortunately, investigation of NP diffusion inside tissues is inherently difficult at the moment largely due to the lack of suitable models. 2D culture models as standard tools for therapeutic effect or toxicity studies[47,48] could not replicate the complex morphology and *in vivo* conditions. Meanwhile, *in-vivo* imaging of animal study was limited by the insufficient resolution and was not able to identify NP distribution in real-time in organs and deep tissues[49–51], which are also variable, and costly. Therefore, *ex-vivo* studies based on 3D cell culture models

become an applicable candidate for NP transport study to minimize the necessity of animal studies.

In the second and third chapters, we aim to better understand of NP diffusion in solid tumors, which will aid in development and application of these drug carriers and imaging agents for efficient penetration into cancerous tissues. To adequately evaluate transport and distribution of NPs inside the tumor tissue in 3D cell culture, the models shall meet the following needs: (1) 3D cell culture with spheroids-based features experimentally demonstrated similar morphology and functions as some original tissues. (2) The size of the spheroids can be accurately controlled with high uniformity which eliminates sample-to-sample variability and enables standardized mathematical description of experimental data. (3) Culture substrates (scaffolds) shall be high transparent with low scattering in order to evaluate NP transport in real time with high resolution imaging equipment. (4) They can also be easily integrated with high-throughput technologies. In the dissertation, cell spheroids grown in inverted colloidal crystal (ICC) scaffold [26,52], which have the advantages over the other models and simple enough to avoid the tradeoff of convenience will be utilized to conduct this study.

1.4 Computer-aided drug development and discovery

Computer-aided drug discovery methods have played a major role in the drug development. It can help researchers to design experiments at the early stage of drug development or to better understand experimental data. Many novel

computational methods were developed in discovering promising drug candidates.[53] Much progress has been made in areas such as scoring functions, similarity search methods and statistical approaches[54,55]. These computational tools such as Molecular Dynamics (MD) simulation and Pharmacokinetic/Pharmacodynamic (PK/PD) modeling are generally used for prediction and scoring of activity of new drugs binding in either target of interest[56] or early stage of the structure design[57], as well as prediction and optimization of drug metabolism and pharmacokinetics by high-throughput screening[58].

MD simulations, combining Newtonian physics and all-atom, flexible representation of proteins, water and other molecules to understand the dynamic interactions between them, can provide important qualitative information, such as the binding affinities of drugs to cell membrane (**Figure 1.4a**) [59,60]. Recent improvements in hardware and algorithms have accelerated the development of this method.[61] However, drug design is more than just molecular binding, biologic activity and selectivity for the target of interest. Meanwhile, once applied to whole animal or human, therapeutic drug metabolism and pharmacokinetics properties need to be considered as well. PK/PD modeling has been developed to simulate and obtain the quantitative information such as drug distribution and metabolism in humans. [58,62] Recent PK/PD simulations account for variations in perfusion, vascularization, interstitial transport, and non-linear local binding. Based on a comparison of the fundamental rates determining uptake, drugs can be classified depending on whether uptake is limited by blood flow, extravasation, interstitial

diffusion, or local binding and metabolism(**Figure 1.4b**)[63]. These parameters provides the systemic prediction of drug doses and efficiency within human.

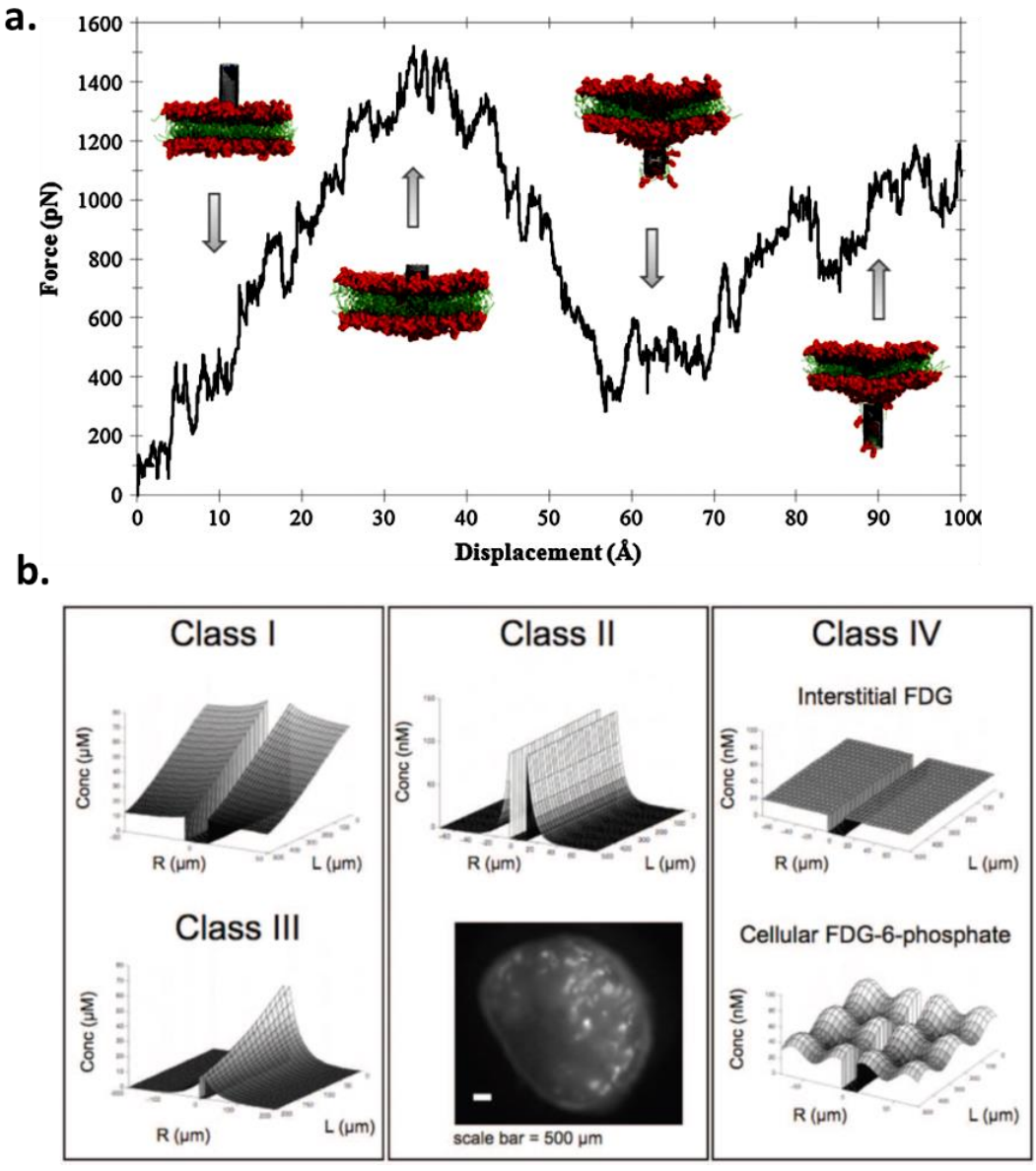

Figure 1.4 (a) the force–displacement profile of CNT during the cell membrane penetration by MD simulation. Displacement (A°) refers to the distance between the instantaneous and the initial positions of the CNT. **(b)** PK/PD Simulation results for different class (I to IV) agents. [59,60,63]

These computational tools have been incorporated into the drug discovery pipeline before a drug discovery is initiated. However, the corresponding experimental and preclinical/clinical validation are still needed to establish the tools with statistical significance and reproducibility in human. In another aspect, as *ex-vivo* experimental culture models develop, computer-aided data analysis and simulation can assist the design of experiment and generalization of the parameters for broader application. Therefore, a methodology of realistic model-based simulation combined with an *ex vivo* experimental framework shall be created. This integrated platform *ex vivo* allows better understanding of biophysical behavior before and during drug design, drug screening in a high-throughput miniaturized format and associated pharmacokinetic simulations to predict *in vivo* drug concentration profiles in a cost effective way for preclinical development of drug delivery systems.

1.5 3D cell culture for preclinical personalized drug screening

Stem cells are able to provide potentially unlimited resources of tissue culture for a wide range of toxicity models that could complement the variety of animal models from human which is more relevant and personalized. Embryonic stem cells (ESCs) have already been proven valuable for drug toxicity tests and other mechanistic studies [64,65]. Induced pluripotent stem cell (iPSC), which are generated by reprogramming human-derived cells back to the status of ESC-like

cells, allow the drug discovery and assessment to be designed under the conditions of personalized genetic background or medical case history. Pathway perturbations that underlie toxicity and disease, enabling the development of predictive assays for toxicity can be elucidated by comprehensive profiling of ESC/iPSCs via genomics, proteomics, transcriptomics, and metabolomics. This human tissue assay is essential to minimize the animal study which is discrepant from human. Therefore, incorporation of human stem cell based assays into drug discovery and toxicity testing offers the potential for safer and more personalized medicines, as well as reduced costs and decreased use of animal models[66].

Significant progress in technology focused on *ex-vivo* 3D cell/tissue cultures has been made, the next step is to consider the integration of stem cell technology to create interconnected patient-specific engineered tissues/organs[67]. The use of ESCs or iPSC in 3D cultures can further assemble them into specific tissues/organs to replicate *in vivo* morphology and environment[68]. Such patient-specific models require a sophisticated set of tools for 3D cell cultures with engineered environment to create controllable and precise interconnected tissue/organ structures. Among the advanced methods in the past decades regarding the complex 3D cultures and state-of-the-art scaffolding, a particularly exciting new development is the ability to explant the living tissue of a patient into 3D culture to obtain individualized predictive or prognostic information. So that, it is also possible to culture stem-based human tissues using excess material from surgery in 3D cell cultures[69,70]. The most recent development is that iPSC research

can be applied to these types of tissue and scaffold systems (**Figure 1.5a**) for a patient-specific drug development model[68,71]. For instance, a recent study developed cerebral organoids from iPSCs in 3D culture and replicated the anatomical organization of multiple human brain regions, including cerebral cortex [71,72] (**Figure 1.5b**). Moreover, the spheroids derived from iPS cells from a microcephaly patient showed complex system disorders in patient case history which can be modelled using *ex-vivo* 3D culture.

In spite of all the advantages and promise, tremendous work are needed to be done for design, optimization and application of these tools. In chapter four and five, we discuss the spheroids derived from ESCs grown in 3D scaffolding and pursue the optimized conditions for liver organoid model regarding to the scaffold design and bone-mimic substrate modification, which is essential for personalized drug screening and discovery.

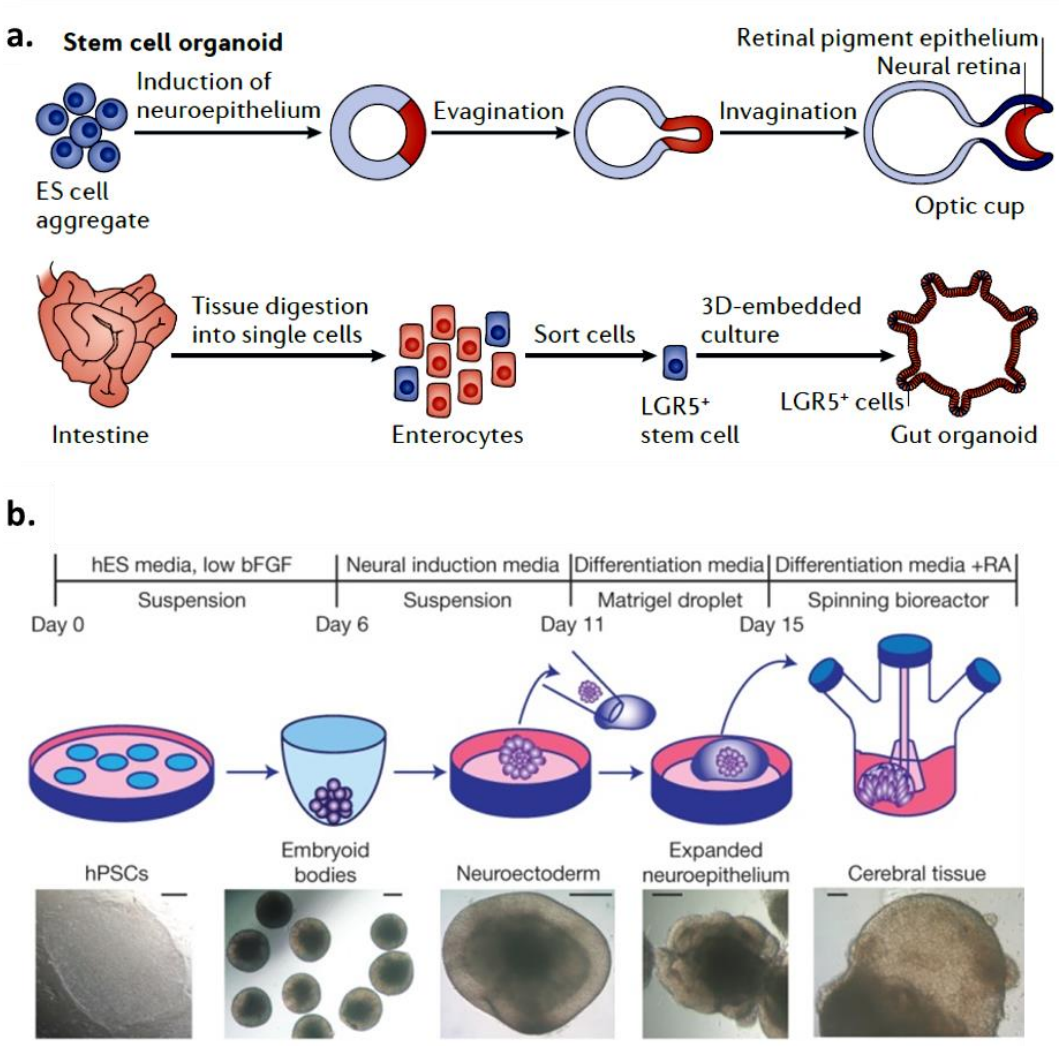

Figure 1.5 (a) Stem cell spheroid-based 3D cultures. Stem cells can be used to generate organoids that model the architecture and cellular composition of a larger organ. Both hESCs and hiPSCs have been used to generate organoids of the kidney, lung, intestine, liver, optic cup and brain in the presence of 3D scaffolds and differentiation factors. [68] **(b)** is an example of a brain tissue culture system. [72]

1.6 Dissertation Framework

A major goal of biomedical science in drug development and discovery is to translate our understanding of the fundamental principles that govern biological systems to improve therapeutic effects on patients. 3D cell culture *ex vivo* can function as an integration point for modelling human tissue or disease in experimental systems for fundamental studies and thereby yielding precise answers to the questions against new drugs. Achieving the full potential of these methods will involve the expertise of biological knowledge, material science and computational simulation.

Drug delivery and transport of nanomedicine through complex 3D tissues such as solid tumors can be adequately evaluated in specially prepared 3D cell culture as platform. This is an important consideration for pharmacodynamics analysis to validate drug doses and administration regimens required to achieve desired therapeutic effects. In coupling with computational Monte-Carlo sampling and analysis of conditioned microenvironment, the standardized and uniform-sized liver tumor spheroids culture model in ICC scaffolds *in vitro* could be used to identify or validate predictive drug transport and efficacy, while the transparency of the platform allowed convenient real-time monitoring of drug-cellular interaction. As a potential solution to improve the predictive power of *ex vivo* screening procedures, in chapter 2 and 3 of this dissertation established the experimental and conceptual framework for quantitative evaluation of drug delivery and transport in the tumor tissue *ex vivo* as a part of drug discovery, and

explored a new opportunity of carbon nanotubes as a promising nano-sized carrier for drug delivery.

In chapter 4 and 5, these models have been studied to generate replacement human tissues using patient-derived cells and/or stem cell. This is essential for future personalized drug screening and personalized medicine, as well as co-clinical trial applications with a patient's own cells adapted with stem cell techniques. It is able to develop patient-specific model for individualized study of drug safety and efficacy or drug–drug interactions. In this part of dissertation, ICC scaffolds with uniformly, controllable porous structure combined with a layer-by-layer (LBL) surface modification technique served as a platform for engineered embryonic stem cells towards optimal hepatic differentiation and hepatocyte formation for discovery of personalized drug testing. Bone marrow stromal cells as supporting layer for stem cell culture was found interacting and influenced by surface properties of 3D matrices.

Overall this dissertation introduces a promising and standardized 3D cell culture platform established in ICC scaffolds coupling with computational simulation which substantiate the capability in a range of areas in preclinical drug discovery. This platform is a window to fundamental understanding of nanomedicine, as well as a practical and valuable tool for drug discovery regarding drug delivery and transport through complex 3D tissues, as well as development of personalized drug screening.

1.7 References

(1) Sanna, V.; Sechi, M. Nanoparticle Therapeutics for Prostate Cancer Treatment. *Maturitas* **2012**, *73*, 27–32.

(2) Jain, S.; Hirst, D. G.; O'Sullivan, J. M. Gold Nanoparticles as Novel Agents for Cancer Therapy. *Br. J. Radiol.* **2012**, *85*, 101–113.

(3) Xu, X.; Ho, W.; Zhang, X.; Bertrand, N.; Farokhzad, O. Cancer Nanomedicine: From Targeted Delivery to Combination Therapy. *Trends Mol. Med.* **2015**, *21*, 223–232.

(4) Bertrand, N.; Wu, J.; Xu, X.; Kamaly, N.; Farokhzad, O. C. Cancer Nanotechnology: The Impact of Passive and Active Targeting in the Era of Modern Cancer Biology. *Adv. Drug Deliv. Rev.* **2014**, *66*, 2–25.

(5) *Nanoengineering: Global Approaches to Health and Safety Issues*; Elsevier Science, 2015.

(6) Yang, K.; Feng, L.; Liu, Z. The Advancing Uses of Nano-Graphene in Drug Delivery. *Expert Opinion on Drug Delivery*, 2015.

(7) Savla, R.; Garbuzenko, O. B.; Chen, S.; Rodriguez-Rodriguez, L.; Minko, T. Tumor-Targeted Responsive Nanoparticle-Based Systems for Magnetic Resonance Imaging and Therapy. *Pharm. Res.* **2014**, *31*, 3487–3502.

(8) Kanapathipillai, M.; Brock, A.; Ingber, D. E. Nanoparticle Targeting of Anti-Cancer Drugs That Alter Intracellular Signaling or Influence the Tumor Microenvironment. *Adv. Drug Deliv. Rev.* **2014**, *79-80*, 107–118.

(9) Chow, E. K.-H.; Ho, D. Cancer Nanomedicine: From Drug Delivery to Imaging. *Sci. Transl. Med.* **2013**, *5*, 216rv4.

(10) Sekhon, B. S.; Kamboj, S. R. Inorganic Nanomedicine--Part 1. *Nanomedicine* **2010**, *6*, 516–522.

(11) Sekhon, B. S.; Kamboj, S. R. Inorganic Nanomedicine--Part 2. *Nanomedicine* **2010**, *6*, 612–618.

(12) Pritchard, J. F.; Jurima-Romet, M.; Reimer, M. L. J.; Mortimer, E.; Rolfe, B.; Cayen, M. N. Making Better Drugs: Decision Gates in Non-Clinical Drug Development. *Nat. Rev. Drug Discov.* **2003**, *2*, 542–553.

(13) Scannell, J. W.; Blanckley, A.; Boldon, H.; Warrington, B. Diagnosing the Decline in Pharmaceutical R&D Efficiency. *Nat. Rev. Drug Discov.* **2012**, *11*, 191–200.

(14) Esch, E. W.; Bahinski, A.; Huh, D. Organs-on-Chips at the Frontiers of

Drug Discovery. *Nat. Rev. Drug Discov.* **2015**, *14*, 248–260.

(15) Etheridge, M. L.; Campbell, S. A.; Erdman, A. G.; Haynes, C. L.; Wolf, S. M.; McCullough, J. The Big Picture on Nanomedicine: The State of Investigational and Approved Nanomedicine Products. *Nanomedicine* **2013**, *9*, 1–14.

(16) Holmes, A.; Bonner, F.; Jones, D. Assessing Drug Safety in Human Tissues — What Are the Barriers? *Nat. Rev. Drug Discov.* **2015**, *14*, 1–3.

(17) Blanco, E.; Shen, H.; Ferrari, M. Principles of Nanoparticle Design for Overcoming Biological Barriers to Drug Delivery. *Nat. Biotechnol.* **2015**, *33*, 941–951.

(18) Gnach, A.; Lipinski, T.; Bednarkiewicz, A.; Rybka, J.; Capobianco, J. a. Upconverting Nanoparticles: Assessing the Toxicity. *Chem. Soc. Rev. Chem. Soc. Rev* **2015**, *44*, 1561–1584.

(19) National Cancer Institute. Establish and Standardize an Analytical Cascade for Nanomaterial Characterization http://ncl.cancer.gov/objectives_ncl_obj1.asp.

(20) Bowes, J.; Brown, A. J.; Hamon, J.; Jarolimek, W.; Sridhar, A.; Waldron, G.; Whitebread, S. Reducing Safety-Related Drug Attrition: The Use of in Vitro Pharmacological Profiling. *Nat. Rev. Drug Discov.* **2012**, *11*, 909–922.

(21) Astashkina, A.; Grainger, D. W. Critical Analysis of 3-D Organoid in Vitro Cell Culture Models for High-Throughput Drug Candidate Toxicity Assessments. *Adv. Drug Deliv. Rev.* **2014**, *69-70*, 1–18.

(22) Thoma, C. R.; Zimmermann, M.; Agarkova, I.; Kelm, J. M.; Krek, W. 3D Cell Culture Systems Modeling Tumor Growth Determinants in Cancer Target Discovery. *Adv. Drug Deliv. Rev.* **2014**, *69-70*, 29–41.

(23) Bhise, N. S.; Ribas, J.; Manoharan, V.; Zhang, Y. S.; Polini, A.; Massa, S.; Dokmeci, M. R.; Khademhosseini, A. Organ-on-a-Chip Platforms for Studying Drug Delivery Systems. *J. Control. Release* **2014**, *190*, 82–93.

(24) Jiguet Jiglaire, C.; Baeza-Kallee, N.; Denicolaï, E.; Barets, D.; Metellus, P.; Padovani, L.; Chinot, O.; Figarella-Branger, D.; Fernandez, C. Ex Vivo Cultures of Glioblastoma in Three-Dimensional Hydrogel Maintain the Original Tumor Growth Behavior and Are Suitable for Preclinical Drug and Radiation Sensitivity Screening. *Exp. Cell Res.* **2014**, *321*, 99–108.

(25) Dereli-Korkut, Z.; Akaydin, H. D.; Ahmed, a. H. R.; Jiang, X.; Wang, S. Three Dimensional Microfluidic Cell Arrays for Ex Vivo Drug Screening with Mimicked Vascular Flow. *Anal. Chem.* **2014**, *86*, 2997–3004.

(26) Lee, J.; Cuddihy, M. J.; Cater, G. M.; Kotov, N. a. Engineering Liver

Tissue Spheroids with Inverted Colloidal Crystal Scaffolds. *Biomaterials* **2009**, *30*, 4687–4694.

(27) Eglen, R. M.; Randle, D. H. Drug Discovery Goes Three-Dimensional: Goodbye to Flat High-Throughput Screening? *Assay Drug Dev. Technol.* **2015**, *13*, 150629132900006.

(28) Abbott, A. Biology ' S New Dimension. *Nature* **2003**, *424*, 870–872.

(29) Doillon, C. J.; Gagnon, E.; Paradis, R.; Koutsilieris, M. Three-Dimensional Culture System as a Model for Studying Cancer Cell Invasion Capacity and Anticancer Drug Sensitivity. *Anticancer Res.* **2004**, *24*, 2169–2177.

(30) Loessner, D.; Stok, K. S.; Lutolf, M. P.; Hutmacher, D. W.; Clements, J. A.; Rizzi, S. C. Bioengineered 3D Platform to Explore Cell-ECM Interactions and Drug Resistance of Epithelial Ovarian Cancer Cells. *Biomaterials* **2010**, *31*, 8494–8506.

(31) Friedl, P.; Wolf, K. Tumour-Cell Invasion and Migration: Diversity and Escape Mechanisms. *Nat. Rev. Cancer* **2003**, *3*, 362–374.

(32) Fischbach, C.; Chen, R.; Matsumoto, T.; Schmelzle, T.; Brugge, J. S.; Polverini, P. J.; Mooney, D. J. Engineering Tumors with 3D Scaffolds. *Nat. Methods* **2007**, *4*, 855–860.

(33) Gerlach, J. C.; Lin, Y.-C.; Brayfield, C. A.; Minteer, D. M.; Li, H.; Rubin, J. P.; Marra, K. G. Adipogenesis of Human Adipose-Derived Stem Cells within Three-Dimensional Hollow Fiber-Based Bioreactors. *Tissue Eng. Part C. Methods* **2012**, *18*, 54–61.

(34) Pampaloni, F.; Reynaud, E. G.; Stelzer, E. H. K. The Third Dimension Bridges the Gap between Cell Culture and Live Tissue. *Nat. Rev. Mol. Cell Biol.* **2007**, *8*, 839–845.

(35) Kunz-Schughart, L. A.; Freyer, J. P.; Hofstaedter, F.; Ebner, R. The Use of 3-D Cultures for High-Throughput Screening: The Multicellular Spheroid Model. *J. Biomol. Screen.* **2004**, *9*, 273–285.

(36) Friedrich, J.; Seidel, C.; Ebner, R.; Kunz-Schughart, L. A. Spheroid-Based Drug Screen: Considerations and Practical Approach. *Nat. Protoc.* **2009**, *4*, 309–324.

(37) Tanner, K.; Gottesman, M. M. Beyond 3D Culture Models of Cancer. *Sci. Transl. Med.* **2015**, *7*, 283ps9.

(38) Bhatia, S. N.; Ingber, D. E. Microfluidic Organs-on-Chips. *Nat. Biotechnol.* **2014**, *32*, 760–772.

(39) Sackmann, E. K.; Fulton, A. L.; Beebe, D. J. The Present and Future Role of Microfluidics in Biomedical Research. *Nature* **2014**, *507*, 181–189.

(40) Jain, S.; Hirst, D. G.; O'Sullivan, J. M. Gold Nanoparticles as Novel Agents for Cancer Therapy. *Br. J. Radiol.* **2012**, *85*, 101–113.

(41) Sanna, V.; Pala, N.; Sechi, M. Targeted Therapy Using Nanotechnology: Focus on Cancer. *Int. J. Nanomedicine* **2014**, *9*, 467–483.

(42) Sanna, V.; Sechi, M. Nanoparticle Therapeutics for Prostate Cancer Treatment. *Maturitas* **2012**, *73*, 27–32.

(43) Christensen, J.; Litherland, K.; Faller, T.; van de Kerkhof, E.; Natt, F.; Hunziker, J.; Boos, J.; Beuvink, I.; Bowman, K.; Baryza, J.; *et al.* Biodistribution and Metabolism Studies of Lipid Nanoparticle-Formulated Internally [3H]-Labeled siRNA in Mice. *Drug Metab. Dispos.* **2014**, *42*, 431–440.

(44) *Nanotoxicology: Progress toward Nanomedicine, Second Edition*; CRC Press, 2014.

(45) Dawidczyk, C. M.; Russell, L. M.; Searson, P. C. Nanomedicines for Cancer Therapy: State-of-the-Art and Limitations to Pre-Clinical Studies That Hinder Future Developments. *Front. Chem.* **2014**, *2*, 1–13.

(46) Chauhan, V. P.; Popović, Z.; Chen, O.; Cui, J.; Fukumura, D.; Bawendi, M. G.; Jain, R. K. Fluorescent Nanorods and Nanospheres for Real-Time in Vivo Probing of Nanoparticle Shape-Dependent Tumor Penetration. *Angew. Chem. Int. Ed. Engl.* **2011**, *50*, 11417–11420.

(47) Sharifi, S.; Behzadi, S.; Laurent, S.; Forrest, M. L.; Stroeve, P.; Mahmoudi, M. Toxicity of Nanomaterials. *Chem. Soc. Rev.* **2012**, *41*, 2323–2343.

(48) Qiao, Y.; An, J.; Ma, L. Single Cell Array Based Assay for in Vitro Genotoxicity Study of Nanomaterials. *Anal. Chem.* **2013**, *85*, 4107–4112.

(49) Qian, X.; Peng, X.-H.; Ansari, D. O.; Yin-Goen, Q.; Chen, G. Z.; Shin, D. M.; Yang, L.; Young, A. N.; Wang, M. D.; Nie, S. In Vivo Tumor Targeting and Spectroscopic Detection with Surface-Enhanced Raman Nanoparticle Tags. *Nat. Biotechnol.* **2008**, *26*, 83–90.

(50) Park, J.-H.; Gu, L.; von Maltzahn, G.; Ruoslahti, E.; Bhatia, S. N.; Sailor, M. J. Biodegradable Luminescent Porous Silicon Nanoparticles for in Vivo Applications. *Nat. Mater.* **2009**, *8*, 331–336.

(51) Kumar, R.; Roy, I.; Ohulchanskky, T. Y.; Vathy, L. A.; Bergey, E. J.; Sajjad, M.; Prasad, P. N. In Vivo Biodistribution and Clearance Studies Using Multimodal Organically Modified Silica Nanoparticles. *ACS Nano* **2010**, *4*, 699–708.

(52) Kotov, N. A.; Liu, Y.; Wang, S.; Cumming, C.; Eghtedari, M.; Vargas, G.; Motamedi, M.; Nichols, J.; Cortiella, J. Scaffolds. **2004**, *20*.

(53) Sliwoski, G.; Kothiwale, S.; Meiler, J.; Lowe, E. Computational Methods in Drug Discovery. *Pharmacol. Rev.* **2014**, *66*, 334–395.

(54) Vogt, M.; Bajorath, J. Chemoinformatics: A View of the Field and Current Trends in Method Development. *Bioorg. Med. Chem.* **2012**, *20*, 5317–5323.

(55) Duffy, B. C.; Zhu, L.; Decornez, H.; Kitchen, D. B. Early Phase Drug Discovery: Cheminformatics and Computational Techniques in Identifying Lead Series. *Bioorg. Med. Chem.* **2012**, *20*, 5324–5342.

(56) Durrant, J. D.; Hall, L.; Swift, R. V; Landon, M.; Schnaufer, A.; Amaro, R. E. Novel Naphthalene-Based Inhibitors of Trypanosoma Brucei RNA Editing Ligase 1. *PLoS Negl. Trop. Dis.* **2010**, *4*, e803.

(57) Biarnés, X.; Bongarzone, S.; Vargiu, A. V.; Carloni, P.; Ruggerone, P. Molecular Motions in Drug Design: The Coming Age of the Metadynamics Method. *J. Comput. Aided. Mol. Des.* **2011**, *25*, 395–402.

(58) Rajman, I. PK/PD Modelling and Simulations: Utility in Drug Development. *Drug Discov. Today* **2008**, *13*, 341–346.

(59) Mousavi, S. Z.; Amjad-Iranagh, S.; Nademi, Y.; Modarress, H. Carbon Nanotube-Encapsulated Drug Penetration Through the Cell Membrane: An Investigation Based on Steered Molecular Dynamics Simulation. *J. Membr. Biol.* **2013**, *246*, 697–704.

(60) Buch, I.; Giorgino, T.; De Fabritiis, G. Complete Reconstruction of an Enzyme-Inhibitor Binding Process by Molecular Dynamics Simulations. *Proc. Natl. Acad. Sci. U. S. A.* **2011**, *108*, 10184–10189.

(61) Stanley, N.; De Fabritiis, G. High Throughput Molecular Dynamics for Drug Discovery. *Silico Pharmacol.* **2015**, *3*, 3–6.

(62) Stroh, M.; Addy, C.; Wu, Y.; Stoch, S. A.; Pourkavoos, N.; Groff, M.; Xu, Y.; Wagner, J.; Gottesdiener, K.; Shadle, C.; *et al.* Model-Based Decision Making in Early Clinical Development: Minimizing the Impact of a Blood Pressure Adverse Event. *AAPS J.* **2009**, *11*, 99–108.

(63) Thurber, G. M.; Weissleder, R. A Systems Approach for Tumor Pharmacokinetics. *PLoS One* **2011**, *6*.

(64) *Handbook of Nanotoxicology, Nanomedicine and Stem Cell Use in Toxicology*; Sahu, S. C.; Casciano, D. A., Eds.; John Wiley & Sons, Ltd: Chichester, UK, 2014.

(65) Schwartz, M. P.; Hou, Z.; Propson, N. E.; Zhang, J.; Engstrom, C. J.; Costa, V. S.; Jiang, P.; Nguyen, B. K.; Bolin, J. M.; Daly, W.; *et al.* Human Pluripotent Stem Cell-Derived Neural Constructs for Predicting Neural Toxicity. *Proc. Natl. Acad. Sci. U. S. A.* **2015**.

(66) Ramamoorthy, H.; Abraham, P.; Isaac, B. Mitochondrial Dysfunction and Electron Transport Chain Complex Defect in a Rat Model of Tenofovir Disoproxil Fumarate Nephrotoxicity. *Jjournal Biochem. Mol. Toxicol.* **2014**, *28*, 246–255.

(67) Williamson, A.; Singh, S.; Fernekorn, U.; Schober, A.; Williamson, A. Lab on a Chip The Future of the Patient-Specific Body-on-a-Chip. **2013**, 3471–3480.

(68) Shamir, E. R.; Ewald, A. J. Three-Dimensional Organotypic Culture : Experimental Models of Mammalian Biology and Disease. *Nat. Publ. Gr.* **2014**, *15*, 647–664.

(69) Cheung, K. J.; Gabrielson, E.; Werb, Z.; Ewald, A. J. Collective Invasion in Breast Cancer Requires a Conserved Basal Epithelial Program. *Cell* **2013**, *155*, 1639–1651.

(70) Sato, T.; Stange, D. E.; Ferrante, M.; Vries, R. G. J.; Van Es, J. H.; Van den Brink, S.; Van Houdt, W. J.; Pronk, A.; Van Gorp, J.; Siersema, P. D.; *et al.* Long-Term Expansion of Epithelial Organoids from Human Colon, Adenoma, Adenocarcinoma, and Barrett's Epithelium. *Gastroenterology* **2011**, *141*, 1762–1772.

(71) Beebe-Dimmer, J.; Yee, C. HHS Public Access. *Cancer* **2015**, *121*, 1265–1272.

(72) Lancaster, M. A.; Renner, M.; Martin, C.-A.; Wenzel, D.; Bicknell, L. S.; Hurles, M. E.; Homfray, T.; Penninger, J. M.; Jackson, A. P.; Knoblich, J. A. Cerebral Organoids Model Human Brain Development and Microcephaly. *Nature* **2013**, *501*, 373–379.

Chapter II

Transport of Nanoparticles

in 3D Cellular Spheroid Culture

2.1 Abstract

As nanotechnology has been developing emergently for drug development, understanding transport of nanoparticles (NP) in dense tissues is essential for biomedical imaging and drug delivery using these agents. Compared to animal studies and traditional Petri dish cell cultures, three-dimensional (3D) tissue replicas approach the complexity of the actual organs and enable high temporal and spatial resolution of the NP permeation. We investigated diffusional transport of NPs generally investigated as nanomedicines such as carbon nanotubes (CNTs) and

gold nanoparticles (AuNPs) in highly uniform spheroids of hepatocellular carcinoma derived by 3D cell culture in Inverted Colloidal Crystal (ICC) scaffolds. It was found that apparent diffusion coefficients of CNTs in these tissue replicas are extremely high and comparable to diffusion rates of similarly charged small molecules whereas AuNPs only accumulates on the surface of the tissue replicas in spite of the aspect-ratio difference. Moreover, diffusivity of CNTs in tissues is enhanced after functionalization with targeting ligand, transforming growth factor (TGFβ1). The finding in this chapter shows the feasibility of 3D cell culture testing for nanomedicine and the result also indicate nanotubes and potentially similar nanostructures are capable of fast and deep diffusion within the dense tissue for anticancer treatment such as solid tumor.

2.2 Introduction

Nanoparticles (NPs), such as polymeric nanocapsules, metallic nanorods (NRs) and carbon nanotubes (CNTs) have emerged as potent nanomedicine for drug delivery and cancer imaging[1–3]. Their unique optical and chemical properties originating from quantum confinement promisingly enhanced the therapy and diagnostics of many diseases[4–8]. There are many advantages of NPs as nanomedicine compared to the traditional methods of therapeutics and diagnostics, which include the prospects of functionalization with multiple targeting ligands,

synergistic effect of multiple drugs delivered in the same cargo, long clearance times, and enhanced permeability and retention effect for cancer treatment. Therefore, it prompted tremendous efforts on the targeting efficiency of NPs to specific cells, circulation in blood, and distribution among organs [9,10–12].

However, little is known about their transport within the organs following transvascular delivery or locally injection that affects both the safety and efficacy of NPs as imaging and therapeutic agents. Understanding the transport processes for NPs within tissues or organ has been often hindered by lack of adequate preclinical models. Most studies have relied on analysis of cells grown in two-dimensional (2D) cell culture models[13–15], but they do not have adequate 3D morphology to maintain their differentiated functions, as a result, fail to replicate diffusion conditions in tissues. A variety of data regarding the biodistribution of NPs in different animal models has been reported [15–17]. Although the studies involving the dissection of animal organs followed by imaging improve the resolution of distribution maps, they are limited to static post-treatment results. In addition, it is difficult to extract the transport parameters from these studies, because they were mostly focused on toxicity and drug clearance. They are also expensive and laborious comparing to *ex-vivo* studies. Moreover, the animal data were obtained for different tumor models, therapeutic modalities, administration routes, doses, and quantification methods, in consequences, it is difficult to be generalized because of the varieties of animals and environmental conditions, as

well as the difference between animals and human. This results in mismatches of the therapeutic effect on human in clinical study. [18,19]

Meanwhile, lack of suitable imaging technology with sufficient temporal and spatial resolution in animal studies lead to the difficulty of real-time NP distribution maps within organs. The resolutions of real-time *in vivo* imaging methods such as magnetic[20], X-ray[21,22], and photoacoustic imaging[23] are currently sub-millimeter, micrometers or even sub-micrometers, respectively. Currently spatial resolution of fluorescent imaging have mainly met the requirement for the diameter of NPs (sub-μm).[24] However, this resolution trades off the imaging time and depth of tissue penetration *in vivo*. Hence, the difficulties regarding to integration of advanced optical microscopy techniques incorporated with animal studies have been aware of. The high cost of such studies also makes it difficult to justify the routes for various types of NPs with different size, shape, surface charge, targeting ligand, and loaded drug.

Therefore, critical need of standardized and convenient testing platform is emerging. *Ex-vivo* 3D tissue cultures became an attractive tool for evaluation of the transport of NP as delivery or imaging agent in tissues or organs. They are not only able to provide the morphological environment in actual tissues comparing to 2D cell cultures, but also allow high resolution and high throughput study for NP transport within tissue or organ and they allow for real-time monitoring of the transport processes. The most widely used 3D tissue models are the multicellular

spheroids[25–27] and multilayer cell cultures[28,29]. Recently, they have been used for the evaluation of NPs, such as polystyrene beads[30], liposomes[31], and viral particles[32]. These studies showed that smaller particles can infiltrate spheroids more effectively than larger particles,[30] while NPs with low charge were shown to penetrate to the central regions of the spheroids better than those with high charge[31,33]. Also, it was indicated that NP transport was improved by functionalization with extracellular matrix-destroying enzymes[30]. It was also demonstrated that spheroid cell cultures of hepatocytes for the toxicity evaluation of CdTe and AuNPs have better correlation with the animal data found in the literature than 2D cell culture models.[34]

Following important qualitative observations made in the studies above, it is important to quantitatively describe the properties of NP transport based on the phenomenon. In previous reports, some classic laws of diffusion describing the permeation of particles in homogeneous media may be utilized to describe the observations whereas could not predict NP transport accurately in tissues.[35,36,37] This is due to the cooperative nature of their interactions with cell membranes, multiplicity of active transport processes, and entanglement of diffusion in different dimensions. The suitable and easily approached model incorporated with correspondent diffusion's laws is required for the insight understanding of NP transport. Such that, the central objective of this chapter is to establish the experimental and conceptual framework for quantitative evaluation of NP transport in the dense tissues by the 3D cellular spheroid culture model *ex vivo*. In order to

accomplish the objectives we utilized 3D cell cultures of liver carcinoma cells (HepG2, ATCC) in inverted colloidal crystals (ICC)[28,38] that were proven to provide close replicas for many organs with respect to both morphology and biological functions[34,38]. They are uniquely suitable for the purpose of this work because the spheroids grown in ICCs provide can be highly controlled and uniform in diameter, greatly simplifying the mathematical description of transport processes. Moreover, ICC scaffolds are transparent and make real-time assessment of NP distribution possible. AuNPs and CNTs as promising candidate of nanomedicine have been studied in the following sections.

2.3 Materials and Methods

2.3.1 Fabrication of ICC Scaffolds

We utilized ICC scaffolds to obtain the tumor-like HepG2 spheroids as described in previous work[10]; polyacrylamide hydrogel ICC scaffolds were prepared by utilizing colloidal crystals (CC) (**Figure 2.1a**) as templates. To control the pore sizes of scaffolds, we use uniform glass beads in diameter of 170μm for penetration study. 3D structure of CC with high connection can be achieved by annealing at 680°C for 3 hours, following by being transferred into ICC geometry high porosity. ICC scaffolds with uniform porous structure (**Figure 2.1b**) facilitate formation of nearly perfect mono-dispersed spheroids with tissue-like features[10].

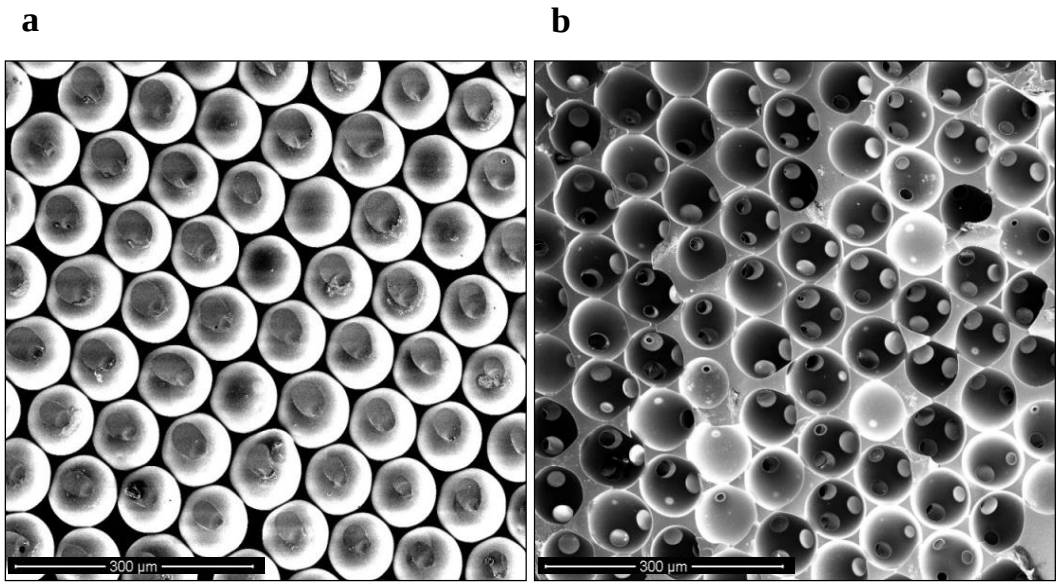

Figure 2.1 SEM images of dehydrated hydrogel ICC scaffolds **(b)** created by dissolving beads template **(a)** from hydrogel matrix. Pore diameter was shrunk during the dehydration process of SEM preparation. Scale bars: 300µm **(a, b).**

2.3.2 Cell and Spheroid Culture

Human hepatocellular carcinoma cells (HepG2, ATCC) were maintained with Eagle's Minimum Essential Medium (EMEM) supplemented with 10% fetal bovine serum (FBS) and 1% Penicillin–Streptomycin. All the medium was filtered using 0.22µm SteriCup filter assembly (Millipore, USA) and stored at 4 °C for no longer than 2 weeks.

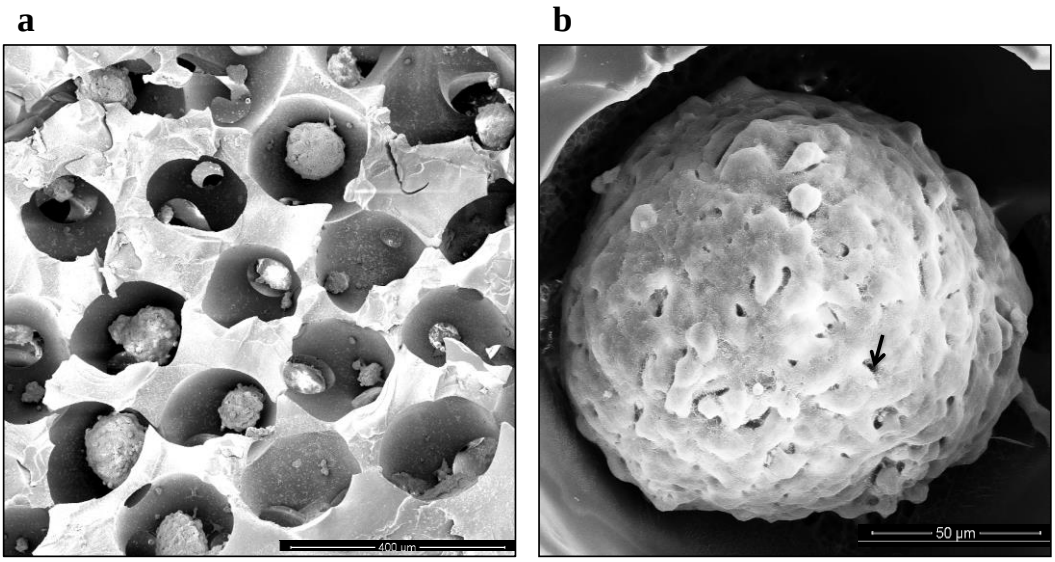

Figure 2.2 SEM images of **(a)** dehydrated hydrogel ICC scaffolds cultured with cellular spheroids. **(b)** SEM images of a mature spheroid in an ICC scaffold cultured for 5 days. Maturation of the spheroid is accompanied with formation of a layer of extracellular matrix on its surface and individual cells become difficult to distinguish. Scale bars: 400µm **(a)** and 50µm **(b).**

To form tissue-like cellular spheroids in ICC scaffold, 500,000 cells in a 25µl of dense cell suspension ($2x10^7$ cells/ml) was dropped on top of dehydrated hydrogel ICC scaffold, followed by adding 975µl of media gently. Total culture volume was maintained at 1000µl in 96-well plates, with media change every two days. Nearly perfectly mono-dispersed spheroids in average diameter of 150 µm were observed in high yield after 5 days culture. (**Figure 2.2a**) Magnified image (**Figure 2.2b**) indicated structural features including the development of an extracellular matrix coating the membrane surface as well as abnormal bile canaliculated structures, which recreate solid tumors tissue *in vivo*.

2.3.3 Biocompatibility of CNTs

CNTs are considered to be fairly biocompatible generally[39,40]. Because toxicity data for 2D *vs.* 3D assays can be substantially different,[40] we decided to initially carry out two standard live/dead cell viability assays which consisted of calcein AM and ethidium homodimer (EthD-1) (**Figure 2.3a-d**) addressing plasma membrane integrity and esterase activity. Both assays indicated that the HepG2 cells of spheroids proliferate normally in contact with medium containing as much as 1 mg/mL CNTs. As the concentration was increased to 2 mg/mL, the cell viability decrease. The CNTs in spheroid 3D culture shows better biocompatibility than similar toxicity thresholds reported in 2D cultures.[40] Therefore, we chose the concentration of CNTs at 0.5 mg/mL for the following permeation studies. Additional test WST-1 assay (**Figure 2.3e**) at this concentration was used to re-verify cellular proliferation, viability, and cytotoxicity, based on the reduction of tetrazolium salt to formazan by electron transport across the plasma membrane of dividing cells. It indicated that the viability of CNT-treated cells is identical within the experimental error to HepG2 spheroids in CNT-free media (control).

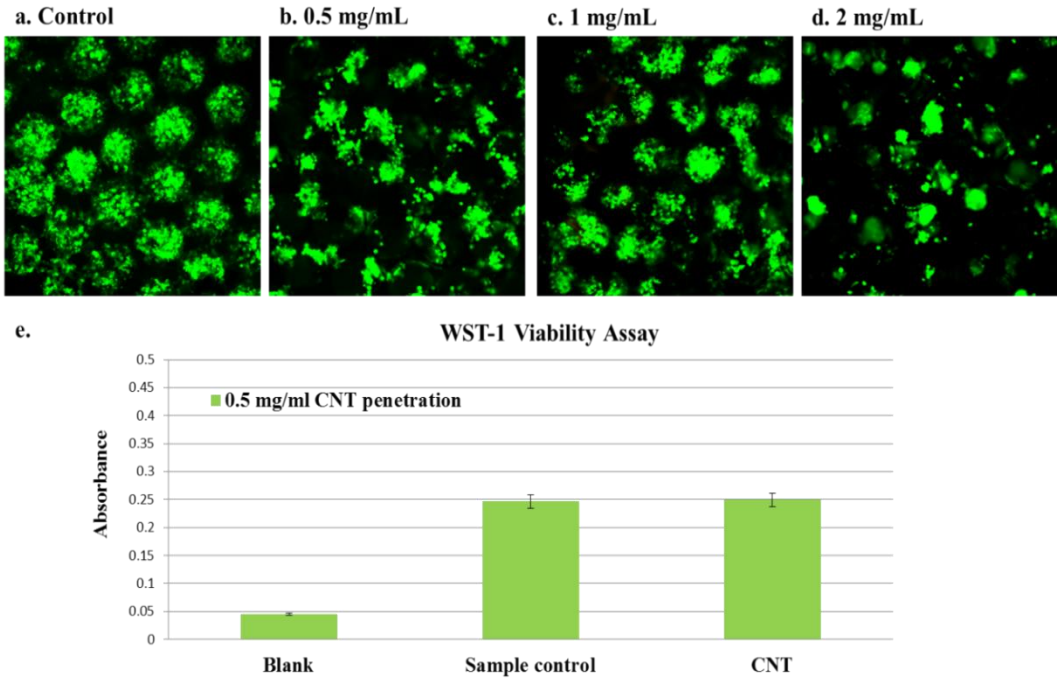

Figure 2.3 Confocal images of live/dead cell viability assay (LIVE/DEAD Viability/Cytotoxicity Kit, Invitrogen, US) of HepG2 cells in spheroids cultured for 3 days in medium containing (**a**, control) 0, **(b)**, 0.5, (**c**) 1, and (**d**) 2 mg/mL CNTs in the culture medium (Eagle's Minimum Essential Medium (EMEM) supplemented with 10% Fetal Bovine Serum (FBS) and 1% Penicillin–Streptomycin (ATCC)). (**e**) WST-1 assay for HepG2 spheroids cultured with 0.5 mg/mL of CNTs as-prepared for 2 hours. (*P < 0.01)

2.3.4 Labeling of CNTs with Fluorescence and Targeting Ligands

To observe CNTs inside the 3D tumor tissue model under the confocal microscopes, we labeled CNTs (P3, Carbon Solution, Inc.) with fluorescence (Fluorescein isothiocyanate isomer I) by cross-linker, 1-ehyl-3-(3-dimethylaminopropyl) carbodiimide (EDC), to make CNTs have an emission of wavelength at 595 nm. The oxidized CNTs were reacted with hexamethylene diamine in the presence of EDC to afford a linker between the CNT and the subsequent fluorescent probe. In brief, 2 mg of oxidized CNTs were mixed with 5 mg hexamethylenediamine and 1 mg EDC in 4ml 0.1M MES buffer (pH 6.0). The mixed solution was stirred at room temperature for 2 h. The oxidized CNTs bonded with hexamethylenediamine (CNT–CONH–$(CH_2)_6NH_2$) were obtained by centrifuging the mixture at 10,000 rpm for 20 min. 4mg of obtained CNTs were dissolved in 200µl dimethylformamide (DMF). N, N-diisopropylethylamine (DIEA, 2µL, 11.5µmol) and a solution of fluorescein isothiocyanate (FITC, 2.5mg, 6.4µmol) in 200µL of DMF were added. The reaction mixture was stirred for 4h at room temperature. The solvent was evaporated and the FITC-labeled CNTs were precipitated several times from methanol/diethyl ether and dried under vacuum.[41,42]

2.3.5 Functionalized CNTs with Targeting Ligands

CNTs were functionalized by covalent attachment of the targeting ligand. The CNTs with targeting ligands, transforming growth factor β1 (TGFβ1, Santa

Cruz Biotechnology, Inc.), were prepared using the following procedure which was simplified from the previous method. In short, 0.5mg oxidized CNTs (0.5 mg/mL) were dispersed in phosphate buffered saline (PBS) by sonication for 5 min followed by incubation with 8 mg EDC for 1 min at room temperature, after which samples were immediately vortexed. Next, TGFβ1 5μg in 50μl PBS and FITC (Fluorescein isothiocyanate isomer I) (2μg in 20μl of DMF) were added together, and the resulting mixture was allowed to react for an additional 2 h at 37 °C in a rotator rocker. These samples were then centrifuged at 1300 rpm for 20 min for 3 times to remove unbound antibodies and excessed FITC in Centricon YM-50 tubes (Millipore Corporation, MA, USA) and the resulting CNT-TGFβ1-FITC were suspended in 1 mL serum-free Eagle's Minimum Essential Medium (EMEM) and used immediately.[42]

2.3.6 Labeling of AuNPs with Fluorescent Polyethylene Glycol

To functionalize the surface of AuNPs with fluorescence, 2mg/ml AuNP solution with three aspect-ratios in water is added with 2mg/ml fluorescent polyethylene glycol (SH-PEG-FITC, MW 5K, Nanocs Inc.), then the mixture is kept at room temperature overnight. The mixture is centrifuged at 5000-8000 rpm/min depending on the size of AuNPs for 15min to remove the unattached molecules.

2.3.7 Molecular Weight of CNTs and Their Derivatives

According to TEM images (**Figure 2.4a**), the CNTs had an average diameter of 1.2 nm and a length of 1,000 nm. Therefore, it was calculated that 40 carbon atoms ((1.55 nm/0.245 nm) × (3.1414) × (2 carbon atoms)) are around the circumference. For every 0.283 nm length, there are 124 carbon atoms (4 × 40 carbons), namely, 6,790,106 amu ((1000nm/0.283nm) × (160) × (12.01)). So the calculated molecular weight of CNT is 6.79×10^6 Da. Fluorescent CNTs bearing, on average, 1-3 atomic % of FITC, which is 1246 Da (0.02 x 160 x 389.38 per tube) heavier than original CNTs as purchased (**Figure 2.4b**). To determine how many antibodies are there on targeted CNT (CNT-TGFβ1-FITC), TEM images were captured and analyzed statistically and it was found 2~3 antibodies on each CNT in average, which agreed with theoretical number 2.97 ± 0.32 (3.80×10^{-20} g, (TGFβ1 MW 23000 Da × 1.66×10^{-24} g)). As a result, the theoretical molecular weight of CNT-TGFβ1-FITC is 6.87×10^6 Da. The actual molecular weight was verified by TEM images and determined to be 6.84×10^6 Da due to loss during reaction (**Figure 2.4c**).

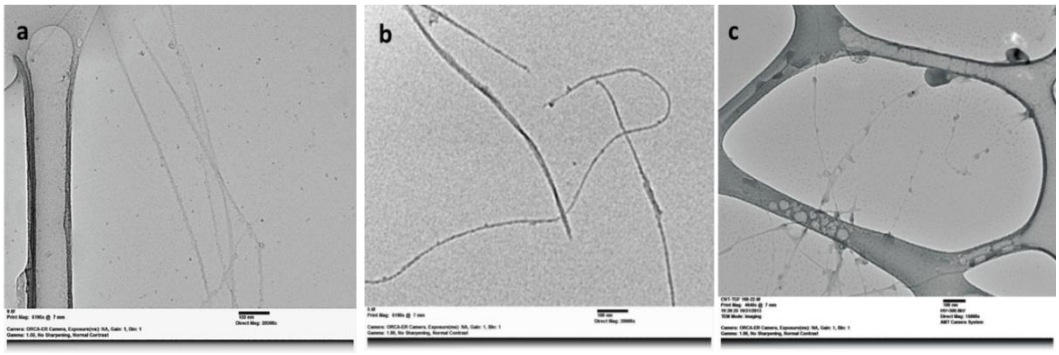

Figure 2.4 TEM images of CNT **(a)**, CNT-FITC **(b)**, and CNT-TGFβ1-FITC **(c)**.

2.3.8 Theoretical Diffusion Coefficients of CNTs, FITC, TGFβ1 and Rhodamine B

Theoretical diffusion coefficient $\boldsymbol{D_0}$ for spherical particle related to the temperature $\boldsymbol{T}$ and the friction coefficient $\boldsymbol{f_0}$ can be calculated using the Stokes equation:

$$\boldsymbol{D_0 = \frac{k_b T}{f_0}} \qquad \textbf{Eq 2.1}$$

$$\boldsymbol{f_0 = 6\pi\eta L_0} \qquad \textbf{Eq 2.2}$$

where $\boldsymbol{k_b} = 1.38 \times 10^{-20}\ m^2 \cdot g/(s^2 \cdot K)$, $\boldsymbol{T}$ = 293 K, $\boldsymbol{\eta}$ = viscosity of the solute, $\boldsymbol{L_0}$ = radius of a spherical particle or molecule with a volume equal to the volume of a rod-like particle or molecule. Frictional coefficient is determined by the viscosity of the media and diameter of the spherical particle.

The frictional coefficient f_n of a non-spherical particle (rod or tube) is usually larger than that of a spherical one of the same volume because there is a larger surface area in contact with the solvent. Therefore, assuming D_n is the theoretical diffusion coefficient for non-spherical particles, when the particle is non-spherical such as a CNT, we could suppose a CNT as a rod-like particle which has a length a = 1000 nm/2 and radius b = 1.55nm/2 (Carbon Solution, Inc. Data sheet.). Its volume is given by the formula:

$$V_{rod} = 2\pi ab^2 \qquad \textbf{Eq 2.3}$$

The aspect ratio P can be defined as: $P = a/b$ = 645.2. The frictional coefficient of a rod-like particle can be calculated as **(6)**

$$f_n = f_0 \frac{\left(\frac{2}{3}\right)^{1/3} P^{2/3}}{ln(2P) - 0.3} \qquad \textbf{Eq 2.4}$$

Relative diameter L_n of rod-like particle is determined to be 7.67 nm by equation **(7)**[43]

$$L_n = \sqrt[3]{\frac{3ab^2}{2}} \qquad \textbf{Eq 2.5}$$

f_0 is calculated to be 7.52 × 10^{-4} g/s in tumor tissue (η = 5.2 ± 2.5 Pa·s**).**[47]

$f_0 = 6\pi\eta R_0 = 6 \times \pi \times 5.2 \times 10^3$ g/(s·m) × 7.67 m × 10^{-9} = 7.52 × 10^{-4} g/s

$D_0 = (1.38 \times 10^{-16}\ gcm^2/s^2 \times 293\ K)/7.52 \times 10^{-4} = 5.4 \times 10^{-15}\ m^2/s$

Thus f_n equals 9.91×10^{-5} g/s for tumor tissue according to equation (4). Theoretical D_n value of rod-shaped CNTs in tumor tissue is determined to be $5.7 \times 10^{-16}\ m^2/s$.

To calculate the theoretical diffusion coefficients of TGFβ1, FITC, and Rhodamine B (RhB), it was assumed that these molecules were rod-shaped, where the longest distance in the molecular structure is represented by ***a*** and the shortest by ***b.*** The molecular structure and distance of TGFβ1 between atoms were reported in a previous study[1] (**Figure 2.5 a**). Moreover, ***a*** and ***b*** of FITC and Rhodamine were analyzed and measured using software **Spartan 10** (**Figures 2.5 b, c**). ***P*** will be calculated based on values of ***a*** and ***b*** for each type of molecule.

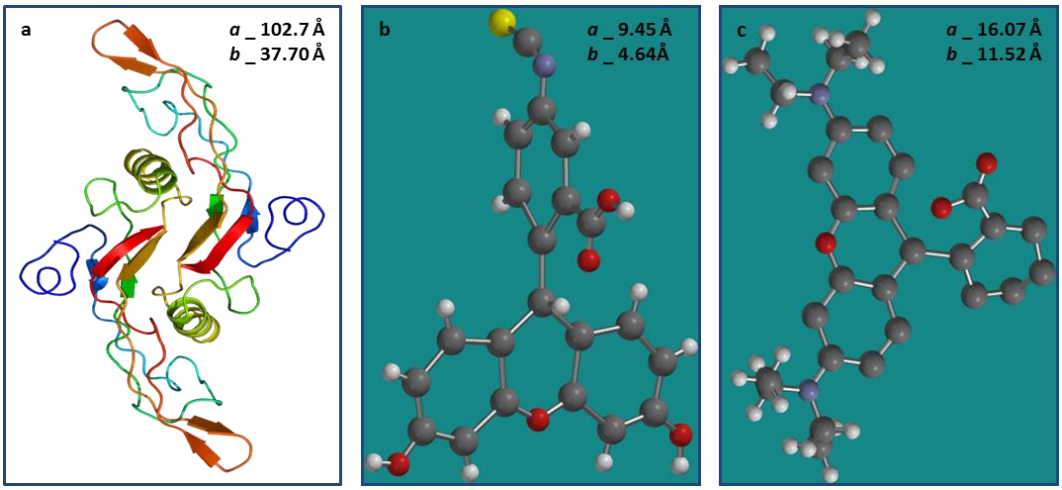

Figure 2.5 The molecular structure and distance of TGFβ1[1] (**a**), FITC (**b**) and RhB (**c**) where ***a*** is the longest distance between atoms in one structure, and ***b*** is the radius of stimulated molecular structure. Spheres (atoms) of (**b**) and (**c**): Grey-C; White-H; Red-O; Purple-N; Yellow-S.

1. TGFβ1

$$\boldsymbol{L_0} = \sqrt[3]{\frac{\boldsymbol{3ab^2}}{\boldsymbol{2}}} = \sqrt[3]{\frac{\boldsymbol{3 \times 1.607 \times 1.152^2}}{\boldsymbol{2}}} = 6.027\ nm$$

$\boldsymbol{f_0 = 6\pi\eta L_0} = \boldsymbol{6 \times \pi} \times 5.2 \times 10^3$ g/(s·m) × 6.027×10^{-9} m = 5.9×10^{-4} g/s

$\boldsymbol{D_0} = \frac{\boldsymbol{k_b\, T}}{\boldsymbol{f_0}}$ = 1.38×10^{-16} g·cm^2/s^2 × 293 K /5.9×10^{-4}g/s = 6.9×10^{-15} m^2/s

$\boldsymbol{f_n = f_0}\ \frac{(\frac{2}{3})^{\boldsymbol{1/3}}\boldsymbol{P^{2/3}}}{\boldsymbol{ln(2P) - 0.3}}$ = 5.9×10^{-4} g/s × $\frac{(\frac{2}{3})^{\boldsymbol{1/3}}2.724^{\boldsymbol{2/3}}}{\boldsymbol{ln(2}\times 2.724\boldsymbol{) - 0.3}}$ = 7.1×10^{-4} g/s

$\boldsymbol{D_n} = \frac{\boldsymbol{k_b\, T}}{\boldsymbol{f_n}}$ = 1.38×10^{-16} g·cm^2/s^2 × 293 K /7.1×10^{-4} g/s = 5.7×10^{-15} m^2/s

2. FITC

$$\boldsymbol{L_0} = \sqrt[3]{\frac{\boldsymbol{3ab^2}}{\boldsymbol{2}}} = \sqrt[3]{\frac{3 \times 0.945 \times 0.4634^2}{2}} = 0.673\ \text{nm}$$

$\boldsymbol{f_0 = 6\pi\eta L_0} = 6 \times \boldsymbol{\pi} \times 5.2 \times 10^3$ g/(s·m) × 0.673×10^{-9} m = 6.6×10^{-5} g/s

$\boldsymbol{D_0} = \frac{\boldsymbol{k_b\, T}}{\boldsymbol{f_0}}$ =1.38×10^{-16} g·cm^2/s^2 K^{-1} × 293 K /6.6×10^{-5} g/s = 6.1×10^{-14} m^2/s

$\boldsymbol{f_n = f_0}\ \frac{(\frac{2}{3})^{\boldsymbol{1/3}}\boldsymbol{P^{2/3}}}{\boldsymbol{ln(2P) - 0.3}}$ = 6.6×10^{-5} g/s × $\frac{(\frac{2}{3})^{\boldsymbol{1/3}}\boldsymbol{1.395^{2/3}}}{\boldsymbol{ln(2}\times \boldsymbol{1.395)-0.3}}$ = 9.91×10^{-5} g/s

$\boldsymbol{D_n} = \frac{\boldsymbol{k_b\, T}}{\boldsymbol{f_n}}$ = 1.38×10^{-20} g·m^2/s^2 K^{-1} × 293K /9.91×10^{-5} g/s = 4.1×10^{-14} m^2/s

3. RhB

$$\boldsymbol{L_0} = \sqrt[3]{\frac{\boldsymbol{3ab^2}}{\boldsymbol{2}}} = \sqrt[3]{\frac{3 \times 1.607 \times 1.152^2}{2}} = 1.473\ nm$$

$\boldsymbol{f_0} = \boldsymbol{6\pi\eta L_0} = 6 \times \boldsymbol{\pi} \times 5.2 \times 10^3$ g/(s·m) × 1.473 m 10^{-9} = 1.45×10^{-4} g/s

$\boldsymbol{D_0} = \frac{\boldsymbol{k_b T}}{\boldsymbol{f_0}}$ =1.38×10^{-16} g·cm^2/s^2 K^{-1} × 293K /1.45×10^{-4} g/s = 2.8×10^{-14} m^2/s

$\boldsymbol{f_n} = \boldsymbol{f_0}\ \frac{(\frac{2}{3})^{1/3}\boldsymbol{P^{2/3}}}{\boldsymbol{ln(2P)-0.3}} = 1.45 \times 10^{-4}$ g/s × $\frac{(\frac{2}{3})^{1/3}\boldsymbol{1.395^{2/3}}}{\boldsymbol{ln(2\times 1.395)-0.3}}$ = 2.2×10^{-4} g/s

$\boldsymbol{D_n} = \frac{\boldsymbol{k_b T}}{\boldsymbol{f_n}}$ = 1.38×10^{-16}g·cm^2/s^2 K^{-1} × 293K /2.2×10^{-4} g/s = 1.8×10^{-14} m^2/s

$\boldsymbol{D_0}$ is the diffusion coefficient for a spherical shape ;

$\boldsymbol{D_n}$ is the diffusion coefficient for a rod shape.

2.3.9 Imaging Methods for NP Transport Study

Confocal Microscopy. Stained with live/dead assay, live cells are green, while dead cells show red. In live/dead assay test, contracted HepG2 spheroids in ICC scaffolds were treated with 0.5 mg/mL, 1mg/mL, and 2 mg/mL CNTs in culture medium for 2 hours, with non-treated spheroids (CNT free) used as the

control. To be observed by Confocal Microscopy during penetration, HepG2 cells in spheroids in scaffolds were pre-labeled by orange-colored CMTMR (Invitrogen, CA); CNTs labeled with FITC were added into scaffolds under the microscope. After 20 min, observation of the penetration process was initiated through a confocal microscope and 36 z-stack images range from top (0μm) to bottom (~150μm) were taken of the whole spheroid every 20 min. The process of FITC and RhB molecules penetration into spheroids was observed in the same way as the CNTs.

Surface Enhanced Raman Scattering (SERS) Spectroscopy. The inelastic scattered radiation was collected with a Renishaw Invia Reflex system equipped with two dimensional Peltier charge coupled device (CCD) detectors and a Leica confocal microscope. The spectrograph uses high resolution gratings with additional band-pass filter optics. The laser line focused onto the spheroid in scaffold with backscattering geometry using either 100× objective providing scattering areas of ~0.5 μm for mapping, or a macrosampling 90° objective adaptor for SERS in suspension. [44]

2.4 Results and Discussion

3D cell cultures in ICC scaffolds[10] are used in this study to investigate AuNP and CNT permeation through cellular spheroids formed by hepatocellular carcinoma cells. The transport process was monitored and recorded in real time by available imaging methods such as confocal microscope and SERS Spectroscopy.

2.4.1 AuNP Transport in HepG2 Cellular Spheroid

SERS, as a potential imaging method, was utilized first to observe AuNPs. However, it was found damaging the live cells during the focusing process within 10 min. The alternative imaging AuNPs were modified with fluorescent thiol-PEG-FITC for observation within cellular spheroids. HepG2 cells were labeled by CellTracker™ CMRA (Invitrogen, US) with orange-red luminescence. Gold nanospheres, nanoshells with multiple sizes and gold nanorods with different aspect ratios of 1:2 and 1:3 in diameter of 30nm were observed under the confocal microscope and SERS. Unfortunately, AuNPs in general were opt to accumulate on the surface of the spheroids. (**Figure 2.6**)

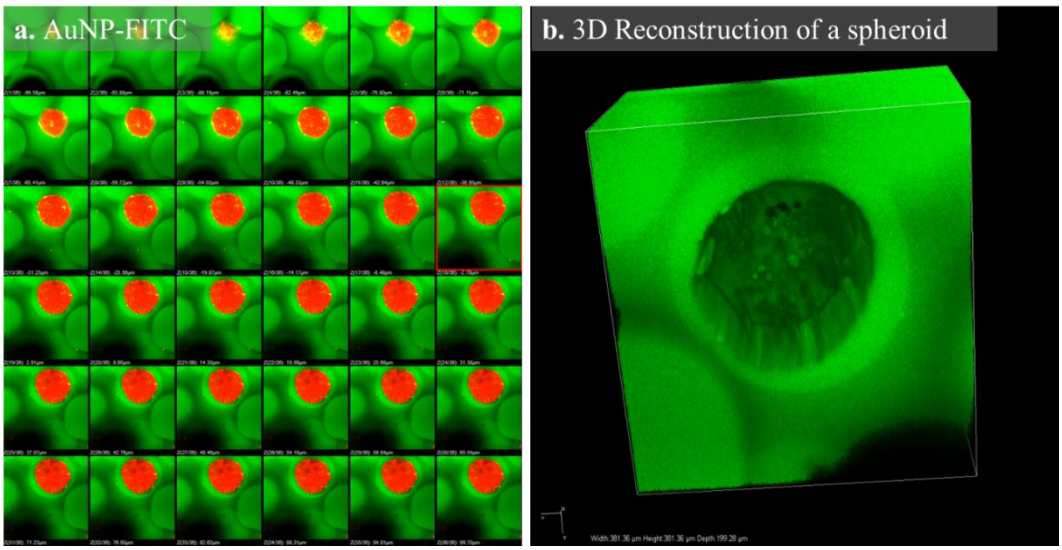

Figure 2.6 Sliced confocal images of HepG2 spheroids after 90 min exposure to **(a)** AuNR-FITC (Green) with dimension of 30:60nm. HepG2 cells in spheroids were stained red (CMTPX) before spheroid formation for images. **(b)** 3D re-construction image can clearly show the inefficient penetration of AuNPs on the surface of the cellular spheroid.

2.4.2 Diffusion of CNTs in Cellular Spheroid

To observe CNTs using standard confocal microscopes inside the spheroids, we labeled them with standard luminescent tag FITC. Transforming growth factor β1 (TGFβ1) was chosen as the targeting ligand because TGFβ receptors are present in HepG2 cells[14] and up-regulated in many cancers. The nanotubes without targeting ligand are referred to as CNT-FITC while the ones carrying both TGFβ1 and FITC are referred to as CNT-TGFβ1-FITC. The total load of the TGFβ1 per CNT was 1.13×10^{-17} g which amounts to 2.6±0.3 molecules of the targeting ligand on an average nanotube. The average molecular weight (*Mr*) of CNT-TGFβ1-FITC

was 6.84×10^6 Da. It can be compared to $Mr = 6.79 \times 10^6$ Da of the CNT-FITC that are $5.83\pm0.74 \times10^4$ Da lighter. Electrokinetic zeta-potential (ζ) of CNT-TGFβ1-FITC and CNT-FITC were -8.4±0.306 mV and -0.01±0.001 mV, respectively (**Table 2.1**).

Table 2.1 Zeta potential or Molecular Charge of CNTs and Small Molecules

	Zeta potential or Molecular Charge (in PBS pH=7.4)
CNT-FITC-TGFβ1	-8.4±0.31 mV
CNT-FITC	-0.01±0.001 mV
TGFβ1	-4.7±0.02 mV
RhB	Positive
FITC	Negative

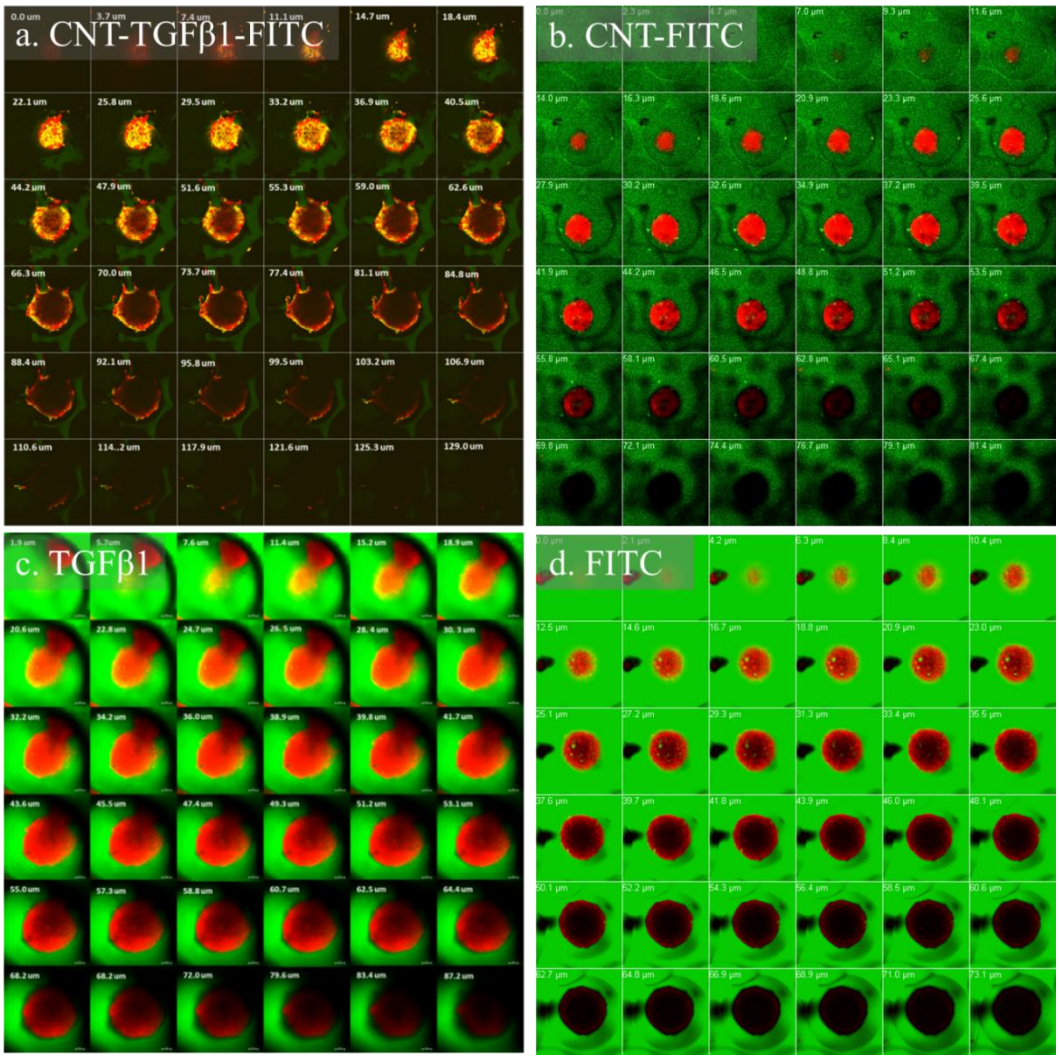

Figure 2.7 Confocal imaging and modeling of diffusion profiles in HepG2 spheroids after 20 min exposure to fluorescent penetrants. Sliced confocal images of HepG2 spheroids after 20 min exposure **(b)** CNT-FITC and **(d)** FITC (8.7 ×10-5mg/ml). HepG2 cells in spheroids were stained red (CMTPX) before spheroid formation for images. CNT-FITC and FITC have green fluorescence. CNTs and free molecules have green fluorescence in (**a** and **c**); the penetration depth is defined at the peak of fluorescent intensity. HepG2 cells in spheroids were stained red (CMTPX) before spheroid formation for images (**a** and **c**).

To visualize green-fluorescing CNT-FITC and CNT-TGFβ1-FITC on the background of tissue spheroids, HepG2 cells were labeled by CellTracker™ CMRA (Invitrogen, US) with orange-red luminescence. In some cases, HepG2 cells in spheroids were stained by CellTracker™ Red CMTPX dye or 5-chloromethylfluorescein diacetate (CMFDA) (Life Technologies, US) with red and green luminescence, respectively. *Z*-stack images of multiple spheroids (**Figure 2.7a, c**) were captured at 20, 40, 60, 80, 100, and 120 minutes after addition of permeants to the cell culture. FITC and TGFβ1 molecules were also observed as control (**Figure 2.7b, d**).

Apparent diffusion coefficients, $\boldsymbol{D_a}$, reflecting the experimentally observable rate of their transport were obtained for FITC, Rhodamine B (RhB), TGFβ1, CNT-FITC, and CNT-TGFβ1-FITC by fitting the progression of experimental diffusion profiles with the Second Fick's law (**Table 2.2**) using our own code. [41-45]

$$\frac{\partial C}{\partial t} = D_a \cdot \frac{1}{r^2}\frac{\partial}{\partial r} \cdot \left(r^2 \cdot \frac{\partial C}{\partial r}\right) \qquad \textbf{Eq 2.6}$$

where $\boldsymbol{C}$ = concentration, $\boldsymbol{t}$ = time, $\boldsymbol{r}$ = distance/radius, $\boldsymbol{D_a}$ = diffusion coefficient. We assumed that the diffusing substance moves into the center of the spheroid and the boundary at $r = 0$ is the surface of the spheroid:

(i) $C(0, t) = C_0, t \geq 0$ (L is the mean diameter of 3D tumor tissue model);

(ii) $C(R, t) = 0, t = 0;$

(iii) At $r = d, \partial^2 C/\partial t^2 = 0$ (d is the measure of penetration depth at a certain time point). Then we obtained the equation regarding the depth d and time t from

$$d^2 = 6\pi D_a \cdot t \qquad \textbf{Eq 2.7}$$

Table 2.2 Experimental Diffusion Coefficients of CNTs and Small Molecules

	Apparent Diffusion Coefficient, D_a (m^2/s in PBS pH=7.4)
CNT-FITC-TGFβ1	$(1.5\pm0.2)\times10^{-13}$
CNT-FITC	$(0.9\pm0.3)\times10^{-14}$
TGFβ1	$(2.5\pm0.3)\times10^{-13}$
RhB	$(5.9\pm0.3)\times10^{-13}$
FITC	$(1.6\pm0.3)\times10^{-14}$

In our model of diffusion, the tumor tissue-like spheroid is considered as a sphere of radius ***L***. Under the boundary conditions of the experiments performed, this depth of highest concentration in the diffusion front was the measure of penetration depth ***d.*** Firstly, according to the z-stack and cross-section images, depth ***d*** in equation **(7)** represents how far fluorescence reached inside the spheroid, where the fluorescence represents FITC, RhB, and CNTs or their derivatives. These data of depth ***d*** and time ***t*** abstracted from images will be substituted into equation **2.7** and certain values of $\boldsymbol{D_{ex}}$ will be fit to find the best value of ***D*** that minimizes the error by statistically analysis of *Mathematica 8.0* (**See Appendix**).

The values $\boldsymbol{D_a}$ for FITC and RhB indicate that diffusion of these small molecules in cellular spheroids grown in ICC scaffolds are similar to those observed previously in solid tissues ;[15] these data provided us useful benchmarks and validated our methods. Concentration profiles inside the spheroids were derived from the fluorescent intensity of the permeants (**Figure 2.8**). As anticipated from the previous studies,[3, 16] diffusivity of the small luminescent molecules in tissue model is strongly dependent on charge, with $\boldsymbol{D_a}$ = (5.9±0.3) $\times 10^{-13}$ m^2/s for RhB being considerably higher than $\boldsymbol{D_a}$ = (1.6±0.3) $\times 10^{-14}$ m^2/s for FITC. The positive charge of RhB is facilitated by electrostatic attraction to negatively charged cellular membranes. We noticed that $\boldsymbol{D_a}$ = (0.9±0.3) $\times 10^{-14}$ m^2/s of CNT-FITC is comparable to the diffusion coefficient of free FITC. Note that the average molecular mass *Mr* =6.79 × 10^6 Da of CNT-FITC is 1.7×10^4 larger than that of FITC with *Mr* = 389.4 Da. The startling closeness of diffusivity for these two

species contradicts known trends for diffusivity of permeants in gas, liquid, solid or gel. As such, diffusivity CNT-FITC predicted by Einstein-Stokes diffusion equation for rod-like particles is lower by almost two orders of magnitude that experimental values (**Table 2.3**).

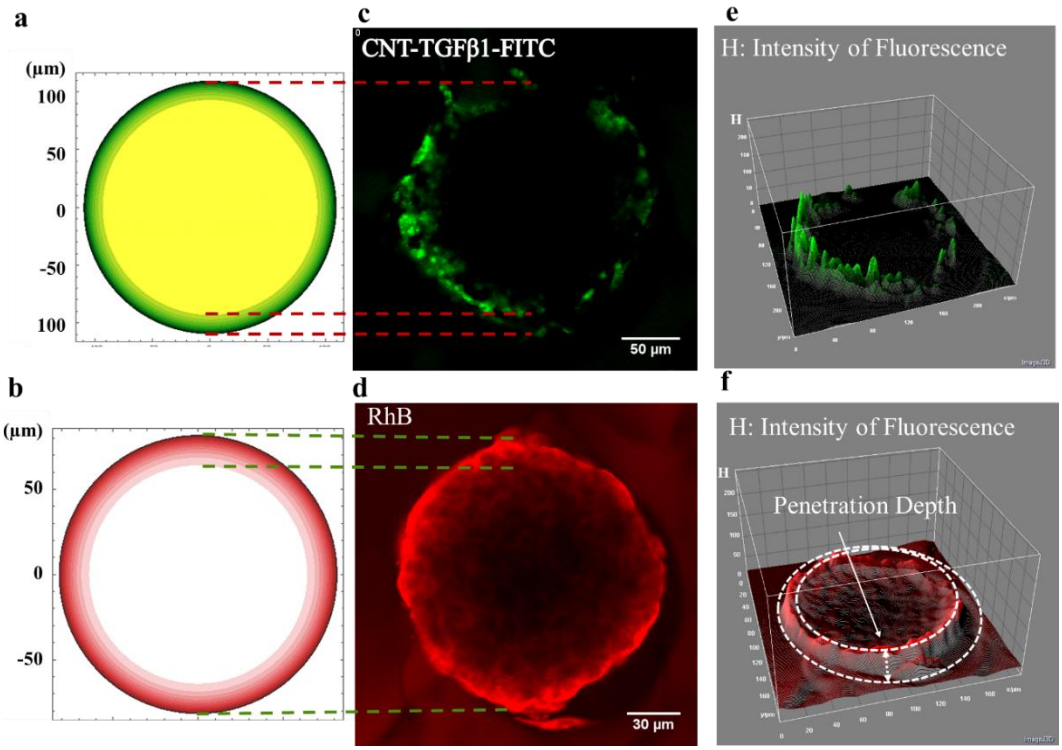

Figure 2.8 Confocal imaging and modeling of diffusion profiles in HepG2 spheroids after 20 min exposure to fluorescent penetrants. (**a**) and (**b**) are calculated diffusion profile of CNT-TGFβ1-FITC and RhB, which compare to (**c**) and (**d**), permeation profiles of CNT-TGFβ1-FITC and RhB at central focal plane of the spheroid with its 3D surface plot; (**e, f**) are the 3D surface plot of (**c, d**); H-axis represents the fluorescent intensity.

Table 2.3 Stokes-Einstein diffusion coefficients of CNTs and small molecules

	Stokes-Einstein Value of *D* rod-like shape (m^2/s in tissue)	**Stokes-Einstein Value of *D* spherical shape** (m^2/s in tissue)
CNT-FITC-TGFβ1	5.7×10^{-16}	5.4×10^{-15}
CNT-FITC	5.7×10^{-16}	5.4×10^{-15}
TGFβ1	5.7×10^{-15}	6.9×10^{-15}
Rhodamine	1.8×10^{-14}	2.8×10^{-14}
FITC	4.1×10^{-14}	6.1×10^{-14}

Although approximate, the Einstein-Stokes diffusion equation correctly predicts the increased friction coefficients between permeants and fluid for rod shaped particles and typically yields a reasonably good match with experimental values. Note also that both FITC and CNT-FITC have negative charge and "acceleration" of nanotube transport cannot be attributed solely to favorable electrostatic interactions with cellular membranes. Furthermore, $\boldsymbol{D_a}$ of CNT-TGFβ1-FITC is equal to $(1.5\pm0.2)\times10^{-13}$ m^2/s markedly exceeding the diffusion

coefficients of both CNT-FITC and FITC, despite even greater $Mr = 6.84 \times 10^6$ Da. Note that diffusion of CNTs in blood, lymph, and bile[17] with $\boldsymbol{D_a}$ equal to $(0.59\pm0.18)\times10^{-14}$ m^2/s, $(1.45\pm0.65)\times10^{-14}$ m^2/s, and $(0.9\pm0.2)\times10^{-14}$ m^2/s, respectively, is considerably slower[17], which is also counterintuitive considering that these tissues are liquid. Experimental observations of CNT transport in dense bacterial biofilms[18] and glomerular membranes[19] confirm that nanotube transports in dense bio logical media is anomalous although might have been attributed to different causes.

The unexpectedly high diffusion coefficients on CNTs in dense tissues were puzzling and we decided to verify the permeation of CNT-TGFβ1-FITC through the 3D tissue models using microscopy techniques to avoid potential artifacts associated, with, for instance, the slow detachment of FITC from nanotubes. After 20 min of exposure of spheroids to CNTs-TGFβ1-FITC, the nanotubes were found to be imbedded in the cellular mass **(Figure 2.9a-c)**. The comparable scanning electron microscopy images of the spheroids prior to exposure to nanotube dispersion can be found in **Figure 2.2**. To verify permeation of CNTs to the central part of the spheroid, we also carried out histological sectioning of ICC scaffolds. CNTs can be found in SEM images of the slices of the spheroids obtained at middle focal plane ~38μm from the spheroid's surface (**Figure 2.9 e-f)** which agrees with permeation profiles in **Figure 2.7 a, c**.

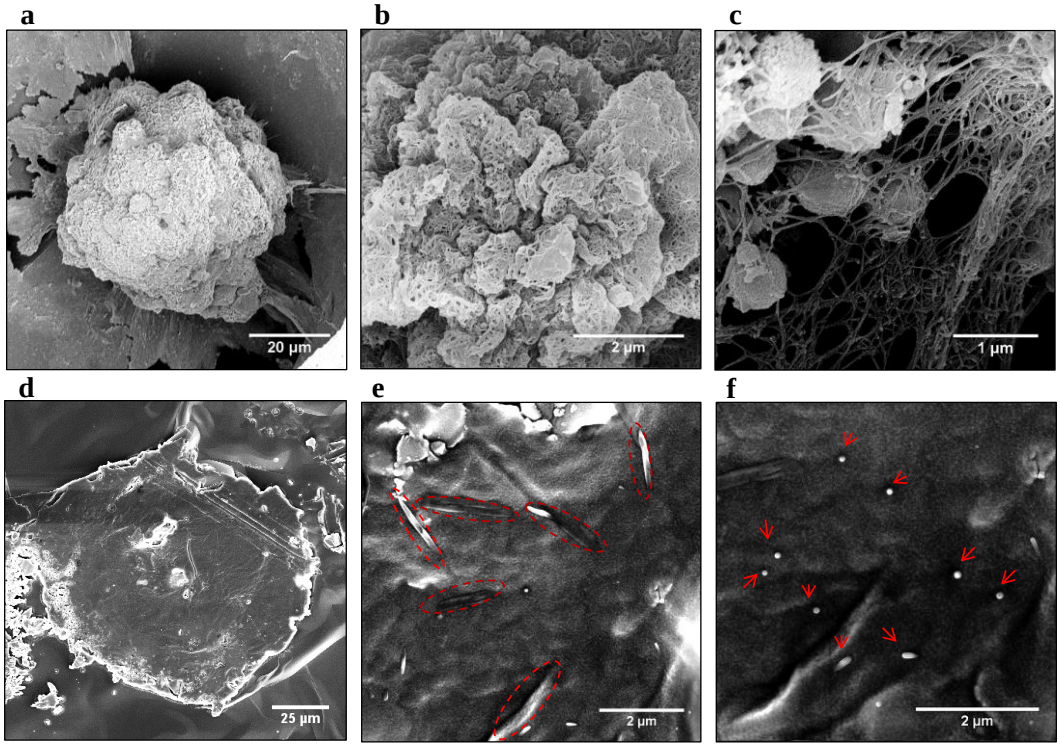

Figure 2.9 SEM images of HepG2 spheroids after exposure to CNT-TGFβ-FITC for 20 mins (a-c). The surface of the spheroid at different magnification. CNTs in all the images could not be washed off without physical destruction of the tissue model that indicated their penetration inside the cellular mass. **(d)** Histological sections of HepG2 cell cultures in ICC scaffolds with CNTs oriented predominantly in **(e)** parallel and **(f)** perpendicular alignment with the plane of sectioning.

2.5 Conclusions

The method described in this work enables accurate and systematically evaluation of the different modes of transport of CNTs and CNT-based drug delivery systems necessary for comprehensive pharmacokinetic models.[30] In the same manner, *in-vitro* 3D cell cultures with ICC scaffolds, which can easily apply to other molecules/nanoscale carriers, offers possibility for simple comparative studies between different drug carriers in the absence of complicating factors such as pharmacokinetics and metabolism.[31] Our results also indicates that it is important to design drug delivery systems such that they strike a balance between efficient diffusion and cellular affinity, ensuring that the therapeutic will transport deep within the tumor and accumulate in quantities sufficient to elicit a therapeutic effect. In the future study, incorporation of the physical and chemical parameters such as fluid flow and shear force into the 3D tissue model could be done to provide deeper insight into the effects of CNT-tissue on transport efficiency. Certainly, in addition to *in-vitro* study, the corresponding data from *in-vivo* studies and clinical evidence will be needed to standardize the data obtained from the 3D model for extensive clinical use.

2.6 Reference

(1) Feazell, R. P.; Nakayama-Ratchford, N.; Dai, H.; Lippard, S. J. Soluble Single-Walled Carbon Nanotubes as Longboat Delivery Systems for platinum(IV) Anticancer Drug Design. TL - 129. *J. Am. Chem. Soc.* **2007**, *129 VN* - , 8438–8439.

(2) Liu, Z.; Chen, K.; Davis, C.; Sherlock, S.; Cao, Q.; Chen, X.; Dai, H. Drug Delivery with Carbon Nanotubes for in Vivo Cancer Treatment. *Cancer Res.* **2008**, *68*, 6652–6660.

(3) Jain, R. K. Delivery of Molecular and Cellular Medicine to Solid tumors1PII of Original Article: S0169-409X(97)00027-6. The Article Was Originally Published in Advanced Drug Delivery Reviews 26 (1997) 71–90.1. *Adv. Drug Deliv. Rev.* **2001**, *46*, 149–168.

(4) Cheng, Y.; Morshed, R. A.; Auffinger, B.; Tobias, A. L.; Lesniak, M. S. Multifunctional Nanoparticles for Brain Tumor Imaging and Therapy. *Adv. Drug Deliv. Rev.* **2014**, *66*, 42–57.

(5) Mieszawska, A. J.; Mulder, W. J. M.; Fayad, Z. A.; Cormode, D. P. Multifunctional Gold Nanoparticles for Diagnosis and Therapy of Disease. *Mol. Pharm.* **2013**, *10*, 831–847.

(6) Yigit, M. V; Moore, A.; Medarova, Z. Magnetic Nanoparticles for Cancer Diagnosis and Therapy. *Pharm. Res.* **2012**, *29*, 1180–1188.

(7) Meng, L.; Zhang, X.; Lu, Q.; Fei, Z.; Dyson, P. J. Single Walled Carbon Nanotubes as Drug Delivery Vehicles: Targeting Doxorubicin to Tumors. *Biomaterials* **2012**, *33*, 1689–1698.

(8) Nair, L. V.; Nagaoka, Y.; Maekawa, T.; Sakthikumar, D.; Jayasree, R. S. Quantum Dot Tailored to Single Wall Carbon Nanotubes: A Multifunctional Hybrid Nanoconstruct for Cellular Imaging and Targeted Photothermal Therapy. *Small* **2014**, *10*, 2771–2775.

(9) Sanna, V.; Pala, N.; Sechi, M. Targeted Therapy Using Nanotechnology: Focus on Cancer. *Int. J. Nanomedicine* **2014**, *9*, 467–483.

(10) Fuchs, A. V; Tse, B. W. C.; Pearce, A. K.; Yeh, M.-C.; Fletcher, N. L.; Huang, S. S.; Heston, W. D.; Whittaker, A. K.; Russell, P. J.; Thurecht, K. J. Evaluation of Polymeric Nanomedicines Targeted to PSMA: Effect of Ligand on Targeting Efficiency. *Biomacromolecules* **2015**.

(11) Kai, M. P.; Keeler, A. W.; Perry, J. L.; Reuter, K. G.; Luft, J. C.; O'Neal, S. K.; Zamboni, W. C.; DeSimone, J. M. Evaluation of Drug Loading, Pharmacokinetic Behavior, and Toxicity of a Cisplatin-Containing Hydrogel Nanoparticle. *J. Control. Release* **2015**, *204*, 70–77.

(12) Moghimi, S. M.; Hunter, A. C.; Andresen, T. L. Factors Controlling Nanoparticle Pharmacokinetics: An Integrated Analysis and Perspective. *Annu. Rev. Pharmacol. Toxicol.* **2012**, *52*, 481–503.

(13) Larson, B.; Banks, P.; Sherman, H.; Rothenberg, M. Automation of Cell-Based Drug Absorption Assays in 96-Well Format Using Permeable Support Systems. *J. Lab. Autom.* **2012**, *17*, 222–232.

(14) Jin, H.; Heller, D. a; Strano, M. S. Single-Particle Tracking of Endocytosis and Exocytosis of Single-Walled Carbon Nanotubes in NIH-3T3 Cells. *Nano Lett.* **2008**, *8*, 1577–1585.

(15) Reuel, N. F.; Dupont, A.; Thouvenin, O.; Lamb, D. C.; Strano, M. S.; Reuel, B. N. F.; Dupont, A.; Thouvenin, O.; Lamb, D. C.; Strano, M. S. Three-Dimensional Tracking of Carbon Nanotubes within Living Cells. *ACS Nano* **2012**, *6*, 5420–5428.

(16) Current Limitations of Molecular Magnetic Resonance Imaging for Tumors as Evaluated With High-Relaxivity CD105-Specific Iron Oxide Nanoparticles. http://ovidsp.tx.ovid.com/sp-3.17.0a/ovidweb.cgi?T=JS&PAGE=fulltext&D=ovft&AN=00004424-201207000-00001&NEWS=N&CSC=Y&CHANNEL=PubMed (accessed Oct 2, 2015).

(17) Oszlánczi, G.; Vezér, T.; Sárközi, L.; Horváth, E.; Kónya, Z.; Papp, A. Functional Neurotoxicity of Mn-Containing Nanoparticles in Rats. *Ecotoxicol. Environ. Saf.* **2010**, *73*, 2004–2009.

(18) Scannell, J. W.; Blanckley, A.; Boldon, H.; Warrington, B. Diagnosing the Decline in Pharmaceutical R&D Efficiency. *Nat. Rev. Drug Discov.* **2012**, *11*, 191–200.

(19) Holmes, A.; Bonner, F.; Jones, D. Assessing Drug Safety in Human Tissues — What Are the Barriers? *Nat. Rev. Drug Discov.* **2015**, *14*, 1–3.

(20) Weissleder, R.; Nahrendorf, M.; Pittet, M. J. Imaging Macrophages with Nanoparticles. *Nat. Mater.* **2014**, *13*, 125–138.

(21) Hainfeld, J. F.; Slatkin, D. N.; Focella, T. M.; Smilowitz, H. M. Gold Nanoparticles: A New X-Ray Contrast Agent. *Br. J. Radiol.* **2006**, *79*, 248–253.

(22) Hertz, H. M.; Larsson, J. C.; Lundström, U.; Larsson, D. H.; Vogt, C. Laboratory X-Ray Fluorescence Tomography for High-Resolution Nanoparticle Bio-Imaging. *Opt. Lett.* **2014**, *39*, 2790–2793.

(23) Yang, Z.; Chen, J.; Yao, J.; Lin, R.; Meng, J.; Liu, C.; Yang, J.; Li, X.; Wang, L.; Song, L. Multi-Parametric Quantitative Microvascular Imaging with Optical-Resolution Photoacoustic Microscopy in Vivo. *Opt. Express* **2014**, *22*, 1500–1511.

(24) Hare, D. J.; New, E. J.; de Jonge, M. D.; McColl, G. Imaging Metals in Biology: Balancing Sensitivity, Selectivity and Spatial Resolution. *Chem. Soc. Rev.* **2015**, *44*, 5941–5958.

(25) Masuda, N.; Mizuno, A.; Rahman, M. M.; Arai, K.; Itoh, M. Abstract 303: Effect of Scaffold on Drug Sensitivity of Multicellular Spheroids: Which Method Is close to in Vivo and Suitable for HTS. *Cancer Res.* **2015**, *75*, 303–303.

(26) Liu, T.; Winter, M.; Thierry, B. Quasi-Spherical Microwells on Superhydrophobic Substrates for Long Term Culture of Multicellular Spheroids and High Throughput Assays. *Biomaterials* **2014**, *35*, 6060–6068.

(27) Charoen, K. M.; Fallica, B.; Colson, Y. L.; Zaman, M. H.; Grinstaff, M. W. Embedded Multicellular Spheroids as a Biomimetic 3D Cancer Model for Evaluating Drug and Drug-Device Combinations. *Biomaterials* **2014**, *35*, 2264–2271.

(28) Sapp, M. C.; Fares, H. J.; Estrada, A. C.; Grande-Allen, K. J. Multilayer Three-Dimensional Filter Paper Constructs for the Culture and Analysis of Aortic Valvular Interstitial Cells. *Acta Biomater.* **2015**, *13*, 199–206.

(29) Yohan, D.; Cruje, C.; Lu, X.; Chithrani, D. Elucidating the Uptake and Distribution of Nanoparticles in Solid Tumors via a Multilayered Cell Culture Model. *Nano-Micro Lett.* **2015**, *7*, 127–137.

(30) Goodman, T. T.; Olive, P. L.; Pun, S. H. Increased Nanoparticle Penetration in Collagenase-Treated Multicellular Spheroids. *Int. J. Nanomedicine* **2007**, *2*, 265–274.

(31) Kostarelos, K.; Emfietzoglou, D.; Papakostas, A.; Yang, W.-H.; Ballangrud, A.; Sgouros, G. Binding and Interstitial Penetration of Liposomes within Avascular Tumor Spheroids. *Int. J. Cancer* **2004**, *112*, 713–721.

(32) Tomei, A. A.; Choe, M. M.; Swartz, M. A. Effects of Dynamic Compression on Lentiviral Transduction in an in Vitro Airway Wall Model. *Am. J. Physiol. Lung Cell. Mol. Physiol.* **2008**, *294*, L79–L86.

(33) Nel, A. E.; Mädler, L.; Velegol, D.; Xia, T.; Hoek, E. M. V; Somasundaran, P.; Klaessig, F.; Castranova, V.; Thompson, M. Understanding Biophysicochemical Interactions at the Nano-Bio Interface. *Nat. Mater.* **2009**, *8*, 543–557.

(34) Lee, J.; Lilly, G. D.; Doty, R. C.; Podsiadlo, P.; Kotov, N. A. In Vitro Toxicity Testing of Nanoparticles in 3D Cell Culture. *Small* **2009**, *5*, 1213–1221.

(35) John William Judkins. Carbon Nanotube Diffusion under Simulated

Physiological Conditions. *Cornell Hotel Restaur. Adm. Q.* **2010**, *22*, 64–64.

(36) Katayama, K.; Nomura, H.; Ogata, H.; Eitoku, T. Diffusion Coefficients for Nanoparticles under Flow and Stop-Flow Conditions. *Phys. Chem. Chem. Phys.* **2009**, *11*, 10494–10499.

(37) Pinheiro, J. P.; Domingos, R.; Lopez, R.; Brayner, R.; Fiévet, F.; Wilkinson, K. Determination of Diffusion Coefficients of Nanoparticles and Humic Substances Using Scanning Stripping Chronopotentiometry (SSCP). *Colloids Surfaces A Physicochem. Eng. Asp.* **2007**, *295*, 200–208.

(38) Lee, J.; Cuddihy, M. J.; Cater, G. M.; Kotov, N. a. Engineering Liver Tissue Spheroids with Inverted Colloidal Crystal Scaffolds. *Biomaterials* **2009**, *30*, 4687–4694.

(39) Shim, M.; Shi Kam, N. W.; Chen, R. J.; Li, Y.; Dai, H. Functionalization of Carbon Nanotubes for Biocompatibility and Biomolecular Recognition. *Nano Lett.* **2002**, *2*, 285–288.

(40) Smart, S. K.; Cassady, A. I.; Lu, G. Q.; Martin, D. J. The Biocompatibility of Carbon Nanotubes. *Carbon N. Y.* **2006**, *44*, 1034–1047.

(41) Wong, C.; Stylianopoulos, T.; Cui, J.; Martin, J.; Chauhan, V. P.; Jiang, W.; Popovic, Z.; Jain, R. K.; Bawendi, M. G.; Fukumura, D. Multistage Nanoparticle Delivery System for Deep Penetration into Tumor Tissue. *Proc. Natl. Acad. Sci. U. S. A.* **2011**, *108*, 2426–2431.

(42) Li, X.; Fan, Y.; Watari, F. Current Investigations into Carbon Nanotubes for Biomedical Application. *Biomed. Mater.* **2010**, *5*, 022001.

(43) Methods in Molecular Biophysics | Biological Physics and Soft Matter Physics | Cambridge University Press http://www.cambridge.org/US/academic/subjects/physics/biological-physics-and-soft-matter-physics/methods-molecular-biophysics-structure-dynamics-function (accessed Oct 5, 2015).

(44) Yang, M.; Alvarez-Puebla, R.; Kim, H.-S.; Aldeanueva-Potel, P.; Liz-

Marzán, L. M.; Kotov, N. a. SERS-Active Gold Lace Nanoshells with Built-in Hotspots. *Nano Lett.* **2010**, *10*, 4013–4019.

Appendix 2.1 ***Mathematica*** **Code for Data Processing** (Example: one set of data from images in main text**)**

```
c0 = 0.0005 (* Initial concentration *)
0.0005

ct[x_, t_, d_] := c0 * x * (Exp[-x^2 / (4 t * d)]) / (2 * Sqrt[π * t * d])
(* Define concentration function to distance x (m),
time t (s) and diffusion coefficient d based on solutions of
 Equation (1) and derived from one dimensional diffusion solution*)

gradient = D[ct[x, t, d], {{x}}]
    (* Function of gradient *)
```

$$\left\{\frac{0.000141047\, e^{-\frac{x^2}{4dt}}}{\sqrt{d\,t}} - \frac{0.0000705237\, e^{-\frac{x^2}{4dt}} x^2}{d\,t\sqrt{d\,t}}\right\}$$

```
Dgradient = D[ct[x, t, d], {{x}, 2}][[1]]
 (* Define function of Dgradient to distance, time and diffusion coefficient *)
```

$$\left\{-\frac{0.000211571\, e^{-\frac{x^2}{4dt}} x}{d\,t\sqrt{d\,t}} + \frac{0.0000352618\, e^{-\frac{x^2}{4dt}} x^3}{d^2\,t^2\sqrt{d\,t}}\right\}$$

```
Solve [Dgradient == 0, x]
```

$$\left\{\{x \to 0.`\}, \left\{x \to -2.449489742783178` \sqrt{d}\ \sqrt{t}\right\}, \left\{x \to 2.449489742783178` \sqrt{d}\ \sqrt{t}\right\}\right\}$$

```
(*when the gradient change reach the peak,
the equation (2) can be derived from equation (1) *)

t1 = 1200
t2 = 2400
t3 = 3600
t4 = 4800
t5 = 6000
t6 = 7200
 (* time point as seconds "s" *)

x1 = 0.0000114
x2 = 0.0000369
x3 = 0.0000372
x4 = 0.0000409
x5 = 0.0000409
x6 = 0.0000454

(* depth data from images (meter "m") *)
```

```
(({2.44949` √d √t /. t → t1} - x1)^2 + ({2.44949` √d √t /. t → t2} - x2)^2 +
 ({2.44949` √d √t /. t → t3} - x3)^2 + ({2.44949` √d √t /. t → t4} - x4)^2 +
 ({2.44949` √d √t /. t → t5} - x5)^2 + ({2.44949` √d √t /. t → t6} - x6)^2
{(-0.0000114 + 84.8528 √d)^2 + (-0.0000369 + 120. √d)^2 +
  (-0.0000372 + 146.969 √d)^2 + (-0.0000409 + 169.706 √d)^2 +
  (-0.0000409 + 189.737 √d)^2 + (-0.0000454 + 207.846 √d)^2}

(*Least square method to fined the best diffusion coefficient*)

Dvalue = D[{{{(-0.0000114` + 84.85282265263778` √d)^2 +
      (-0.0000369` + 120.00001260099934` √d)^2 +
      (-0.0000372` + 146.9694` √d)^2 + (-0.0000409` + 169.70564530527557` √d)^2 +
      (-0.0000409` + 189.73667953403213` √d)^2 +
      (-0.0000454` + 207.8461187338364` √d)^2}}, {{d}}]
{{{{84.8528 (-0.0000114 + 84.8528 √d)}/√d + {120. (-0.0000369 + 120. √d)}/√d +
    {146.969 (-0.0000372 + 146.969 √d)}/√d + {169.706 (-0.0000409 + 169.706 √d)}/√d +
    {189.737 (-0.0000409 + 189.737 √d)}/√d + {207.846 (-0.0000454 + 207.846 √d)}/√d}}}

Solve[1/√d 84.85282265263778` (-0.0000114` + 84.85282265263778` √d) +
  1/√d 120.00001260099934` (-0.0000369` + 120.00001260099934` √d) +
  {146.9694` (-0.0000372` + 146.9694` √d)}/√d + 1/√d
  169.70564530527557` (-0.0000409` + 169.70564530527557` √d) + 1/√d
  189.73667953403213` (-0.0000409` + 189.73667953403213` √d) + 1/√d
  207.8461187338364` (-0.0000454` + 207.8461187338364` √d) == 0, d]
{{d → 5.35836 × 10^-14}}
```

In[155]:=
```
(*Plot the Depth vesus Time*)
Solve[D[ct[x, t, d], {{x}, 2}][[1]][[1]] == 0, {x}]
```

In[156]:=
$$\left\{\{x \to 0.`\}, \left\{x \to -2.449489742783178` \sqrt{d}\ \sqrt{t}\right\}, \left\{x \to 2.449489742783178` \sqrt{d}\ \sqrt{t}\right\}\right\}$$

In[157]:=
```
kk = D[ct[x, t, d], {{x}}][[1]] /. {d → 5.35836206921357`*^-14, t → 1200}
```

Out[157]=
$$17.5897\, e^{-3.888\times10^{9}\, x^2} - 1.36778\times10^{11}\, e^{-3.888\times10^{9}\, x^2}\, x^2$$

In[159]:=
```
Plot[Sqrt[6 * d * t] /. {d → 5.35836206921357`*^-14}, {t, 0, 7200}]
```

Out[159]=

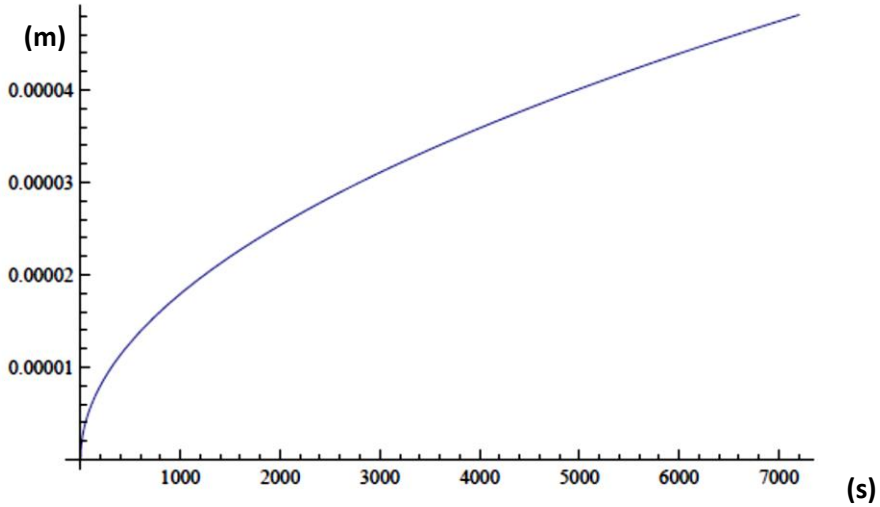

Chapter III

Transport of Carbon Nanotubes in Cellular Spheroid:

A Simulation Study

3.1 Abstract

Anomalously fast diffusion of targeted carbon nanotubes (CNTs) has been investigated within cellular spheroid as classic diffusion in previous chapter. However, why CNTs modified with targeting ligand diffuse faster is still obscure. In this chapter, we hypothesized that in the dense tissue/tumor with high chance of cellular membrane binding, anomalous diffusion occurs due to surface diffusion on the membrane, in which the mean-square displacement is not only proportional to an integral power of time in three dimensional space. The results from cell-CNT

interaction *in vitro* and diffusion coefficient data fitting in equation of two-phase diffusion proved that the fast diffusion of CNTs is the consequence of the planar diffusion along cellular membranes, which reduced effective dimensionality of diffusional space. Furthermore, to better understand the transport properties of CNT in dense tissue, we discussed simulated models incorporated with binding and surface diffusion in which immobile cells in spheroid are represented by obstacles that bind diffusing CNT in nearest-neighbor sites. Random Walks in two phases are utilized in the simulation. The result indicated anomalous diffusion of CNTs is associated with affinity of CNT with cell membrane regarding to distribution coefficient $\boldsymbol{K}$ of the simulated CNT between lipids and interstitial liquid at equilibrium conditions. In addition, it is highly dependent on the void volume ($\boldsymbol{\phi}$ and $\boldsymbol{a_v}$) of the simulated structure which shall be related to specific tissue structure.

3.2 Introduction

Carbon nanotubes (CNTs) have been considered as a promising nano-sized pharmaceutical agent for drug delivery and imaging application. [1, 2, 3] The use of CNTs as deliver cargo to deep tissue/tumor has attracted considerable interest. It has been shown in recent study that apparent diffusion coefficients of targeted CNTs in three-dimensional (3D) cell culture *in vitro* are anomalously high and comparable to diffusion rates of similarly charged molecules with much lower molecular weights[4]. Hence, although diffusion of CNTs in dense tissue have not

yet been used *in vivo*, nanotubes are promising as anticancer agents for fast and deep permeation into the hypoxia region of tissue/tumor.[5] Understanding of their transport through complex 3D tissues both fundamentally and practically is an important consideration for pharmacodynamics analysis to validate drug doses and administration regimens required to achieve desired therapeutic effects. [6,7]

The current studies of nano-sized agent transport are focused on biodistribution or local accumulation experimentally, of which the data were obtained with widely different protocols due to variety of animals, drug doses, and evaluation methods.[8] Therefore, numerous effort was brought to measure or simulate diffusivity of these agents in homogeneous physiological media according to the rules of unobstructed free diffusion.[9] Such that, the mean-square displacement of the diffusing particle is proportional to time as in Brownian diffusion. Furthermore, if CNTs are used as local injection into dense tissue or tumor focus, in classical model it is always considered intercellular diffusion and CNT-cell interaction including binding and internalization. While in dense tissue/tumor, obstruction by or interaction with the cells may lead to anomalous diffusion, in which diffusion is usually considered being hindered.[10,11,12] As a result, in the obstructed space, CNTs should have diffused slower than free diffusion. However, the experimental results have indicated that diffusivity diffusion of targeted CNTs enhanced in dense tissue structure.

The fundamental mechanism of enhanced targeted CNT transport is still unclear. For instance, how does enhanced CNTs diffusion occur in dense tissue with cellular obstructions? Does cellular membrane diffusion influence anomalous diffusion in dense tissue under the equilibrium state of binding/unbinding? What feature(s) is essential for CNT diffusivity? In this chapter, we hypothesize that in the dense tissue/tumor with high chance of cellular membrane binding, anomalous diffusion occurs due to surface diffusion on the membrane, in which the mean-square displacement is not only proportional to an integral power of time in three dimensional space. Cell-CNT interaction was examined by 2D cell culture *in vitro* to support the assumption of CNT binding/unbinding equilibrium in the environment. Diffusion coefficient data in previous study was extracted for data fitting in equation of two-phase diffusion. The results proved that the fast diffusion of CNTs is the consequence of the planar diffusion along cellular membranes, which reduced effective dimensionality of diffusional space.

The effect of planar diffusion on CNT transport was highly related to the affinity of permeant and volume fraction of the dense tissue. In order to understand how these factors associate with apparent diffusion coefficient of CNTs, the computational models with conditioned cellular structure and permeates was built according to the experimental microenvironment of dense tumor tissue. Simulated cellular spheroid structure was created by inert designed spheres according to experimental model. The computational Monte-Carlo sampling and analysis of conditioned microenvironment are coupled with the standardized and uniform-

sized liver tumor spheroids culture model in Inverted Colloidal Crystal (ICC) scaffolds *in vitro* for experimental study in **Chapter 2** and provided identification or validation of predictive drug transport and efficacy. The simulation result presented here shows the affinity of CNTs with cellular membrane (***K***) is essential for the effective diffusivity in dense tissue. In addition, both actual apparent diffusion in spheroid culture and simulated displacement in two-phase diffusion model, apparent diffusivity is highly depending on the interstitial space and cellular structure such as void fraction (***ϕ***).

3.3 Materials and Methods

3.3.1 Cellular Spheroid Cultured in ICC Scaffold

Realistic models of this study, Cellular spheroids, were formed by liver hepatocellular carcinoma cells (HepG2, ATCC, VA) in ICC scaffold. [4,12] The geometry of ICC scaffold is shown as hexagonally packed uniform spherical cavities connected to each other, while material of the scaffold is made of polyacrylamide. [4,12] As a result, mono-dispersed spheroids are nearly perfectly formed by seeding a 25 μl of dense cell suspension (2×10^7 cells/ml) and culturing for 5 days (**Figure 3.1a**). The cells were stained with Viability/Cytotoxicity assay (Life Technologies, US) to indicate live (green-fluorescent) from dead cells (red-fluorescent) by simultaneously staining with calcein-AM to indicate intracellular

esterase activity and ethidium homodimer-1. Mature spheroids include the extracellular matrix coating on their surface (**Figure 3.1b**). The final realistic model yield HepG2 cellular spheroids with average diameter of 141.9 ± 5.6 μm including 500-600 cells.

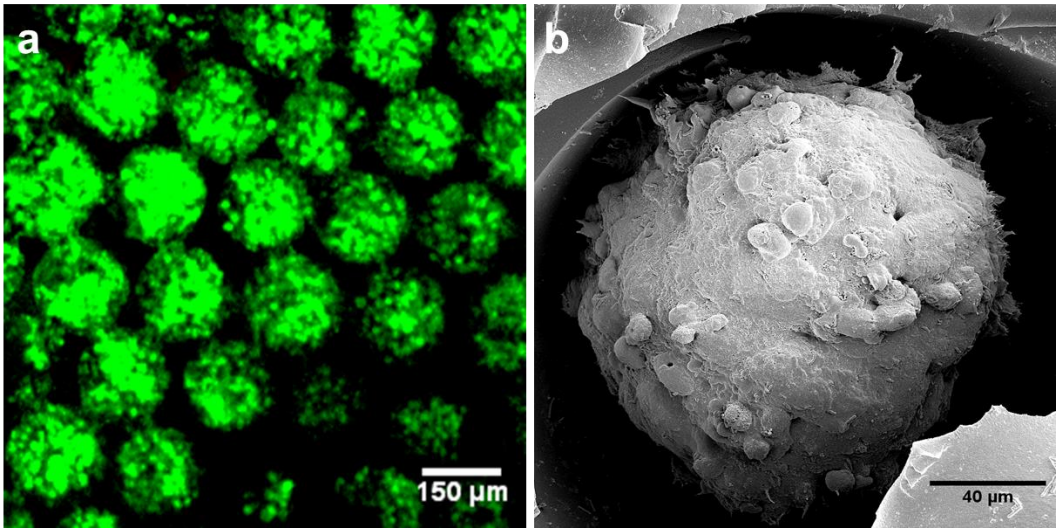

Figure 3.1 Cellular Spheroids in realistic model. **(a)** Confocal microscope image of uniform cellular spheroids formed in ICC scaffold: cells were stained with Viability/Cytotoxicity assay where live cells are green fluorescent and dead cells are red fluorescent. **(b)** Characterization image of mature cellular spheroid taken by SEM shows extracellular matrix covered on the surface.

3.3.2 Simulated Cellular Spheroid Structure

To simulate the transport of CNTs in the practical model, the computational model of cellular spheroid is built in a range of 142 μm referring to the average diamter of realistic model in ***x***, ***y*** and ***z*** axises, and the model consists of spheres as

individual cells in the grid (**Figure 3.2a**). The diameter of sphere corresponds to average value of indiviual HepG2 cell as 9μm.[13] The minimum distance between spheres is coresponding to the interstitial space with diameter of 1.34μm[9].

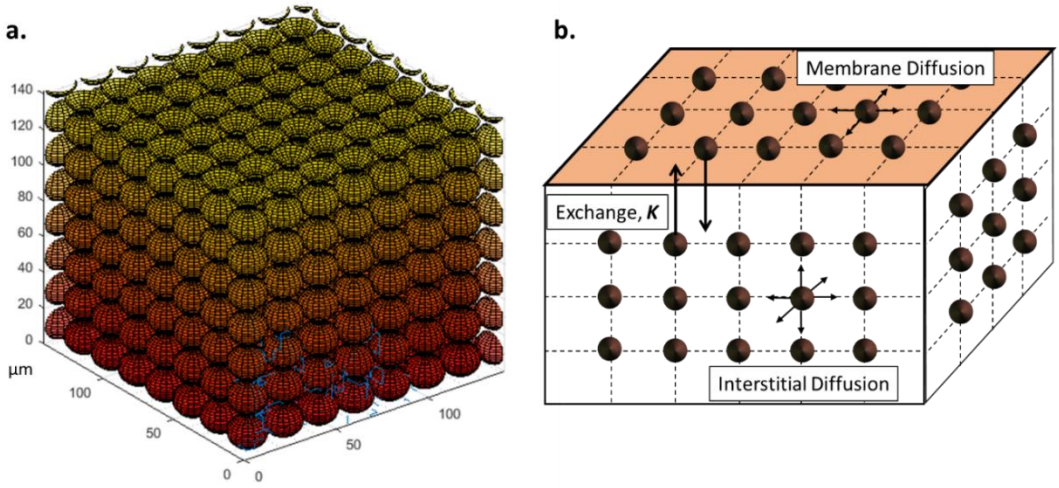

Figure 3.2 Computational model of cellular spheroid is built in Matlab with spheres as individual cells **(a)**. Transport of CNTs is simulated as in the scheme **(b)** where nanotubes as black dots in the grid undergo surface diffusion on the membrane and 3D diffusion in the interstitial space.

As a result, this simulated model contained 512 cells with the void fraction of 56.4%, within the range of medical observation of 50%-80%.[14] The scheme (**Figure 3.2b**) represents the model for simulations of CNT diffusion in interstitial space and/or membrane surface, as well as its interaction with cell membrane. The CNTs undergo 3D diffusion as 3D random walk in a cubic volume, and bind reversibly (with the kinetic equilibrium constants ***K***) to one of the volume

boundaries, representing the cell membrane. The bound CNT is allowed to be mobile as planar diffusion as 2D random walk.

3.3.3 Monte-Carlo Simulations of CNT Diffusion by Random Walks

In this simulation, an apparent diffusivity $\boldsymbol{D_a}$ can be described in terms of the diffusivities associated with an equivalent capillary and of tortuosity factors for the void and surface phases. These properties are determined by the model structure built in simulation. Based on assumptions of association-dissociation equilibrium ($\boldsymbol{K}$)[15] in the system

$$\boldsymbol{D_a = \frac{D_i \phi}{\tau_i} + \frac{D_{mem}}{\tau_{mem}} a_v K} \qquad \textbf{Eq 3.1}$$

where $\boldsymbol{D_i}$ and $\boldsymbol{D_{mem}}$ are interstitial phase diffusivity and cell membrane surface diffusivity, in equivalent capillaries. The terms $\boldsymbol{\tau_i}$ and $\boldsymbol{\tau_{mem}}$ denote the void and surface tortuosities, defined as the length of the equivalent capillary required in order to describe effective diffusivities in the void and surface phases, respectively. These two factors depend on the structure in simulated obstructs. $\boldsymbol{\phi}$ is void fraction of tumor. $\boldsymbol{a_v}$ is volume ratio (cylinder layer-cell membrane to capillary-interstitial layer). Therefore, transport of CNT within dense tissue can be described as interstitial and cell membrane surface two-phase diffusion within the structure

associated with $\boldsymbol{\tau}$, $\boldsymbol{\phi}$ and $\boldsymbol{a_v}$. [16,17] According to the practical diffusivity of CNTs in multimedia, $\boldsymbol{D_i}$ = (1.45 ± 0.7)×10^{-2} $\mu m^2/s$ in plasma[9] and $\boldsymbol{D_{mem}}$ = (2.3±0.7) $\mu m^2/s$ [13] were used in the simulation.

The diffusion was treated in terms of random walks, and the expected value of apparent diffusion coefficient $\boldsymbol{D_a}$ was computed using a Monte–Carlo algorithm, Metropolis–Hastings algorithm, with an average step size determined by the diffusion coefficient $\boldsymbol{D_i}$ and $\boldsymbol{D_{mem}}$. CNTs are initially placed at the starting position within 10nm from the simulated tissue model. As a result, the nanotubes located in void space are allowed to move as described below. Each simulation monitors the cumulative mean squared displacement of a thousand CNTs, ***MSD***, of 5.3μm^2 /walk in interstitial space and 828 μm^2/walk on the membrane with curvature based on assumptions of association-dissociation equilibrium (***K***). $\boldsymbol{D_a}$ is given by the Einstein equation in three dimensions:

$$\boldsymbol{D_a = \frac{\langle MSD \rangle}{6t}} \qquad \textbf{Eq 3.2}$$

in which ***t*** is the walking steps of random walks and representative of one second.

3.3.4 Markov chain of the algorithm in CNT random walks

The possible move in the Markov chain of this algorithm in the simulation was described as below (**Figure 3.3**):

Start of point ***p0*** at ***t0*** is in intercellular space

i. go to position ***p1*** at ***t1*** and then go to ***p2*** position at ***t2*** in intercellular space. → **ii/iv**

ii. go to position ***p1*** reversibly bind to the membrane at ***t1*** and then go to ***p2*** on the membrane at ***t2***. → **iii/iv**

iii. go to position ***p3*** on the membrane at ***t3***. → **ii/iv**

iv. go to position ***p3*** into intercellular space at ***t3***. → **ii/v**

v. go to position ***p1*** at ***t1*** and then go to ***p2*** back into intercellular space at ***t2***.

where ***p0***, ***p1***, ***p2*** and ***p3*** are the positions in the grid at time ***t0***, ***t1***, ***t2*** and ***t3***.

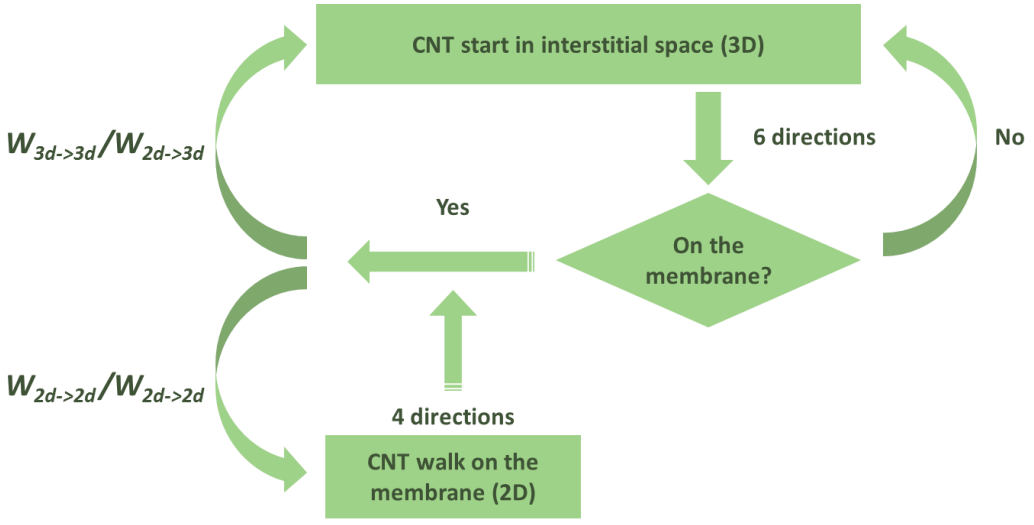

Figure 3.3 Flow chart of Markov chain by Metropolis–Hastings algorithm for random walks of CNTs. Transition probability of status is shown as W, associated with affinity of moving CNT, ***K***, and qualified for detailed balance in the Metropolis algorithm.

3.3.5 Proof of Detailed Balance in the Metropolis–Hastings algorithm

$$\frac{k_a}{k_a + k_d} W_{2\to3} + \frac{k_d}{k_a + k_d} W_{3\to3} = \frac{k_d}{k_a + k_d}$$

$$\frac{k_d}{k_a + k_d} W_{3\to2} + \frac{k_a}{k_a + k_d} W_{2\to2} = \frac{k_a}{k_a + k_d}$$

$$W_{2\to3} + W_{2\to2} = 1$$

$$W_{3\to3} + W_{3\to2} = 1$$

$$W_{2\to3} = W_{3\to3} = \frac{1}{K+1}$$

$$W_{3\to3} = W_{2\to3} = \frac{K}{K+1}$$

3.4 Result and Discussion

The collected microscopy and calculation data in **Chapter 2** indicate that biochemical interaction CNTs with the tissue model are likely to strongly alter their transport compared to purely Brownian diffusion.[20] Let us now consider possible pathways of CNT transport in the cellular spheroids. CNTs can permeate through the interstitial space and across/along the cell membranes.[7,21] In addition, the transport process is also influenced by the interaction of CNTs with extracellular matrix (ECM) and living cells, which is expected to affect their mobility in

tissues.[22] The transport processes at the cellular interface include adsorption to the cellular membrane, surface diffusion, desorption from the cellular membrane, endocytosis, and exocytosis (**Figure 3.4)**.

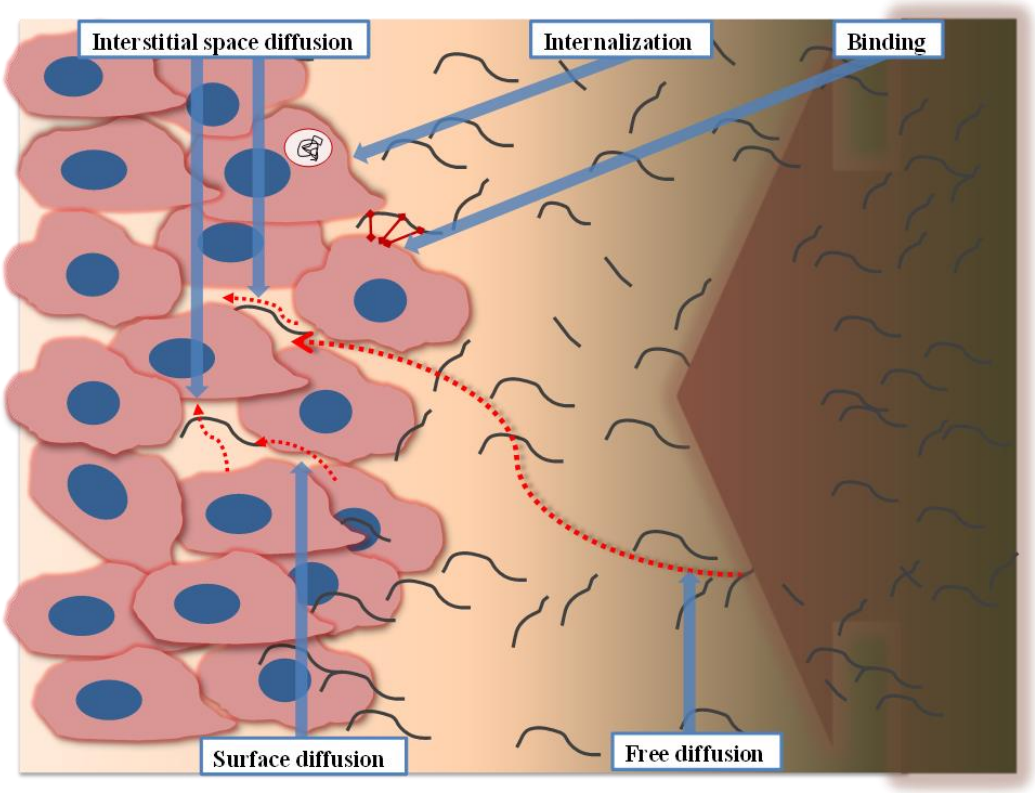

Figure 3.4 Transport mechanisms governing CNT penetration through tissues.

3.4.1 Transport based on cell-CNT interaction

The transport of CNTs in tissue can cumulatively be described by an equation

$$\frac{\partial Cex}{\partial t} = \nabla \cdot (\boldsymbol{D_{ex}} \nabla \boldsymbol{C_{ex}} - \boldsymbol{u C_{ex}}) - \boldsymbol{R} \qquad \textbf{Eq 3.3}$$

where the concentration of CNT in interstitial/extracellular space is $\boldsymbol{C_{ex}}$ and $\boldsymbol{u}$ is convection coefficient.[18] $\boldsymbol{D_{ex}}$ is diffusion coefficient in the extracellular spaces, approximated as homogeneous aqueous media [19, 20]. Biological interactions of the CNTs with the ECM and cellular membrane including adsorption, surface diffusion, desorption, endocytosis, and exocytosis are represent by the reaction term $\boldsymbol{R}$ [21]. Diffusion conditions specific for tissue model allow us to simplify **Eq 3.3**. Firstly, ICC scaffolds prevent macroscopic fluid flow and, thus, convection term $\boldsymbol{u C_{ex}}$ can be eliminated. Secondly, within the 120 min of our experiment, exocytosis component of the term $\boldsymbol{R}$ of CNT has minimum effect on transport process as reported by Strano *et al*.[19] The remaining components of $\boldsymbol{R}$ for CNTs-FITC and CNTs-TGFβ1-FITC can be evaluated in 2D cell culture.

Previous studies showed that surface properties of CNTs have an effect on cell internalization and excretion of nanoparticles and molecules.[22] To determine how the different surfaces of CNTs influenced their interactions with cell membranes and to quantify endocytosis component of $\boldsymbol{R}$, we first blocked the energy-enabled membrane transport of cells for the CNTs and their derivatives with

FITC by treating the cells with sodium azide and 2-deoxyglucose. HepG2 cells were incubated with CNTs-FITC and CNTs-TGFβ1-FITC at both 4°C and 37°C for 1 hour. Statistically identical small amounts of CNTs-FITC and CNTs-TGFβ1-FITC were internalized by cells for both experimental conditions (**Figure 3.5-7**).

Subsequently, we carried out confocal fluorescence microscopy studies of their uptake and intracellular distribution in living cells without endocytosis (**Figure 3.6**). By analysis of confocal images, it was found that without endocytosis, CNTs and their derivatives can both penetrate into cells by direct insertion. When the temperature decreased, the lipid membrane become rigid and reduced the penetration amount of CNTs. Moreover, fewer CNTs with ligands penetrated into cells through transient pores than regular ones. With blockage of an energy source and thus the endocytosis, the internalization of CNTs is theoretically through lipid-membrane fusion only[23]. The results shows internalization of CNT-TGFβ1-FITC were lower than that of CNT-FITC. Meanwhile, the ratio of endocytosis at normal status was measured by staining and counting endosomes in cells. The images (**Figure 3.7)** implicated CNT with targeting ligand were internalized more by endocytosis whereas CNT-FITC interacted with cells by a lipid-assisted mechanism for passive insertion without energy supplement. This is potentially due to the shapes of CNTs; that CNTs as elongated tubes are able to penetrate through the plasma membrane with lipid-membrane fusion, as a 'nanosyringe',[23] which is dependent on their hydrophobicity and stability (**Figure 3.8**) culture

media.[24] This property of nanosyringe possibly hindered CNTs moving forward by free diffusion.

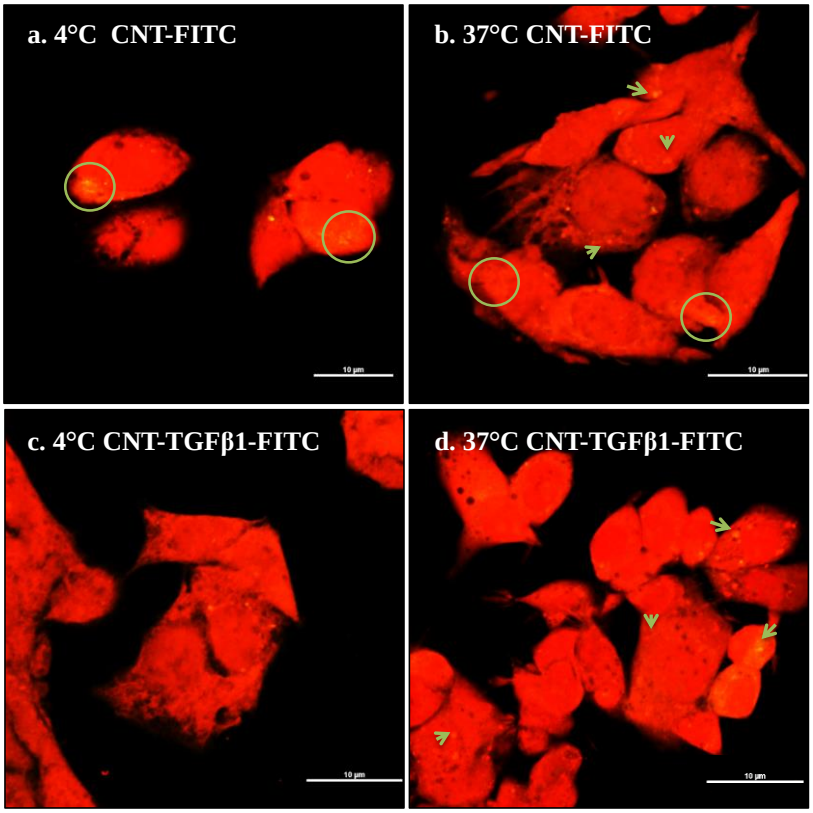

Figure 3.5 Encocytotic internalization of CNT penetrants in 2D cell cultures.(a-d) Confocal microscopy images of HepG2 cells after incubation for 1 hour in serum-free medium with 0.5mg/ml of CNTs-FITC (a,b) or CNTs-TGFβ1-FITC (c,d) at 4°C (a,c) and at 37°C (b,d). All scale bars are 10μm. (e) Quantification of CNTs-FITC and CNTs-TGFβ1-FITC internalized by cells at 4°C and 37°C. The percentage in (e) refers to fluorescent area fraction of CNTs (green) to cells (red).

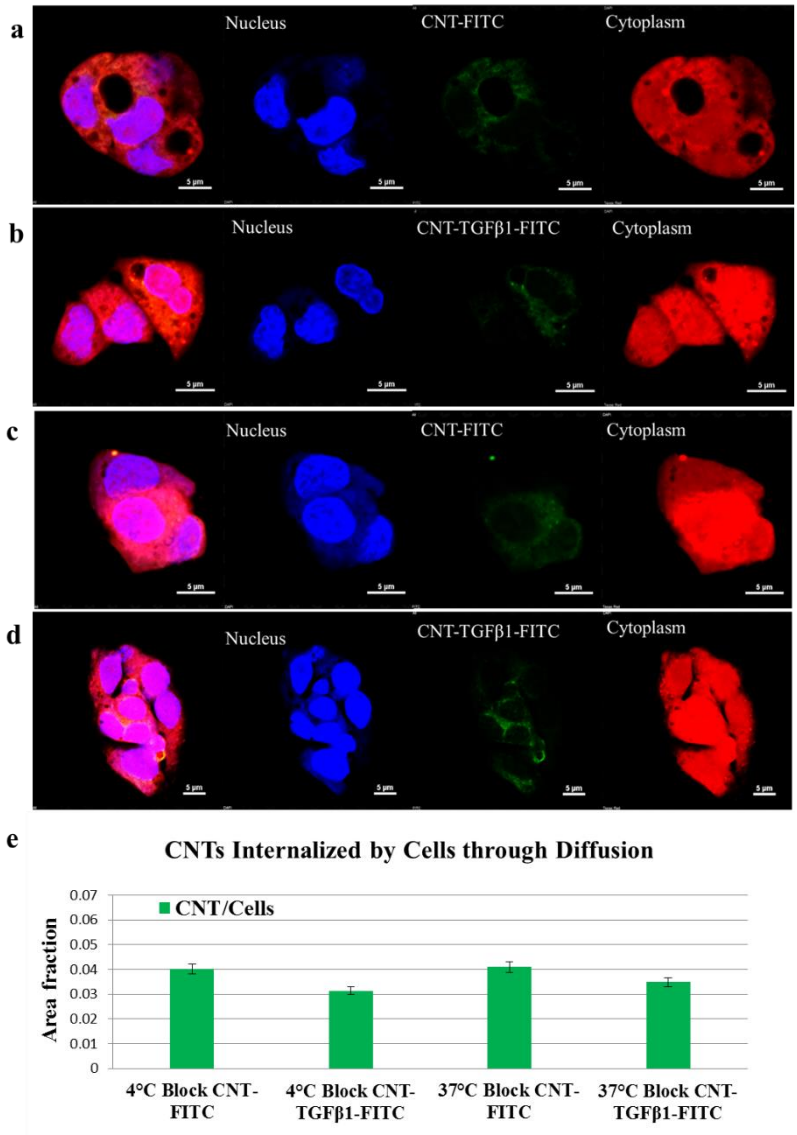

Figure 3.6 CNTs-FITC and their derivatives CNTs-TGFβ1-FITC entering cells at 4 °C and 37 °C under conditions where active internalization processes are blocked in the presence of azide and 2-deoxyglucose. HepG2 cells were incubated for 20 min in serum-free medium with CNTs-FITC (a) or CNTs-TGFβ1-FITC (b) at 4 °C and with CNTs-FITC (c) or CNTs-TGFβ1-FITC (d) at 37 °C. Area fraction of CNTs and their derivatives were calculated (e). Nuclei were stained with DAPI (blue) while the cytoplasm was stained with CellTracker™ CMRA (orange-red). Scale bars: 5 μm.

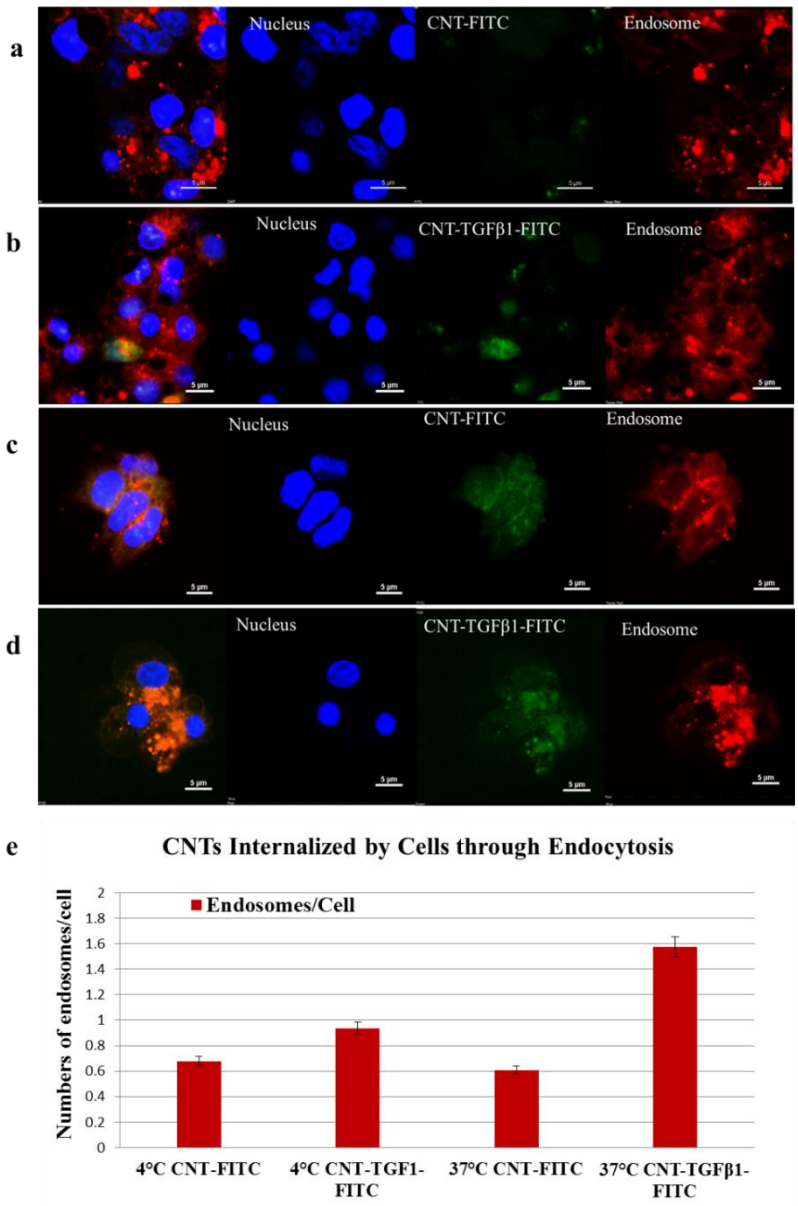

Figure 3.7 Quantification of CNTs-FITC and their derivatives CNTs-TGFβ1-FITC entering cells by endocytosis at 4 °C and 37 °C. HepG2 cells were incubated for 20 min in serum-free medium with CNTs-FITC (a) or CNTs-TGFβ1-FITC b) at 4 °C and with CNTs-FITC (c) or CNTs-TGFβ1-FITC (d) at 37 °C. Nuclei were counterstained with DAPI (blue) and early endosomes are marked with early Endosomes-RFP. Endosomes were counted and shown in (e). Scale bars: 5 μm.

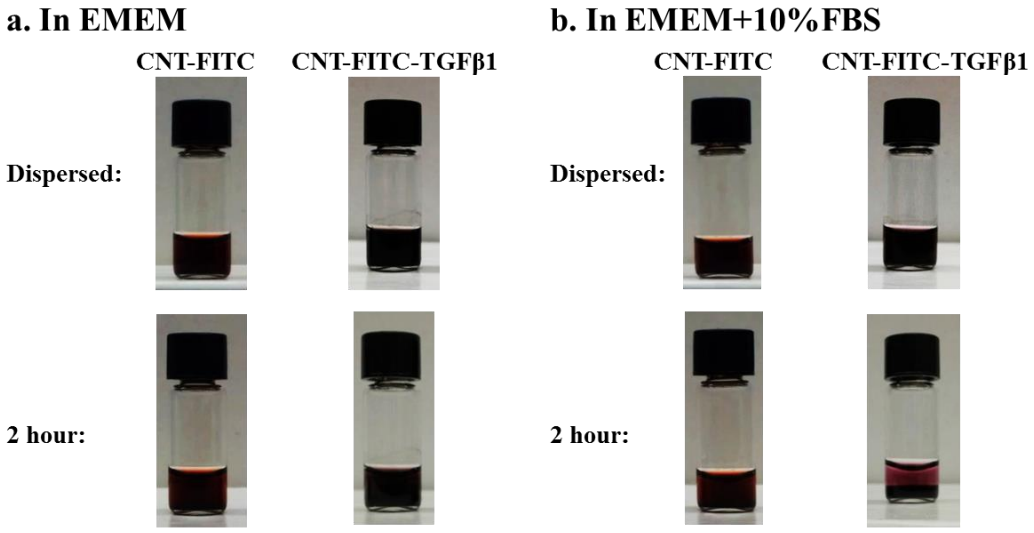

Figure 3.8 Stability of CNTs-FITC and CNTs-TGFβ1-FITC in EMEM without (**a**) and with (**b**) FBS of CNTs-FITC and CNTs-TGFβ1-FITC after 2 hours.

3.4.2 Calculation of equilibrium constants

Endocytosis term in ***R*** of **Eq 3.3** for these permeants can be neglected in this tissue model and period of CNT diffusion experiment since endocytosis is arrested at 4°C. Therefore, adsorption to, surface diffusion on, and desorption from the cellular membranes of CNTs have made the primary contributions to ***R.*** The original equation can be re-written then as a system of differential equations:

$$\begin{cases} \dfrac{\partial C_{ex}}{\partial t} + \dfrac{\partial C_{mem}}{\partial t} = \nabla \cdot (D_{ex}\, \nabla C_{ex}) + \nabla' \cdot (D_{mem}\, \nabla' C_{mem}) - (k_a\, C_{ex} - k_d\, C_{mem}) & \textbf{Eq 3.4} \\ \dfrac{\partial C_{ex}}{\partial t} = \nabla \cdot (D_{ex}\, \nabla C_{ex}) & \textbf{Eq 3.5} \\ \dfrac{\partial C_{mem}}{\partial t} = \nabla' \cdot (D_{mem}\, \nabla' C_{mem}) & \textbf{Eq 3.6} \end{cases}$$

where C_{mem} is the concentration on the cell membrane. k_a and k_d are the first order rate constants for adsorption and desorption of CNT on membranes.[25] ∇' is the Laplace operator for 2D diffusion and D_{mem} is the coefficient for the diffusion along the cell membrane. Since binding/unbinding processes are reversible and fast with characteristic times of milliseconds,[25] we can add another equation to this system

$$C_{mem}/C_{ex} = k_a/k_d = K \qquad \textbf{Eq 3.7}$$

where K is the equilibrium constant ($K > 0$) for CNT two-phases distribution between the interstitial space and membrane surface.

Note that ∇ and ∇' have different systems of coordinates that are 'natural' for 3D bulk and 2D surface diffusion processes. It is possible to transform ∇' into Cartesian coordinates but it will require additional boundary conditions and separate geometrical description of the membrane surface. Note also that D_{mem} is logarithmically dependent on the membrane curvature and the size of the permeant.[13] Even after some simplification including **Eq. 3.7**, this system of differential equations is difficult for analytical solution. It can be solved by numerically of using Monte Carlo (MC) simulations.

Similar problem originated in the past for diffusion for small molecules in porous solids.[17] Based on MC simulations of the diffusion pathways for combined 2D (surface-confined) and 3D (bulk) diffusion, an apparent diffusion coefficient

can be calculated as **Eq.3.1** based the assumption of association-dissociation equilibrium ($C_{bi}/C_{ex} = K$)[15].

$$J = J_{ex} + J_{mem} = -\left[D_{e,ex} + a_v D_{e,mem}\frac{C_{bi}}{C_{ex}}\right]\frac{d\,C_{ex}}{dr'} \qquad \textbf{Eq. 3.8}$$

where J_i is the interstitial phase diffusive flux, J_{mem} is the cell membrane surface diffusive flux, $D_{e,i}$ is the effective interstitial phase diffusivity, $D_{e,mem}$ is the effective cell membrane surface diffusivity (length^2/time); C_{ex} is the extracellular concentration, C_{bi} is the cell membrane surface concentration. a_v is volume ratio(cylinder layer-cell membrane to capillary-interstitial layer). r' is the direction of net motion.

For combined interstitial and cell membrane surface diffusion, an effective diffusivity can be described in terms of the diffusivities associated with an equivalent capillary and of tortuosity factors τ for the void and surface phases as **Eq. 3.1**. The parameters in the equation can be estimated using experimental results for hepatocytes, cellular spheroids, and tumors as following:

$a_v = 2\pi$ (interstitial space size) (cell membrane thickness)$\times L/\pi$(interstitial space size)$^2\times L$

=2(cell membrane thickness)/(interstitial space diameter) = 2× 8nm/1343nm = 0.012 [26,27]

D_{ex} = (1.45±0.65) $\times 10^{-14}$ m^2/s in lymph [9]

$\boldsymbol{D_{mem}}$ = (2.3±0.7) ×10^{-12} m^2/s [13]

$\boldsymbol{D_a}$ were shown in **Table 1** of maintext

$\boldsymbol{\phi}$ = 40%~80% (average: 60%) [28]

$\boldsymbol{\tau_{ex} = \tau_{mem} = \frac{L}{C} = \frac{2d}{\pi d} = \frac{2}{\pi}}$ = 0.6 (assume heptocytes are spherical, $\boldsymbol{d}$ is the average radius)

$\boldsymbol{\tau_{ex}}$ = $\boldsymbol{\tau_{mem}}$ = 0.6, $\boldsymbol{\phi}$ = 60%, and $\boldsymbol{a_v}$ = 0.012.

$\boldsymbol{D_{mem}}$ can be treated as a surface-averaged constant and was calculated for diffusion for membrane proteins to be (2.3±0.7) ×10^{-12}(m^2/s).[13] Since lymph is essentially interstitial fluid, we should use diffusion coefficient of CNTs in lymph as $\boldsymbol{D_{ex}}$, i.e. (1.45±0.65)×10^{-14} m^2/s.[9] $\boldsymbol{D_a}$ from ***Eq 3.3*** for CNTs-FITC and CNTs-TGFβ1-FITC is equal to (0.9±0.3)×10^{-14} m^2/s and (1.5±0.2) ×10^{-13} m^2/s**.** [4] Therefore, if consider the membrane diffusion as part of extracellular diffusion, we have

$$\boldsymbol{K = (D_a - \frac{D_{ex}\,\phi}{\tau_{ex}})/(\frac{D_{mem}}{\tau_{mem}}\,a_v)} \quad (\boldsymbol{K} > 0) \qquad \textbf{Eq 3.9}$$

Based on the parameters above, we can calculate the equilibrium constant $\boldsymbol{K}$:

a. CNT-FITC:

$$K_{CNT\text{-}FITC} = (0.9\pm0.3\times10^{-14}\ m^2/s - 60\% \times 1.45\pm0.65\times10^{-14}\ m^2/s\ /0.6)/ (2.3\pm0.7\times10^{-12}\ m^2/s\ /0.6 \times 0.012) \approx 0 \text{ (Range of 0~0.125)}$$

b. CNT-FITC-TGFβ1

$$K_{CNT\text{-}FITC\text{-}TGF\beta1} = (1.5\pm0.2\times10^{-13}\ m^2/s - 60\% \times 1.45\pm0.65\times10^{-14}\ m^2/s\ /0.6)/ (2.3\pm0.7\times10^{-12}\ m^2/s\ /0.6 \times 0.012) \approx 2.95 \text{ (Range of 1.81~5.06)}$$

Therefore, the equilibrium constants obtained from experimental data are $K_{CNT\text{-}FITC} = 0$ and $K_{CNT\text{-}FITC\beta1\text{-}FITC} = 2.95$ for CNTs-FITC and CNTs-TGFβ1-FITC, respectively. These values are in agreement with each other as one would expect that affinity of surface ligands to the cells surface increases with addition of TGFβ1. The presence of carboxyl groups on CNTs-TGFβ1-FITC is likely to play a role as well because the latter are less adhesive to cells than the targeting ligand itself. [29] Given the overall tendency for the CNTs-based permeants to adhere to cell membranes, the negative charges of CNTs-TGFβ1-FITC and CNTs-FITC (**Table 2.3)** are likely to stimulate the lateral 2D diffusion be reducing internalization in the tissue model from HepG2 cells, which allowed unbounded CNTs to diffuse further and faster.

Thus, anomalously high values of $\boldsymbol{D_a}$ of CNTs-TGFβ1-FITC should be attributed to the contribution of the lateral diffusion along the cellular surface to the overall transport.[7, 9] Some electrostatic repulsion between CNTs-TGFβ1-FITC and cellular membrane facilitate the lateral motion. The partial confinement to the surface due to the presence of targeting ligands dramatically accelerate the transport of the permeant despite the overall increase in mass and results in anomalously high diffusivities. Similar transition from 3D to 2D diffusion in tissues is also known for some proteins that roll across the cellular membrane. [19,30]

3.4.3 Simulation model

Simulations of CNT transport within dense tissue model require (**i**) appropriate methods to represent realistic model, cellular spheroid, and (**ii**) efficient algorithms to monitor nanotube trajectories within the interstitial void space and/or on the cell membrane surfaces that constrain these voids. Here, we describe these realistic, simulated structures and algorithm that we used for Monte Carlo simulation for diffusion; while we concurrently provide a rigorous comparison of the transport properties of CNTs in dense tissue.

Given the equilibrium condition in the tissue environment, CNT transport is subject to **Eq.3.1**, where $\boldsymbol{D_i}$ and $\boldsymbol{D_{mem}}$ are the inherent properties of nanotubes and homogeneous media in each phase according to practical experiments. Correspondingly, the variables $\boldsymbol{K}$, $\boldsymbol{a_v}$ and $\boldsymbol{\phi}$ in the simulated tissue model are the uncertain factors from real cellular spheroids and difficult to measure in the

experimental setting. $\boldsymbol{K}$ is dependent on the affinity between CNTs and HepG2 cells, meanwhile, $\boldsymbol{a_v}$ and $\boldsymbol{\phi}$ are determined by the nature structure of cells and cellular spheroids such as thickness of cell membrane and diameter of interstitial space. Here we investigate how the change of these parameters affect the transport of nanotubes in dense tissue.

First of all, in anomalous diffusion of CNTs incorporated with cell membrane surface displacement, equilibrium constant $\boldsymbol{K}$ is the key factor to affect CNT transport in dense tissue. To demonstrate the method of data analysis and to provide a reference system, we first consider spherical obstructs, of which the surface has no binding ($\boldsymbol{K}$=0) with CNT (**Figure 3.9**). Simulated apparent diffusion coefficient of this condition, (1.48±0.002) $\times 10^{-2}$ $\mu m^2/s$, agrees with the value of interstitial diffusion rate, $\boldsymbol{D_i}$, as in free Brownian diffusion. In the simulation, travel distance (μm) associated time (min) (**Figure 3.9a**) and average value of apparent diffusion coefficient $\boldsymbol{D_a}$ (**Figure 3.9b**) were simulated from 1,000 CNTs. Within the range of experimental $\boldsymbol{K}$ value within 1-10 in previous report[4], the diffusion rate has significantly increased from (7.6±0.3) $\times 10^{-2}$ $\mu m^2/s$ to (12.9±0.5) $\times 10^{-2}$ $\mu m^2/s$ but not yet achieved the maximum. When $\boldsymbol{K}$ increased up to 1000, apparent diffusion coefficients in cellular spheroid is converging to (13.6±0.4) $\times 10^{-2}$ $\mu m/s^2$. The value had been inherently assumed to be the membrane diffusion coefficient. However, this convergence is ten folds smaller than membrane diffusion coefficient $\boldsymbol{D_{mem}}$. The observed difference between simulated $\boldsymbol{D_a}$ with large value of $\boldsymbol{K}$ and $\boldsymbol{D_{mem}}$ could be a consequence of inadequate steps of interstitial diffusion, which

result in no further movement of nanotubes with initial steps in interstitial space. This phenomenon indicated that balance between interstitial diffusion and cell membrane surface sliding against the curvature is essential for two-phase transport of CNTs. Moreover, the resulting apparent diffusion coefficients $(1.1\pm0.03) \times 10^{-1}$ $\mu m^2/s$ at $\boldsymbol{K}$ = 2.95 from simulation show slightly lower than experimental data $(1.5\pm0.2) \times 10^{-1}$ $\mu m^2/s$. It could be due to the discrepancy of structures between the theoretical model and the realistic tumor spheroid, especially, the void fraction and volume ratio. To prove this hypothesis, alternative structures are simulated as below.

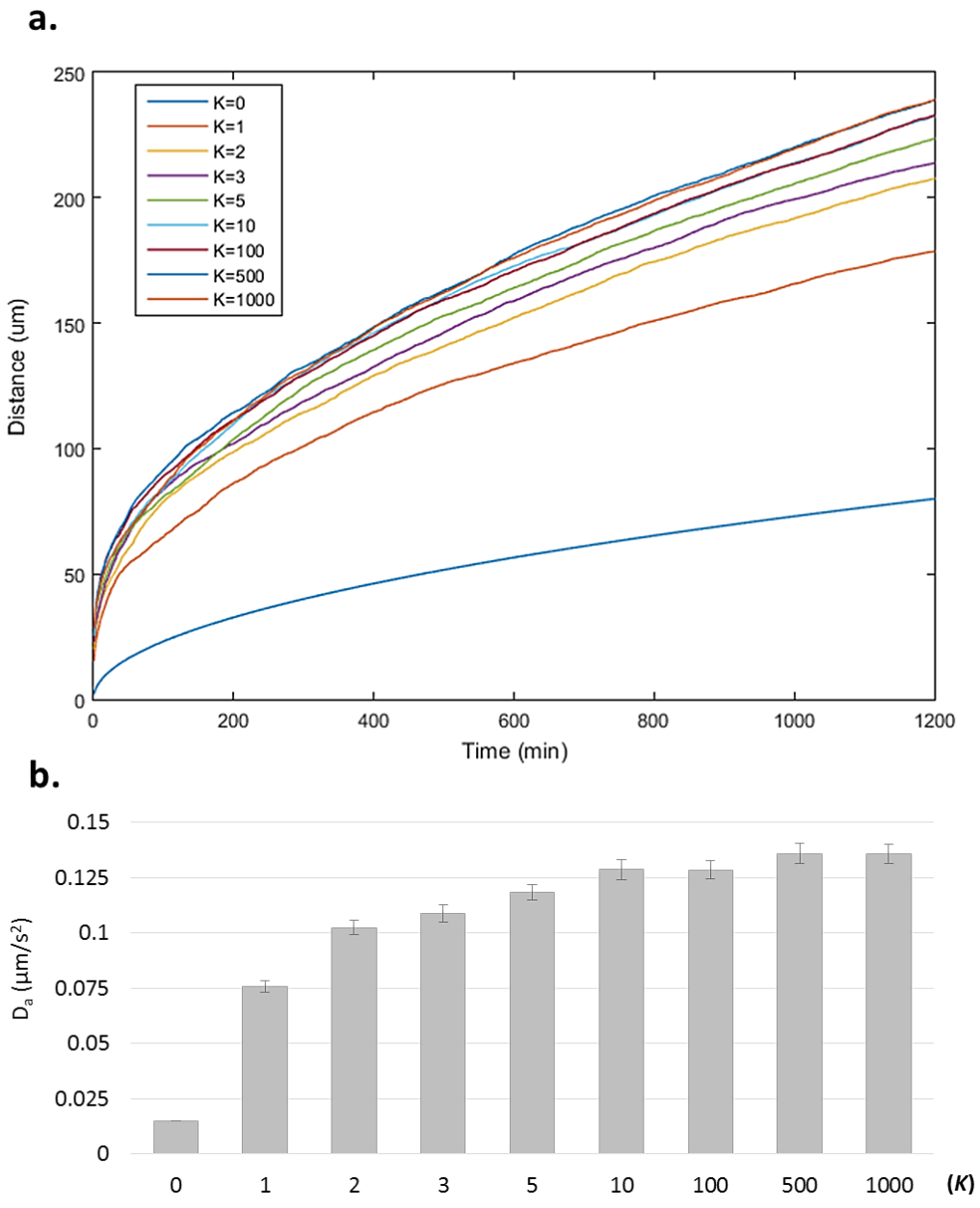

Figure 3.9 Chart of Simulated results with ***K*** =1-1000**.** Trajectories of CNTs associated time **(a)** and average value of apparent diffusion coefficient D_a **(b)** were simulated from 1,000 CNTs.

Now let us consider if the void fraction change can affect the simulation results. In the simulated model, we originally applied the value of average intercellular distance of 1.34 μm[26]. The void fraction $\boldsymbol{\phi}$ is determined to be 56.4%. In addition, the simulated structures are also built with interstitial diameters of 0μm, 1.93μm, 4.20μm and 7.78μm. The resulting structures accurately capture the morphology of the void space formed as 47.6%, 50%, 60%, 70% and 80% (**Figure 3.10a-c**).[31] The range of these fractions is reasonable within the surgical and radiological observation. The corresponding apparent diffusion coefficients were computed at the experimental equilibrium condition $\boldsymbol{K}$=2.95 (**Figure 3.10d**).

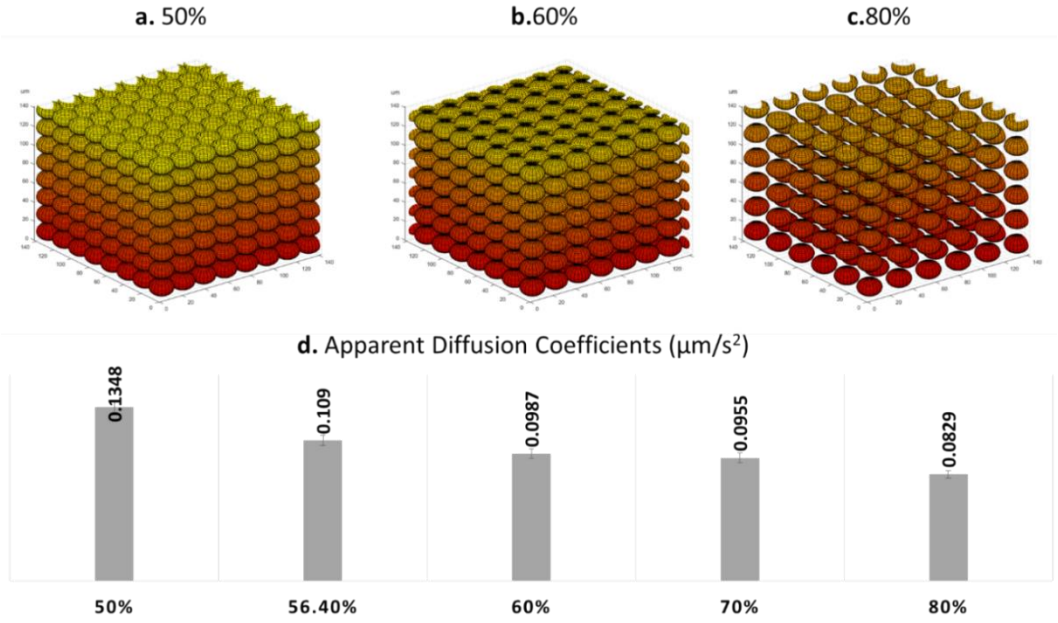

Figure 3.10 Fraction Volume (%) which is corresponding to interstitial space of 0.3, 1.3, 1.9, 4.2, 7.8nm. The apparent diffusion coefficient decreased with void fraction increased.

The values of simulated $\boldsymbol{D_a}$ increases with the $\boldsymbol{\phi}$ decreases, and $\boldsymbol{D_a}$ = (1.3±0.04) $\times 10^{-1}$ $\mu m^2/s$ with $\boldsymbol{\phi}$ = 50% is approximate to the experimental value in cultured cellular spheroid. In another word, the experimental models, in fact, have lower void volume than real tumor tissue because they do not inculde blood vessle and lymth system. Therefore, the experimental value was higher than estimated, which was calculated according to both void fraction $\boldsymbol{\phi}$ and volume ratio $\boldsymbol{a_v}$ from reference images of tumor *in vivo*, average interstitial space size and cell membrane thickness. Overall, this trend establishes the fact that the structure of tissue/tissue model is essential for CNT transport, and the result also shows that the actual void fraction in practical cellular spheroids was lower than the estimated value *in vivo*. Although the construction of cells in tumor tissue and transport of nano-sized particles can be much more complex than the models in the ICC scaffold *in vitro,* these simulations provide a conceptual benchmark and prediction to compare against actual conditions and values.

3.5 Conclusion

The simulation results of CNT transport in cellular spheroids presented here make contact with previous work and to serve as a reference system. In the two-phase diffusion model, apparent diffusion coefficient is depending on the void fraction of tissue structure and equilibrium constant ***K***. We conclude that under the equilibrium state, the implications of higher affinity of nano-sized agent with cell membrane is essential and beneficial for its transport in dense tissue such as solid tumor. And the diffusion coefficient is, at the same time, associated with the void fraction (volume), of which the factor varies among individual patients or different types of cancer/diseases. In the future study, binding and lateral diffusion on lipid membrane of CNT or other nano-sized agents in dense tissue should be considered in pharmaceutical application.

3.6 Notation

a_v surface-to-volume ratio

C_i interstitial space concentration

C_m membrane surface concentration

D_a equivalent diffusivity for calculation of void tortuosity

D_i interstitial space diffusivity

D_{mem} membrane surface diffusivity

K equilibrium constant

MSD mean-square tracer displacement

τ_i void tortuosity

τ_{mem} surface tortuosity

3.7 References

(1) Ferrari, M. Cancer Nanotechnology: Opportunities and Challenges. *Nat. Rev. Cancer* **2005**, *5*, 161–171.

(2) Liu, Z.; Chen, K.; Davis, C.; Sherlock, S.; Cao, Q.; Chen, X.; Dai, H. Drug Delivery with Carbon Nanotubes for In Vivo Cancer Treatment. *Cancer Res.* **2008**, *68*, 6652–6660.

(3) Ulissi, Z. W.; Sen, F.; Gong, X.; Sen, S.; Iverson, N.; Boghossian, A. a.; Godoy, L. C.; Wogan, G. N.; Mukhopadhyay, D.; Strano, M. S. Spatiotemporal Intracellular Nitric Oxide Signaling Captured Using Internalized, near-Infrared Fluorescent Carbon Nanotube Nanosensors. *Nano Lett.* **2014**, *14*, 4887–4894.

(4) Wang, Y.; Bahng, J. H.; Che, Q.; Han, J.; Kotov, N. a. Anomalously Fast Diffusion of Targeted Carbon Nanotubes in Cellular Spheroids. *ACS Nano* **2015**, *9*, 8231–8238.

(5) Junttila, M. R.; de Sauvage, F. J. Influence of Tumour Micro-Environment Heterogeneity on Therapeutic Response. *Nature* **2013**, *501*, 346–354.

(6) Nel, A. E.; Mädler, L.; Velegol, D.; Xia, T.; Hoek, E. M. V; Somasundaran, P.; Klaessig, F.; Castranova, V.; Thompson, M. Understanding Biophysicochemical Interactions at the Nano-Bio Interface. *Nat. Mater.* **2009**, *8*, 543–557.

(7) Kujawa, P.; Winnik, F. M. Innovation in Nanomedicine through Materials Nanoarchitectonics. *Langmuir* **2013**, *29*, 7354–7361.

(8) Dawidczyk, C. M.; Russell, L. M.; Searson, P. C. Nanomedicines for Cancer Therapy: State-of-the-Art and Limitations to Pre-Clinical Studies That Hinder Future Developments. *Front. Chem.* **2014**, *2*, 1–13.

(9) John William Judkins. Carbon Nanotube Diffusion under Simulated Physiological Conditions. *Cornell Hotel Restaur. Adm. Q.* **2010**, *22*, 64–64.

(10) Saxton, M. J. Anomalous Diffusion due to Obstacles: A Monte Carlo Study. *Biophys. J.* **1994**, *66*, 394–401.

(11) Saxton, M. J. Anomalous Diffusion due to Binding: A Monte Carlo Study. *Biophys. J.* **1996**, *70*, 1250–1262.

(12) Lee, J.; Cuddihy, M. J.; Cater, G. M.; Kotov, N. a. Engineering Liver Tissue Spheroids with Inverted Colloidal Crystal Scaffolds. *Biomaterials* **2009**, *30*, 4687–4694.

(13) Domanov, Y. a; Aimon, S.; Toombes, G. E. S.; Renner, M.; Quemeneur, F.; Triller, A.; Turner, M. S.; Bassereau, P. Mobility in Geometrically Confined Membranes. *Proc. Natl. Acad. Sci. U. S. A.* **2011**, *108*, 12605–12610.

(14) Steiner, K.; Papadopoulou, A.; Yu, D. The Role of Interventional Radiology in the Treatment of Hepatocellular Carcinoma. *Semin. Ultrasound. CT. MR* **2013**, *34*, 89–101.

(15) Petersen, E. J.; Huang, Q.; Weber, W. J. Relevance of Octanol-Water Distribution Measurements to the Potential Ecological Uptake of Multi-Walled Carbon Nanotubes. *Environ. Toxicol. Chem.* **2010**, *29*, 1106–1112.

(16) Ju, B.; Fan, T. Experimental Study and Mathematical Model of Nanoparticle Transport in Porous Media. *Powder Technol.* **2009**, *192*, 195–202.

(17) Zalc, J. M.; Reyes, S. C.; Iglesia, E. Monte-Carlo Simulations of Surface and Gas Phase Diffusion in Complex Porous Structures. *Chem. Eng. Sci.* **2003**, *58*, 4605–4617.

(18) Li, C.; Krishnan, J.; Stebbing, J.; Xu, X. Y. Use of Mathematical Models to Understand Anticancer Drug Delivery and Its Effect on Solid Tumors. *Pharmacogenomics* **2011**, *12*, 1337–1348.

(19) Jin, H.; Heller, D. a; Strano, M. S. Single-Particle Tracking of Endocytosis

and Exocytosis of Single-Walled Carbon Nanotubes in NIH-3T3 Cells. *Nano Lett.* **2008**, *8*, 1577–1585.

(20) Verma, A.; Uzun, O.; Hu, Y.; Hu, Y.; Han, H.-S.; Watson, N.; Chen, S.; Irvine, D. J.; Stellacci, F. Surface-Structure-Regulated Cell-Membrane Penetration by Monolayer-Protected Nanoparticles. *Nat. Mater.* **2013**, *12*, 376–376.

(21) *Advances in Carbon Nanomaterials: Science and Applications*; CRC Press, 2012.

(22) Kostarelos, K.; Lacerda, L.; Pastorin, G.; Wu, W.; Wieckowski, S.; Luangsivilay, J.; Godefroy, S.; Pantarotto, D.; Briand, J.-P.; Muller, S.; *et al.* Cellular Uptake of Functionalized Carbon Nanotubes Is Independent of Functional Group and Cell Type. *Nat. Nanotechnol.* **2007**, *2*, 108–113.

(23) Lopez, C. F.; Nielsen, S. O.; Moore, P. B.; Klein, M. L. Understanding Nature's Design for a Nanosyringe. *Proc. Natl. Acad. Sci. U. S. A.* **2004**, *101*, 4431–4434.

(24) Wang, X.; Xia, T.; Ntim, S. A.; Ji, Z.; George, S.; Meng, H.; Zhang, H.; Castranova, V.; Mitra, S.; Nel, A. E. Quantitative Techniques for Assessing and Controlling the Dispersion and Biological Effects of Multiwalled Carbon Nanotubes in Mammalian Tissue Culture Cells. *ACS Nano* **2010**, *4*, 7241–7252.

(25) Liu, C.; Krishnan; Xu, X. Y. Towards an Integrated Systems-Based Modelling Framework for Drug Transport and Its Effect on Tumour Cells. *J. Biol. Eng.* **2014**, *8*, 3.

(26) Spring, K.; Hope, a. Size and Shape of the Lateral Intercellular Spaces in a Living Epithelium. *Science (80-.).* **1978**, *200*, 54–58.

(27) Nanomedicine, Volume I: Basic Capabilities: 9781570596803: Medicine & Health Science Books @ Amazon.com http://www.amazon.com/Nanomedicine-Volume-I-Basic-Capabilities/dp/1570596808 (accessed Oct 29, 2015).

(28) Liver Malignancies - Diagnostic and Interventional Radiology | C. Bartolozzi | Springer http://www.springer.com/us/book/9783642636790 (accessed Oct 29, 2015).

(29) Lee, J. H.; Jung, H. W.; Kang, I.-K.; Lee, H. B. Cell Behaviour on Polymer Surfaces with Different Functional Groups. *Biomaterials* **1994**, *15*, 705–711.

(30) Reuel, N. F.; Dupont, A.; Thouvenin, O.; Lamb, D. C.; Strano, M. S.; Reuel, B. N. F.; Dupont, A.; Thouvenin, O.; Lamb, D. C.; Strano, M. S. Three-Dimensional Tracking of Carbon Nanotubes within Living Cells. *ACS Nano* **2012**, *6*, 5420–5428.

(31) Alex M. Andrew. *Nanomedicine, Volume 1: Basic Capabilities*; Emerald Group Publishing Limited, 2000.

Chapter IV

3D Cell Culture for NP Transport Study in Personalized Model: Hepatic Differentiation of Controlled-Size EBs in ICC Scaffolds

4.1 Abstract

Human stem cells such as embryonic stem cells (ESCs) and induced pluripotent stem cell (iPSC) hold promising potential as a renewable cell source for tissue regeneration and personalized drug screening. The stem cells in 3D culture systems for various *ex-vivo* application is advancing exponentially. ESC-derived specific cell lineages were strongly influenced by the size of embryoid bodies (EBs). Several approaches have been developed to control the size of EBs and direct ESC

fate for cardiogenesis and neurogenesis. However, desirable size for directed differentiation of ES cells to hepatocyte-like cells are still unknown. In this chapter, a 3D stem cell culture in inverted colloidal crystal (ICC) scaffolds with highly uniform porous structure was introduced. The size-controlled EBs can potentially apply to NP transport evaluation as personalized model. The sizes of EBs were controlled by varying diameters of pores in scaffold (90 μm, 170 μm, 200 μm, 270 μm and 400 μm). Differentiation of ES cells into early hepatocytes was assessed by analyzing gene expression. We found that hepatic differentiation of ES cells were strongly regulated by the sizes of EBs and EBs equals to or larger than 180 μm in diameter maintained the ability to differentiate to specific lineage and EBs in diameter of 202 μm induced highest yield of hepatic differentiation where the optimal pore size of scaffolds is 270 μm.

4.2 Introduction

Human stem cells such as embryonic stem (ES) cells and induced pluripotent stem cell (iPSC) are able to provide potentially unlimited resources of tissue for *ex-vivo* models for regenerated medicine and personalized drug screening especially for transport of nanomedicine in patient-specific tissue because this process was strongly influenced by cellular interaction with drugs [1,2]. They can be

derived to a wide spectrum of cell types. For instance, ES cells can differentiate into neural cells, cardiomyocytes, hepatic and endothelial cells by forming embryoid bodies (EBs) and complement the variety of conventional animal models from human with more relevance and personalization. The size of EBs is a key factor in determining cell fate, and promoting differentiation toward cardiomyocytes[3], chondrocytes[4] or neural lineages[5]. A large amount of engineered microstructures have been used for study the effect on ES cell differentiating fate by regulating EBs size during development; and it has been further proved that the lineage specific differentiation from EBs for cardiac and neural fates are highly influenced by the size of EB. Recent study indicated cardiac differentiation of EBs in a wide range of sizes and geometries[6], 100 μm ~500 μm in lateral dimensions and 120 μm in depth. It was concluded that the 300 μm micro-wells produced highest percentage of contracting EBs, and the smaller EBs are less likely to form contracting EBs, however, those contracting EBs formed a similar percentage of cardiomyocytes compared to larger EB sizes. An optimal size of EBs for chondrogenic differentiation were investigated by dividing pre-differentiated EBs into three groups, <100 μm, 100 μm ~150 μm and >150 μm [4]; small EBs were more significantly to express the specialized chondrogentic markers. Cardiogenesis can be enhanced in larger EBs up to 450 μm in diameter, and in contrast, endothelial

cell differentiation was increased in smaller EBs in diameter of 150 μm [7]. Yet, among all genesis of organs and tissues, liver is a key organ for cell therapies and drug discoveries. Thus, an effective and convenient liver tissue model generated from stem cells are always on demand.[8–10,11] However, little is known regarding the size effect of EBs on generation of hepatocytes from ES cells.

Several methods for size control of EBs, such as hanging drop (HD)[12], multi-well plates[13], laser direct-write[14] and micro-patterned chips[15,16–21], have been developed. HD method allowed individual cells spontaneously self-assemble but not all the formed EBs are spherical due to the cell spreading on 2D flat substrates. Various tools by micro-patterned methods provided external forces or confined geometry to control the diameters and homogeneity of EB formation, however, the formed EBs have still limited relatively high variance in diameters. In addition, most of these patterned tools are not able to satisfy both the engineering and tissue culture factors such as size control, mechanical properties, porosity and nutrient transportation at the same time.[22–25] Moreover, cells must be pipetted manually into some of the devices, which is time-consuming and increases the likelihood of contamination during the process. Overall, these techniques have provided advances, but the goal of highly reproducible, efficient, scalable hepatic differentiation from EBs at the same time has not been obtained.

In this chapter, we utilized ICC scaffolds to form size-controlled EBs and to understand how size of EBs shall influence hepatic differentiation derived from ES cells. The ICC scaffolds have unique features with uniformly sized pores in the 3D matrixes, which can afford a high yield production of controlled size spheroids in wide range, at the same time, it can provide efficient nutrient transport and cell-cell interaction to enhance the quality and viability of cellular spheroids [22,26–28,29]. The selected pore sizes of scaffolds were 90μm, 170μm, 210μm, 280μm, 400μm and HD method was used as a control method. The degrees of hepatic differentiation from ES cells into in each diameter was examined as well as the functions of obtained hepatocyte-like cells. This stem cell culture in 3D size-controlled scaffolds also provides a promising tool for future study of NP transport in patient/disease-specific models.

4.3 Materials and Methods

4.3.1 Fabrication of ICC scaffolds in different sizes

Dried 1 g of soda lime glass beads with average diameters of 90μm, 170μm, 200μm, 270μm, 400μm (Thermo Fisher Scientific, MA) were dispersed in 5 ml of ethylene glycol. A glass shell vial (Fisher Scientific) connected with a long glass pipette was used as a mold for colloidal crystals (CCs) preparation. (**Figure 4.1a-**

e) The complex unit was inserted in a glass tube (O.D. ¼10 mm, H ¼75 mm) that was halfway immersed in an ultra-sonic water bath (VWR), and the inner space of mold was filled with ethylene glycol. 20μl of glass bead suspension was released to the mold per 20 min until the thickness reached approximately 1 mm. After complete evaporation of ethylene glycol at 160 °C, the CCs were annealed for 4 h at 670–690 °C, depending on the size of beads, and then free standing CCs were extracted from the mold.

Poly(acrylamide) hydrogel precursor solution (30% (w/w) acrylamide, 5% (w/w) bis-acrylamide, and 0.1% (v/v) N,N,N,N-tetramethylethylenediamine), prepared as described previously, was infiltrated into the CC by centrifugation and polymerized by addition of radical initiator (1% (w/w) potassium peroxideThe infiltrated CC was cut out from the hydrogel and immersed in 5% (v/v) hydrogen fluoride (HF) solution for 24 h to dissolve the glass beads. Later, ICC scaffolds were sequentially washed with pH 3.0 hydrochloric acid (HCl) solution, pH 7.2 phosphate buffered saline (PBS) solution, and deionized water for 2 days in each solution with 3–4 times solution changing per day. ICC scaffolds were further freeze dried to completely remove remaining HF and reserved in dried state until used. The final dimensions of hydrated scaffolds were 6.4 mm in diameter and 1 mm thickness.[29]

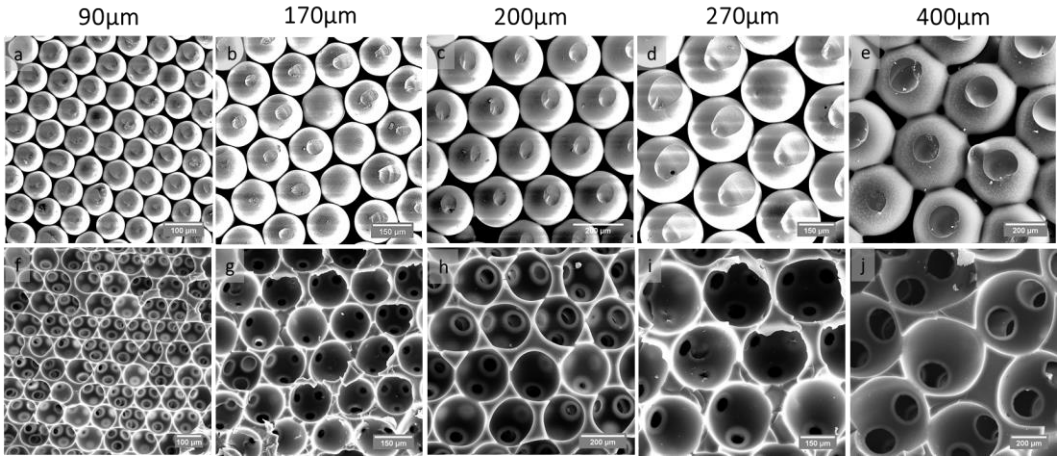

Figure 4.1 ICC scaffold fabrication. SEM images of highly ordered colloidal crystals with different sized glass beads of 90 µm, 170 µm, 200 µm, 270 µm and 400µm (**a-e**). Hydrogel precursor solution is later infiltrated into the colloidal crystals and polymerized. ICC scaffold geometry is created by dissolving beads from hydrogel matrix. The small spots on glass beads in (**a-e**) are contact points between beads, which later become channels in (**f-j**). Pore dimensions were reduced during the dehydration process for SEM sample preparation.

4.3.2 ES Cell Culture

129/Ola mouse embryonic stem (ES) cell line (ATCC, USA) was maintained at undifferentiated state in T-75 flasks (Fisher Scientific) on mitotically inactivated mouse embryonic fibroblast cells in Dulbecco's modified eagle medium-high glucose (GIBCOBRL, USA) containing 15% fetal bovine serum (Hyclone, USA), 1× non-essential amino acids (Gibco BRL, USA), 2mM glutamine (GIBCO-BRL, USA), 1000U/ml mouse Leukemia inhibitory factor-

ESGRO® (LIF-ESGRO®), 100M 2-mercaptoethanol (Sigma, USA), 100U/ml penicillin and 100µg/ml streptomycin (Gibco-BRL). To form embryoid bodies (EB), 1,000,000 cells in a 25µl of dense cell suspension ($4x10^6$ cells/ml) was dropped on top of completely dehydrated hydrogel ICC scaffold using a micro-pipette, and 975µl of media was gently added. Total culture volume was maintained at 1000µl, and half of media was changed every two days. As a control, ES cells were seeded by HP method (2000 cells per 25ul in each drop). All the medium was filtered using 0.22 µ SteriCup filter assembly (Millipore, USA) and stored at 4 °C for no longer than 2 weeks.

4.3.3 Differentiation of ES cells to hepatocyte-like cells *in vitro*

After 6 days of EB differentiation, cells in two culture systems were induced to differentiate towards hepatic direction by adding specific growth media. The composition of the optimized hepatocyte differentiation medium contained, DMEM (high glucose), 10% FBS, L-glutamine (1mM), non-essential amino acids (1%), L-mercaptoethanol (0.1mM), hepatocyte growth factor (HGF) 20µg/ml, aFGF (50µg/ml), Oncostatin (10µg/ml), insulin–transferrin-selenious acid (ITS-

1X), dexamethasone (10^{-5}mM). [30–32] (**Figure 4.2**)

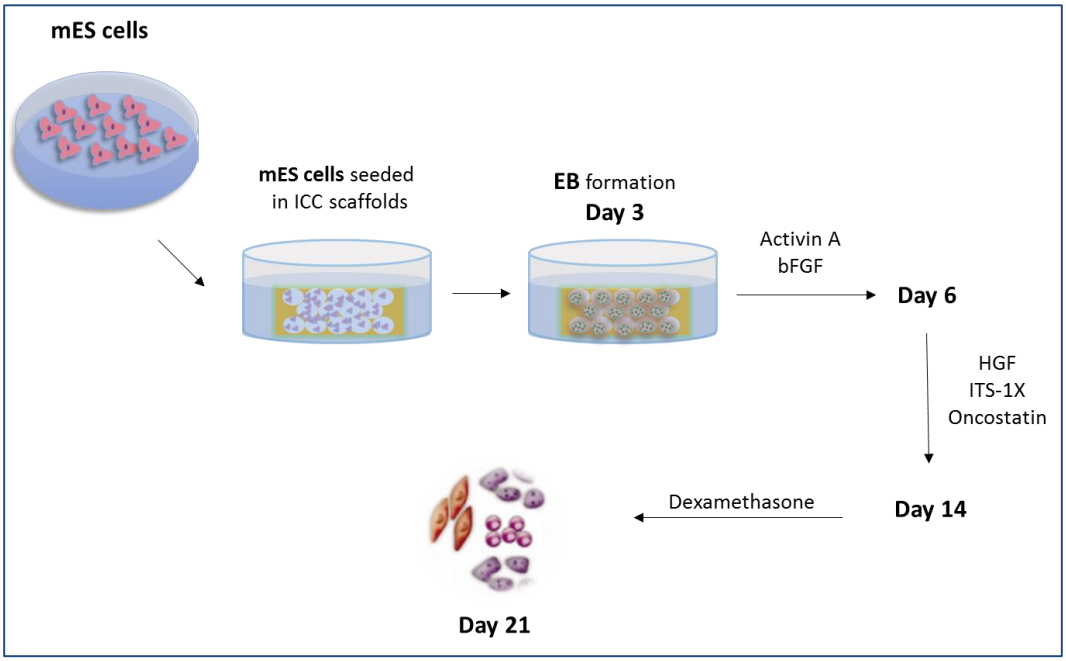

Figure 4.2 Hepatic Differentiation of EBs in ICC scaffolds.

4.3.4 Live/Dead Assay Analysis

Cell viability was observed using a Live/Dead Viability Kit (Invitrogen). 20µl of 2mM EthD-1 stock solution was added to 10mL of sterile, tissue culture–grade PBS solution (PH=7.4) and then to give an approximately 4µM EthD-1 solution. The reagents were combined by transferring 5µl of 4mM calcein AM stock solution to the 10mL EthD-1 solution. The resulting approximately 2µM calcein AM and

4μM EthD-1 working solution is then added directly to cell culture. The stained cells were visualized under fluorescence microscope (Zeiss Axiovert 100M inverted microscope) at 20×. Digital images were acquired with a charge-coupled device (CCD) camera and analyzed by an imaging system (LSM, Zeiss).

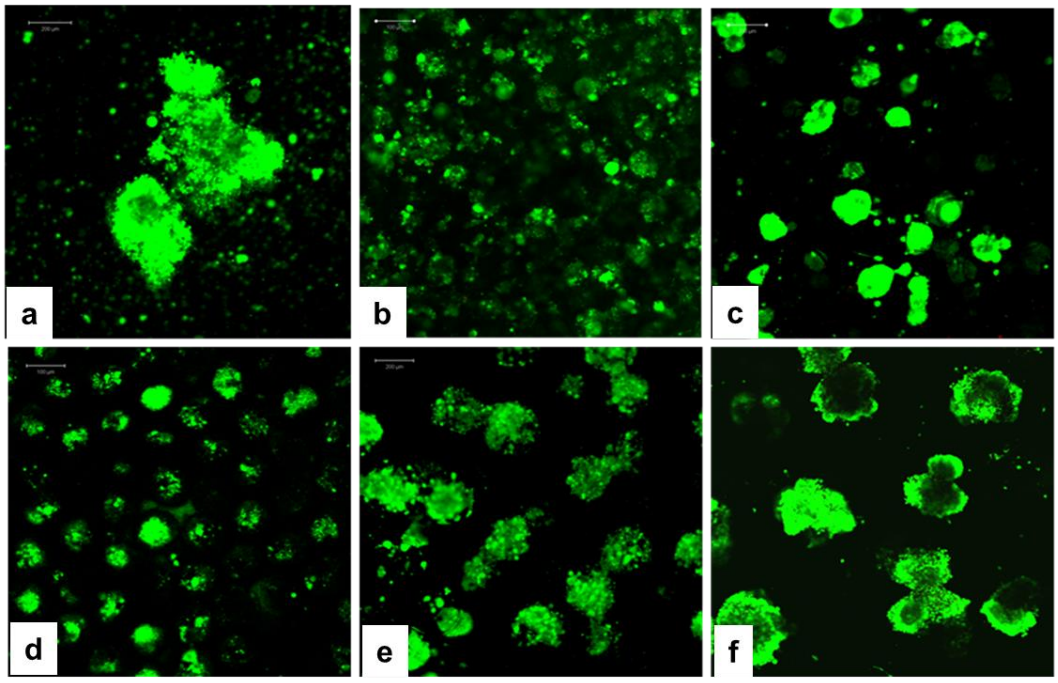

Figure 4.3 Confocal images (**a–f**) of live/dead stained EBs formed in ICC hydrogel scaffolds on Day 6. Green indicates live cells and red indicates dead cells. EBs obtained by hanging drop as a control (**a**). EBs induced by ICC scaffolds with diameters of 90 μm, 170 μm, 200 μm, 270 μm and 400μm (**b-f**). Most cells showed green color.

4.3.5 Detection of EBs formation and hepatic specific proteins by confocal microscope

Cultured ES cells grown in scaffolds, after 6 days and 20 days of differentiation were fixed with 4% freshly prepared paraformaldehyde for 20min at room temperature. For specific protein detection such as nuclear proteins, the cells were permeablized with 0.3% Triton X-100 (Sigma, USA) for 5min at room temperature and processed further. After aspirating the fixative, cells were washed three times for 5min each with PBS. Non-specific binding was blocked with PBS containing 1% rabbit serum in PBS for 2h at room temperature. The cells were then incubated with primary antibody (Oct-3/4, SSEA-1, GATA-4; Santa Cruz, USA, CK-18; Chemicon, USA; 1:100) in 10% rabbit serum overnight at 4 °C. Next, the cells were washed with 1× PBS three times for 5 min each. The cells were then incubated with secondary antibodies anti-rabbit-FITC for SSEA-1 and CK-18; anti-rabbit-TEXAS RED for Oct-3/4 and GATA-4 (Santa Cruz, USA; 1:500) in 0.1% rabbit serum at 37 °C for 30min. After giving three washes (5min each) with PBS, the cells were exposed to 1mg/ml DAPI solution for 1min. After washing the cells twice for 5min each with 1X PBS, they were ready for confocal imaging. Images were analyzied by *ImageJ* software (downloaded on http://rsbweb.nih.gov/ij/)

4.3.6 Detection of stored glycogen by periodic acid schiff (PAS) staining

The PAS technique was used to determine the presence of insoluble stored glycogen content in the cells. Briefly, hepatocyte-like cells after 20-day differentiating in scaffolds of different pore sizes were fixed with 4% paraformaldehyde at room temperature for 15min. It was then oxidized with 1% periodic acid for 5min, rinsed with distilled water for 5min and treated with Schiff's reagent for 10–15min. After rinsing in distilled water for 5min, scaffolds were counter stained with Mayer's hematoxylin stain for 30 s and observed under light microscope.

4.4 Results and Discussion

4.4.1 ES cells and EBs cultured in ICC scaffolds

Polyacrylamide hydrogel ICC scaffolds were prepared by utilizing colloidal crystals (CC) as templates (**Figure 4.1a-e**). To control the pore sizes of scaffolds, we use glass beads with five diameters: 90μm, 170μm, 200μm, 270μm and 400μm for this study. Regardless of the bead sizes, three-dimensional (3D) structure of CC

with high connection was achieved, which in turn was transferred into ICC geometry high porosity as previous method[27] (**Figure 4.1f-j**). To culture ES cells within porous 3D structures, the cells were seeded into scaffolds, allowing the cells to settle within the caves. One major feature of ICC scaffolds is that the resulting size and shape of EBs are similar to the 3D structure in which they are grown. In addition, EBs in scaffolds can contact with each other due to the highly porous connection, in contrast to previously reported concave micro-well or micro-patented chips.[6, 7, 15, 18, 19]

ES cells cultured within ICC scaffolds were physically constrained and formed EBs that were homogeneous in size. The viability of EBs was checked by standard live/dead cell viability assays which consisted of calcein AM and ethidium homodimer (EthD-1) addressing plasma membrane integrity and esterase activity, respectively (**Figure 4.3**). Stained with live/dead assay, live cells are green, while dead cells show red. The results demonstrated that cells cultured for 6 days remained viable regardless of the difference in diameters. The biocompatibility of ICC scaffolds allows further differentiation of culturing ES cells *in vitro*. EBs were harvested after culturing for 5 days within ICC scaffolds with pores in five diameters. The cells were stained as green (5-chloromethylfluorescein diacetate) for size analysis statistically. (**Figure 4.4 b-f**).

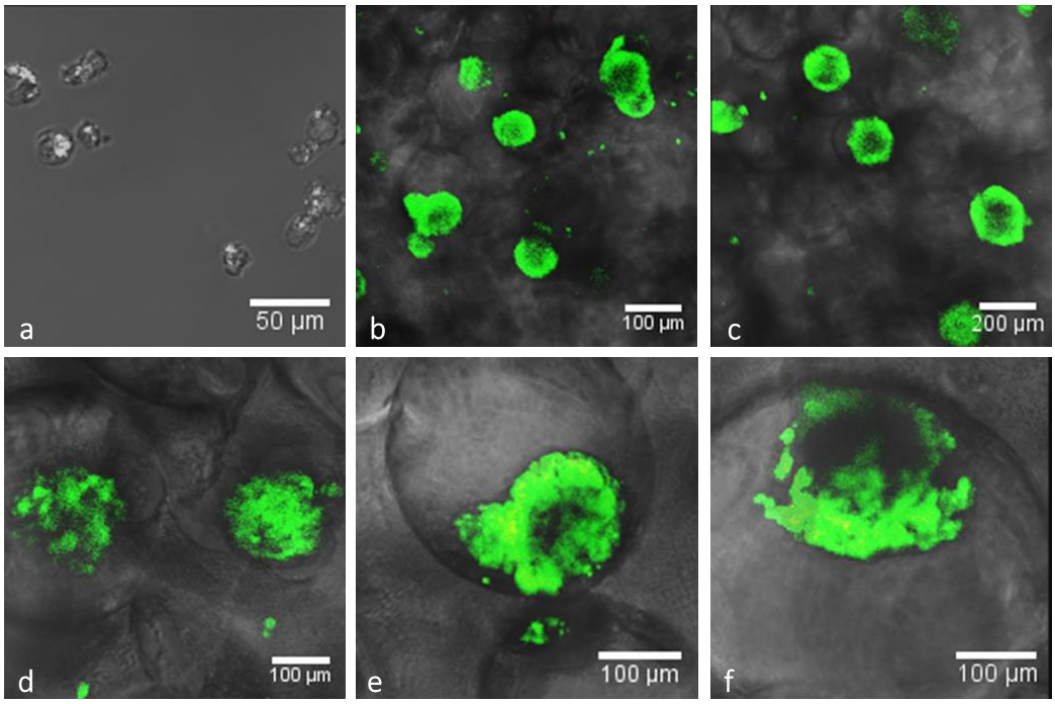

Figure 4.4 Confocal images with bright field of EBs formed in ICC hydrogel scaffolds on Day 3. ES cells are cultured on Petridish as control (**a**). EBs are grown in ICC scaffolds with pore diameters of 90µm, 170µm, 200µm, 270µm and 400µm (**b-f**). Cells were stained with CMFDA (5-chloromethylfluorescein diacetate) as green color.

4.4.2 Diameter distribution of size-controlled EBs in ICC scaffolds

To study how the pore sizes of ICC scaffolds control EBs formation in diameter with desirable precision, the scaffolds with five different diameters (90µm, 170µm, 200µm, 270µm and 400µm) were prepared, and seeded with the same initial number of ES cells. EBs were retrieved after culturing for 6 days from ICC scaffolds and the distribution of their diameters was analyzed. Spherical EBs

formed and exhibited relatively homogeneous sizes (**Figure 4.4b–f**) directly related to the initial pore sizes of ICC scaffolds in contrast to the more heterogeneous size distribution of EBs formed by HD method (**Figure 4.4a**). The dependence of spheroid diameter and uniformity of their size on the ICC pore size was quantified using image analysis. As a control, HD method was also used for formation of EBs. The distribution of EB sizes by HD and in ICC scaffolds were shown in **Figure 4.5** with a fine level of control ($P < 0.0005$) over the diameter.

The average sizes of EBs on day 6 of culture in scaffolds with different diameters and by HD method were 68 μm, 152 μm, 180 μm, 202 μm, 253 μm, 402 μm (**Figure 4.5a**), which were well fit to a Gaussian distribution. The size distribution of EBs was shown in **Figure 4.5b**. The porous structure with controllable size of ICC scaffolds constrained led ES cells forming predictable, uniform-sized EBs, particularly for the smaller sized pores, in contrast to more heterogeneous EB sizes resulting from unconstrained, conventional culture in larger sized pores of ICC scaffolds, and especially from HD method. When the size of pores becomes larger than 270 μm, other factors such as nutrient delivery to the interior cells of EBs would be a more critical issue than physical restriction, and thus the sizes of EBs become less dependent on the pore size of ICC scaffolds.

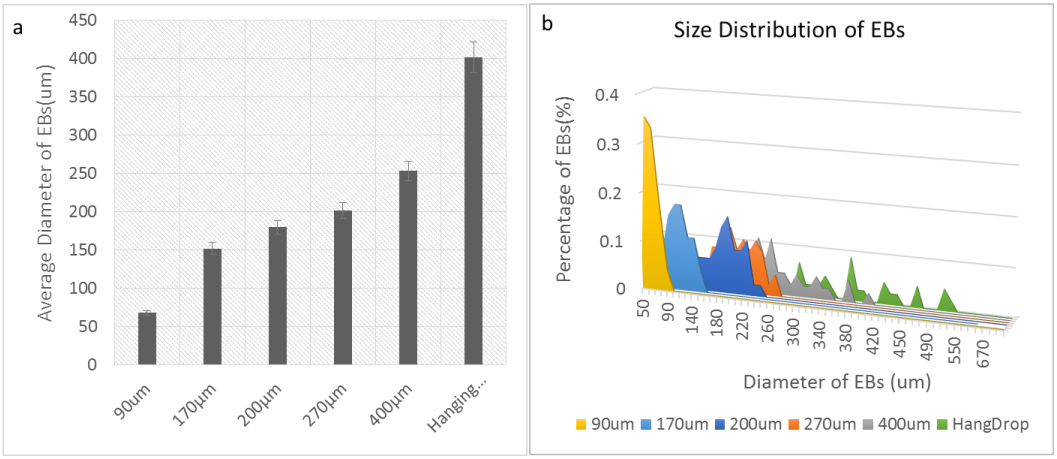

Figure 4.5 EBs size control corresponding to pore dimensions of ICC. ES cells were seeded in each ICC scaffolds having 90, 170, 200, 270 and 400 µm pore dimensions to get the average diameters of EB size after 6 days culturing. **(a)** Each group has significantly different sizes of EBs. Five scaffolds were used in each group and 50 EB sizes were measured. **(b)** Diameters distribution of Day 6 EBs.

4.3.3 Effect of EB size on hepatic differentiation

Once predictable EBs size distributions had been obtained from size-controlled ICC scaffolds after 6 days, ES cells were differentiated into hepatic fate for another two weeks following the existing protocol and the differentiation media was made referred to previous publications[3,29,30]. The effect of EB sizes on hepatic differentiation were examined.

First stage of differentiation. Differentiation of EBs in ICC scaffolds at the first stage was checked on day 3 (**Figure 4.6**) and day 6 (**Figure 4.7**) by immunocytochemical staining against pluripotency markers, Oct-3/4 and SSEA-1. Oct-3/4 is a master regulator of pluripotency and has been shown to be critical for maintaining ES cell character,[30-32] and it also governs three distinct fates of ES cells for the initial formation of a pluripotent founder cell population in the mammalian embryo. A less than two-fold increase in expression causes differentiation into primitive endoderm and mesoderm, which includes the early stage of hepatic fate.[33] SSEA-1 is a marker expressed on murine embryonal carcinoma cells, ES cells, and primordial germ cells. Murine SSEA-1 expression decreases with progress of differentiation in the early stage.[31, 34, 35] In the EBs immune-labeled on day 3 and day 6 of culture, **Figure 4.6** and **Figure 4.7** compared representative those EBs from 90 μm to 400 μm. From the image of EBs, similar ratios of SSEA-1 expression on individual cell surface in EBs were detected in ICC scaffolds with all the pore sizes except 90μm, which was in agreement with the expression of Oct-3/4. Smallest EBs have limited expression of SSEA-1 and OCT3/4, which means ES cells in ICC scaffolds within smallest pore size could not maintain their pluripotency.

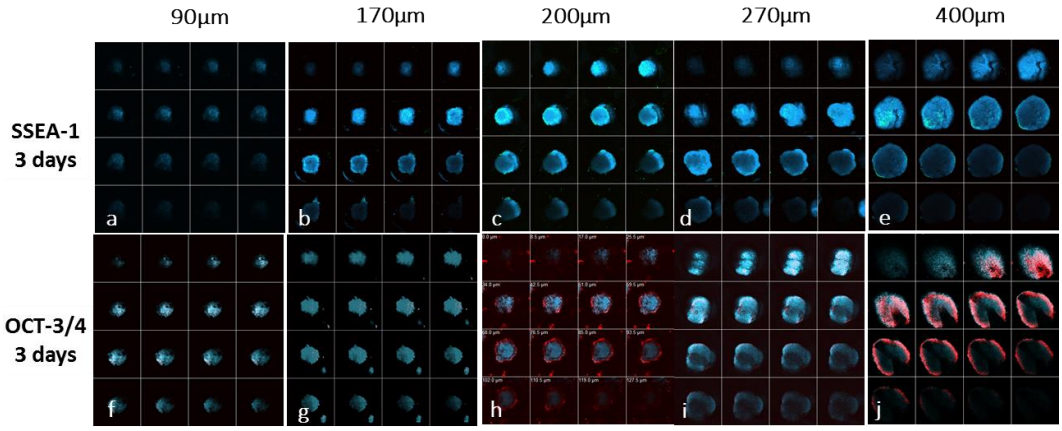

Figure 4.6 Confocal microscopy images differentiated EBs on day 3. EBs were stained for markers of differentiation at first stage. SSEA-1 (**a-e**) is shown in green, and OCT-3/4 (**f-j**) is shown in red, while the cell nuclei, counterstained with DAPI, are in blue. Each image is z-stack from top to bottom of an EB in scaffolds with different pore size.

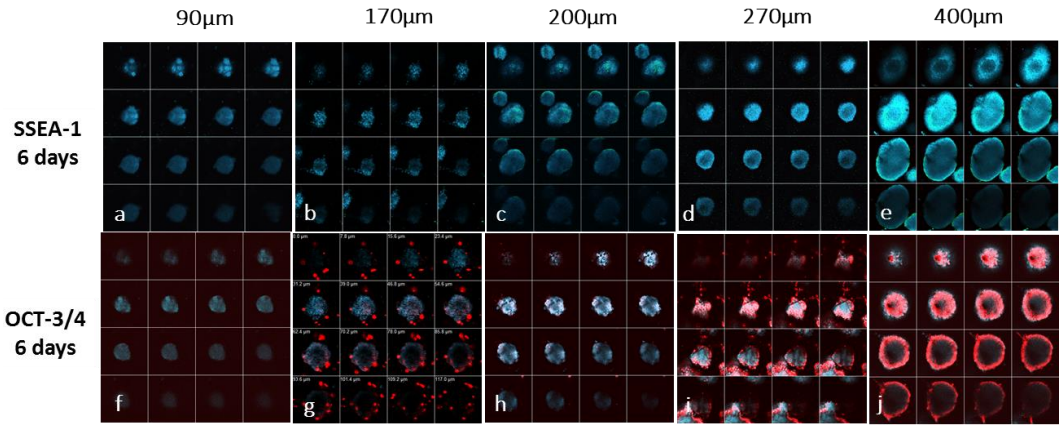

Figure 4.7 Confocal microscopy images differentiated EBs on day 6. EBs were stained for the same markers of differentiation as day 3.

Quantitative study of the change for gene expressions from day 3 to day 6 were shown in **Figure 4.8**. SSEA-1 decreased more significantly in the groups with larger size of 270 μm and 400 μm while no obvious change was observed in other groups. This agreed with the previous results that larger EBs tend to differentiate into primitive germ layers.[18]

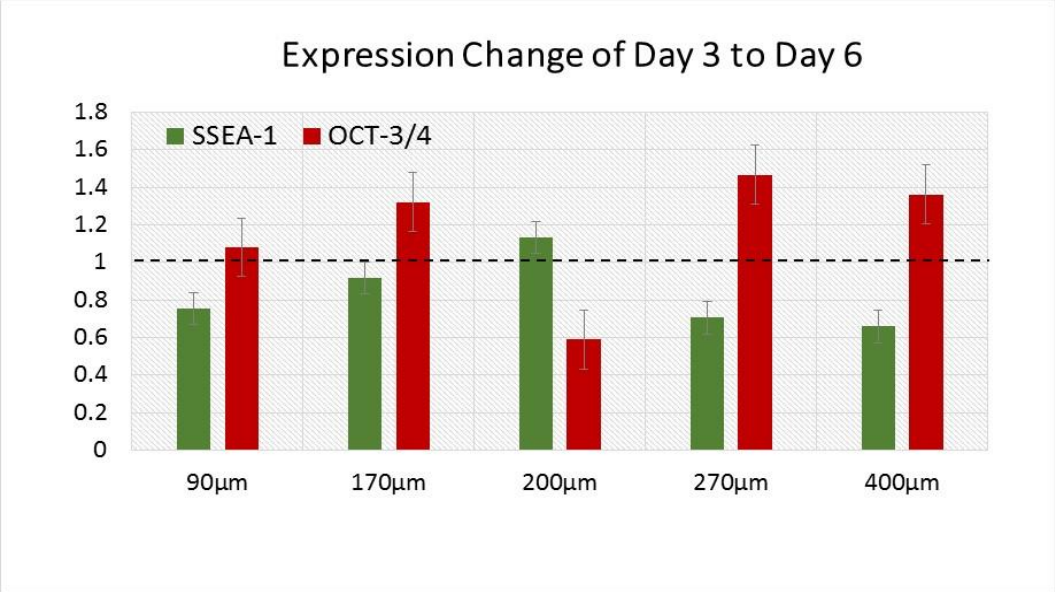

Figure 4.8 First stage of differentiation. Endoderm and Mesoderm development were indicated by OCT3/4 level change. Decrease of SSEA-1 expression indicated the progress of differentiation process.

In another aspect, Oct-3/4 expression of most groups increased slightly with the sizes of EBs except the one with a diameter of 200 μm. The peak of increase appear at the group of 270 μm which approached 1.5 fold, the level towards endoderm and

mesoderm differentiation;[33,34] while the expression of OCT-3/4 in other groups was within 0.5~1.5 fold, which indicated the ES cells still maintained pluripotency no matter the expression increase or decrease. Overall, according to the evaluation of early differentiation, larger EBs have better functionality for further induction of specific lineage and the size of 270 μm shows the highest the potential for hepatic fate developed from endoderm.

Analysis of hepatic differentiation by immunofluorescence. After culturing for 6 days in regular medium, EBs within ICC scaffolds were transferred to a new 48-well plate and cultured in hepatic differentiation medium for additional 14 days, resulting in hepatic differentiation. Hepatic differentiation of EBs cultured in ICC scaffolds with different pore sizes was analyzed by evaluating the expression of gene markers. The EBs were fixed and immune-stained with GATA-4, CK-18, and counterstained with DAPI. GATA-4, an early transcription factor, which indicates onset of hepatic maturation, was highly expressed in the differentiating cell population.[35–37] Meanwhile CK-18 is a mature hepatocyte marker[38,39]. The percentage of differentiated EBs into hepatocyte-like cells was high (**Figure 4.9 b-e, g-j**). However, the smallest EBs (**Figure 4.9 a, f**) demonstrates no differentiating toward hepatocyte-like cells.

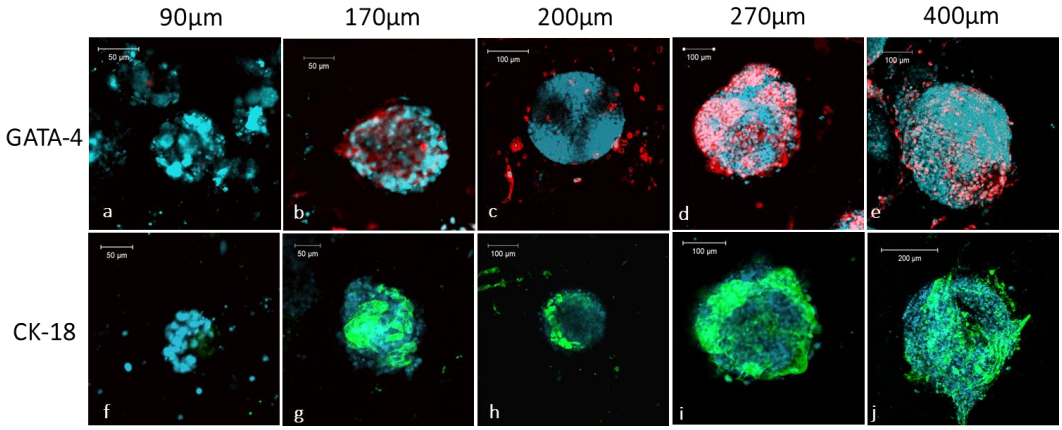

Figure 4.9 Confocal microscopy images differentiated EBs in ICC scaffolds with diameters of 90µm, 170µm, 200µm, 270µm and 400µm on day 21. EBs were stained for markers of hepatic differentiation. GATA-4 (**a-e**) is shown in red, and CK-18 (**f-j)** is shown in green, while the cell nuclei, counterstained with DAPI, are shown in blue. Images represent scans near the center of the EBs.

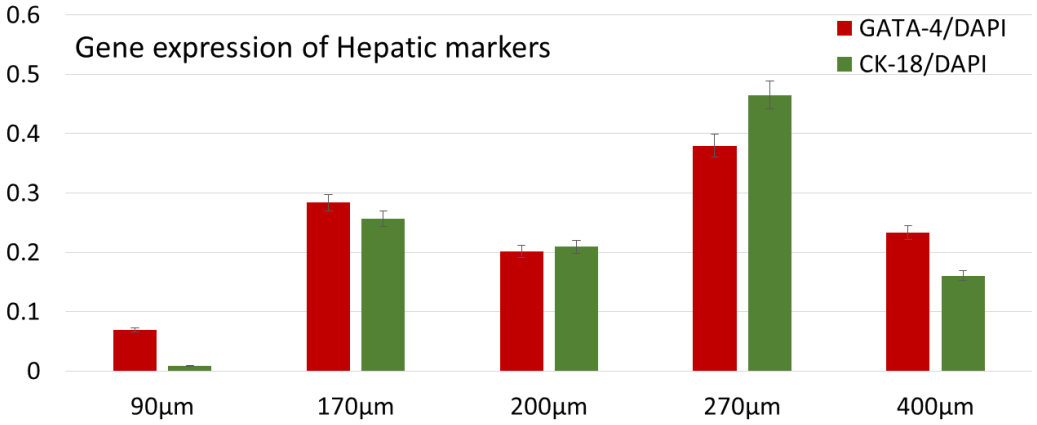

Figure 4.10 Quantitative gene expressions were processed from images.

Here we found the cells in scaffolds with the pore sizes more than 90 μm expressed proteins of resultant GATA-4 and CK-18, which is indicative of hepatocyte-like cells to a certain extent. Accordingly, the gene expression in differentiated cells was significantly reduced when the diameter of pore size was 90 μm, although they have showed decrease of SSEA-1 at the first stage of differentiation, which indicated ES cells could not form functional EBs within the hole in a small diameter and differentiated into specific lineages. GATA-4 and CK-18 are apparently observed in scaffolds with pores of 270 μm, while the expressions are lower in the pore of 170 μm, 200 μm and 400 μm. Processed imaging data **Figure 4.10**, which shows the area fraction of marker-positive cells to DAPI-positive cells, verified the fact that in the scaffolds with pore size of 270 μm, cells showed highest expression for both markers of hepatic differentiation as 38±2% of GATA-4 and 46±3% of CK-18. In contrast, in the scaffold with the pore size of 90 μm, no mature hepatocyte markers CK-18 was detected. The highest production of hepatocyte-like cells in scaffolds with pores of 270 μm was in agreement with the endoderm development in the early stage of differentiation. The yield of hepatocyte-like cells derived from EBs are highly affected by not only the directed differentiation stage but also the early development of three germ layers. From the results above, the optimal size of EBs for hepatic differentiation should be about

201.7±29.6 μm cultured in the scaffolds with pore size of 270 μm among all the groups.

Functionality test by PAS. To provide additional assessment of hepatic differentiation from EBs derived from ICC scaffolds with pores in five different diameters, PAS staining were used to detect the glycogen level that the hepatic-like cells stored. PAS is one of the metallic functions of hepatocytes.[40,41] To observe cells in an entire EB, we sectioned the EBs together with ICC scaffolds into histology slices with thickness of 1μm/slice after 21 day culturing. Middle plane of the sectioned slices were examined under optical microscope for each group.

PAS staining revealed cytoplasmic deposits of glycogen stained with purple-magenta color in hepatocyte-like cells. The stained cross-sections of ICC scaffolds are shown in **Figure 4.11**, where stained hepatocytes (HepG2, ATCC) were used as a control which did show positive staining (**Figure 4.110a**). From the result of PAS staining, we found limited glycogen stored in 90 μm EBs (**Figure 4.11b**) while larger size EBs shows the functionality of glycogen storage (**Figure 4.11c-f**). In the control group of hepatocytes exhibited the ratio of PAS staining-positive cells (98%±2%) to overall number of cells, the cytoplasmic glycogen secreted by the hepatic-like cells can be easily observed in larger EBs. Noticeably,

the stain was distributed uniformly throughout the EBs in group of scaffolds with pore size which is more than 200 µm, while the glycogen was detected only a thin layer close to the surface of EBs in diameter of 152.0±21.5 µm.

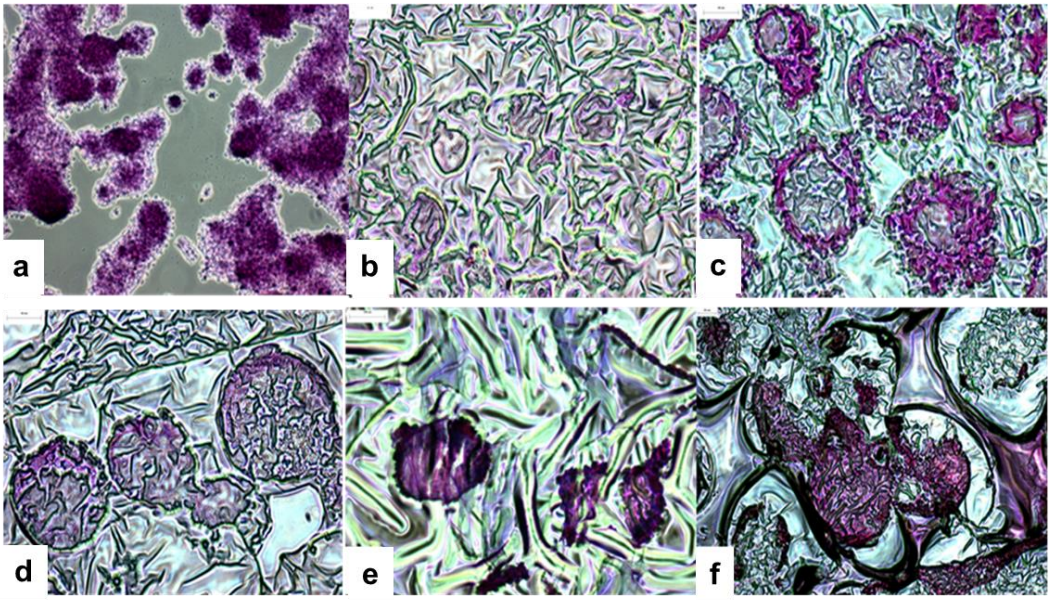

Figure 4.11 PAS staining of EBs in ICC hydrogel scaffolds on Day 21. Stained hepatocytes are as control (**a**). EBs (**b-f**) are obtained by ICC scaffolds with diameters of 90,170,200,270 and 400µm. Images are the cross-sections of scaffolds, which means the stained cells are from middle-plane of EBs.

In this case, the glycogen is possibly stored in myocyte-like cells which are from ectoderm of an embryo during the differentiation.[42,43] In contrast, glycogen stained bright pink was shown in cross-sections of EBs in diameters of 270um,

400um which had large amount (>80%) of hepatic glycogen-stained cells (**Figure 4.12**). These accumulations of PAS-positive material are seen as pink areas throughout the EBs. This result was also consistent with the expressions of early stage markers of differentiation for endoderm layer and hepatic specialized markers. From these results, we concluded that the optimal diameter of circular domains for hepatic differentiation was 201.7±29.6 μm under the present experimental conditions.

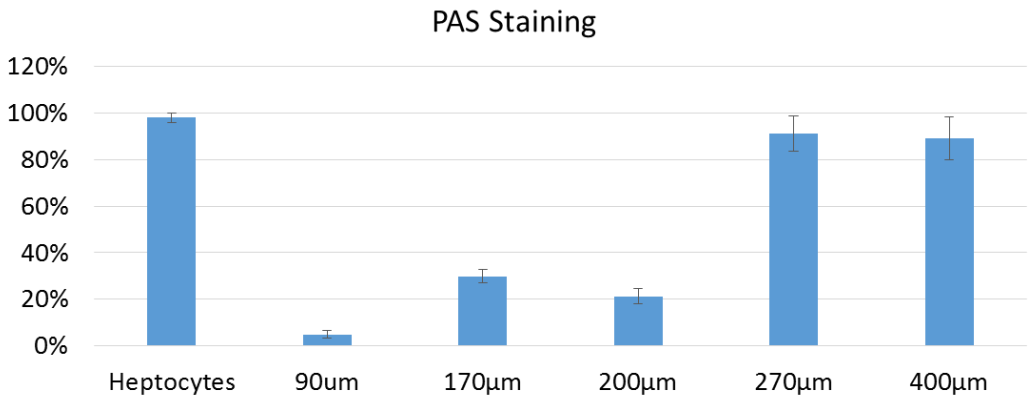

Figure 4.12 Quantitative evaluation of optical images with PAS staining

4.5 Conclusions

This work demonstrated that ICC scaffolds with controllable size of pores was able to form uniform EBs within a narrow size distribution. Derivation of EBs from scaffolds with interconnected pores facilitating cell-cell communication. These functional EBs could be differentiated into hepatocyte-like cells in certain degrees. Expression of hepatic differentiation markers and liver-specific function were demonstrated to be strongly dependent on the diameter of EBs. We anticipate the presented system will contribute to the development of various physiological and pathophysiological 3D tissue models which can be served as a valuable tool for understanding *in vitro* differentiation from ES cells for personalized cell therapy and drug screening. In addition. these result support the 3D cell culture platform for NP transport evaluation in potential preclinical patient/disease-specific study.

4.6 References

(1) Tasnim, F.; Phan, D.; Toh, Y.-C.; Yu, H. Cost-Effective Differentiation of Hepatocyte-like Cells from Human Pluripotent Stem Cells Using Small Molecules. *Biomaterials* **2015**, *70*, 115–125.

(2) Wobus, A. M.; Boheler, K. R. Embryonic Stem Cells: Prospects for Developmental Biology and Cell Therapy. *Physiol. Rev.* **2005**, *85*, 635–678.

(3) Burridge, P. W.; Anderson, D.; Priddle, H.; Barbadillo Muñoz, M. D.; Chamberlain, S.; Allegrucci, C.; Young, L. E.; Denning, C. Improved Human Embryonic Stem Cell Embryoid Body Homogeneity and Cardiomyocyte Differentiation from a Novel V-96 Plate Aggregation System Highlights Interline Variability. *Stem Cells* **2007**, *25*, 929–938.

(4) Messana, J. M.; Hwang, N. S.; Coburn, J.; Elisseeff, J. H.; Zhang, Z. Size of the Embryoid Body Influences Chondrogenesis of Mouse Embryonic Stem Cells. *J. Tissue Eng. Regen. Med.* **2008**, *2*, 499–506.

(5) Ng, E. S.; Davis, R.; Stanley, E. G.; Elefanty, A. G. A Protocol Describing the Use of a Recombinant Protein-Based, Animal Product-Free Medium (APEL) for Human Embryonic Stem Cell Differentiation as Spin Embryoid Bodies. *Nat. Protoc.* **2008**, *3*, 768–776.

(6) Mohr, J. C.; Zhang, J.; Azarin, S. M.; Soerens, A. G.; de Pablo, J. J.; Thomson, J. A.; Lyons, G. E.; Palecek, S. P.; Kamp, T. J. The Microwell Control of Embryoid Body Size in Order to Regulate Cardiac Differentiation of Human Embryonic Stem Cells. *Biomaterials* **2010**, *31*, 1885–1893.

(7) Hwang, Y.-S.; Chung, B. G.; Ortmann, D.; Hattori, N.; Moeller, H.-C.; Khademhosseini, A. Microwell-Mediated Control of Embryoid Body Size Regulates Embryonic Stem Cell Fate via Differential Expression of WNT5a

and WNT11. *Proc. Natl. Acad. Sci. U. S. A.* **2009**, *106*, 16978–16983.

(8) Jones, E. A.; Tosh, D.; Wilson, D. I.; Lindsay, S.; Forrester, L. M. Hepatic Differentiation of Murine Embryonic Stem Cells. *Exp. Cell Res.* **2002**, *272*, 15–22.

(9) Sivertsson, L.; Synnergren, J.; Jensen, J.; Björquist, P.; Ingelman-Sundberg, M. Hepatic Differentiation and Maturation of Human Embryonic Stem Cells Cultured in a Perfused Three-Dimensional Bioreactor. *Stem Cells Dev.* **2013**, *22*, 581–594.

(10) Takayama, K.; Inamura, M.; Kawabata, K.; Katayama, K.; Higuchi, M.; Tashiro, K.; Nonaka, A.; Sakurai, F.; Hayakawa, T.; Furue, M. K.; *et al.* Efficient Generation of Functional Hepatocytes from Human Embryonic Stem Cells and Induced Pluripotent Stem Cells by HNF4α Transduction. *Mol. Ther.* **2012**, *20*, 127–137.

(11) Behbahan, I. S.; Duan, Y.; Lam, A.; Khoobyari, S.; Ma, X.; Ahuja, T. P.; Zern, M. A. New Approaches in the Differentiation of Human Embryonic Stem Cells and Induced Pluripotent Stem Cells toward Hepatocytes. *Stem Cell Rev.* **2011**, *7*, 748–759.

(12) Huang, C.-C.; Liao, C.-K.; Yang, M.-J.; Chen, C.-H.; Hwang, S.-M.; Hung, Y.-W.; Chang, Y.; Sung, H.-W. A Strategy for Fabrication of a Three-Dimensional Tissue Construct Containing Uniformly Distributed Embryoid Body-Derived Cells as a Cardiac Patch. *Biomaterials* **2010**, *31*, 6218–6227.

(13) Ng, E. S.; Davis, R. P.; Azzola, L.; Stanley, E. G.; Elefanty, A. G. Forced Aggregation of Defined Numbers of Human Embryonic Stem Cells into Embryoid Bodies Fosters Robust, Reproducible Hematopoietic Differentiation. *Blood* **2005**, *106*, 1601–1603.

(14) Dias, A. D.; Unser, A. M.; Xie, Y.; Chrisey, D. B.; Corr, D. T. Generating Size-Controlled Embryoid Bodies Using Laser Direct-Write. *Biofabrication*

2014, *6*, 025007.

(15) Sasaki, D.; Shimizu, T.; Masuda, S.; Kobayashi, J.; Itoga, K.; Tsuda, Y.; Yamashita, J. K.; Yamato, M.; Okano, T. Mass Preparation of Size-Controlled Mouse Embryonic Stem Cell Aggregates and Induction of Cardiac Differentiation by Cell Patterning Method. *Biomaterials* **2009**, *30*, 4384–4389.

(16) Nguyen, D.; Sa, S.; Pegan, J. D.; Rich, B.; Xiang, G.; McCloskey, K. E.; Manilay, J. O.; Khine, M. Tunable Shrink-Induced Honeycomb Microwell Arrays for Uniform Embryoid Bodies. *Lab Chip* **2009**, *9*, 3338–3344.

(17) Xu, F.; Sridharan, B.; Wang, S.; Gurkan, U. A.; Syverud, B.; Demirci, U. Embryonic Stem Cell Bioprinting for Uniform and Controlled Size Embryoid Body Formation. *Biomicrofluidics* **2011**, *5*, 22207.

(18) Choi, Y. Y.; Chung, B. G.; Lee, D. H.; Khademhosseini, A.; Kim, J.-H.; Lee, S.-H. Controlled-Size Embryoid Body Formation in Concave Microwell Arrays. *Biomaterials* **2010**, *31*, 4296–4303.

(19) Kim, J.; Lee, J. M.; Chung, B. G. Microwell Arrays for Uniform-Sized Embryoid Body-Mediated Endothelial Cell Differentiation. *Biomed. Microdevices* **2014**, *16*, 559–566.

(20) Moon, S.-H.; Ju, J.; Park, S.-J.; Bae, D.; Chung, H.-M.; Lee, S.-H. Optimizing Human Embryonic Stem Cells Differentiation Efficiency by Screening Size-Tunable Homogenous Embryoid Bodies. *Biomaterials* **2014**, *35*, 5987–5997.

(21) Nakazawa, K.; Yoshiura, Y.; Koga, H.; Sakai, Y. Characterization of Mouse Embryoid Bodies Cultured on Microwell Chips with Different Well Sizes. *J. Biosci. Bioeng.* **2013**, *116*, 628–633.

(22) Lee, J.; Cuddihy, M. J.; Kotov, N. A. Three-Dimensional Cell Culture

Matrices: State of the Art. *Tissue Eng. Part B. Rev.* **2008**, *14*, 61–86.

(23) Montanez-Sauri, S. I.; Beebe, D. J.; Sung, K. E. Microscale Screening Systems for 3D Cellular Microenvironments: Platforms, Advances, and Challenges. *Cell. Mol. Life Sci.* **2014**, *72*, 237–249.

(24) Duarte, A. R. C.; Mano, J. F.; Reis, R. L. Thermosensitive Polymeric Matrices for Three-Dimensional Cell Culture Strategies. *Acta Biomater.* **2011**, *7*, 526–529.

(25) Griffith, L. G.; Swartz, M. A. Capturing Complex 3D Tissue Physiology in Vitro. *Nat. Rev. Mol. Cell Biol.* **2006**, *7*, 211–224.

(26) Kotov, N. A.; Liu, Y.; Wang, S.; Cumming, C.; Eghtedari, M.; Vargas, G.; Motamedi, M.; Nichols, J.; Cortiella, J. Scaffolds. **2004**, *20*.

(27) Lee, J.; Lilly, G. D.; Doty, R. C.; Podsiadlo, P.; Kotov, N. A. In Vitro Toxicity Testing of Nanoparticles in 3D Cell Culture. *Small* **2009**, *5*, 1213–1221.

(28) Astashkina, A.; Grainger, D. W. Critical Analysis of 3-D Organoid in Vitro Cell Culture Models for High-Throughput Drug Candidate Toxicity Assessments. *Adv. Drug Deliv. Rev.* **2014**, *69-70*, 1–18.

(29) Lee, J.; Cuddihy, M. J.; Cater, G. M.; Kotov, N. a. Engineering Liver Tissue Spheroids with Inverted Colloidal Crystal Scaffolds. *Biomaterials* **2009**, *30*, 4687–4694.

(30) Matsumoto, K.; Mizumoto, H.; Nakazawa, K.; Ijima, H.; Funatsu, K.; Kajiwara, T. Hepatic Differentiation of Mouse Embryonic Stem Cells in a Three-Dimensional Culture System Using Polyurethane Foam. *J. Biosci. Bioeng.* **2008**, *105*, 350–354.

(31) Liu, T.; Zhang, S.; Chen, X.; Li, G.; Wang, Y. Hepatic Differentiation of

Mouse Embryonic Stem Cells in Three-Dimensional Polymer Scaffolds. *Tissue Eng. Part A* **2010**, *16*, 1115–1122.

(32) Kulkarni, J. S.; Khanna, A. Functional Hepatocyte-like Cells Derived from Mouse Embryonic Stem Cells: A Novel in Vitro Hepatotoxicity Model for Drug Screening. *Toxicol. Vitr.* **2006**, *20*, 1014–1022.

(33) Matoba, R.; Niwa, H.; Masui, S.; Ohtsuka, S.; Carter, M. G.; Sharov, A. A.; Ko, M. S. H. Dissecting Oct3/4-Regulated Gene Networks in Embryonic Stem Cells by Expression Profiling. *PLoS One* **2006**, *1*, e26.

(34) Loh, Y.-H.; Wu, Q.; Chew, J.-L.; Vega, V. B.; Zhang, W.; Chen, X.; Bourque, G.; George, J.; Leong, B.; Liu, J.; *et al.* The Oct4 and Nanog Transcription Network Regulates Pluripotency in Mouse Embryonic Stem Cells. *Nat. Genet.* **2006**, *38*, 431–440.

(35) Hermitte, S.; Chazaud, C. Primitive Endoderm Differentiation: From Specification to Epithelium Formation. *Philos. Trans. R. Soc. Lond. B. Biol. Sci.* **2014**, *369*.

(36) Capo-Chichi, C. D.; Rula, M. E.; Smedberg, J. L.; Vanderveer, L.; Parmacek, M. S.; Morrisey, E. E.; Godwin, A. K.; Xu, X.-X. Perception of Differentiation Cues by GATA Factors in Primitive Endoderm Lineage Determination of Mouse Embryonic Stem Cells. *Dev. Biol.* **2005**, *286*, 574–586.

(37) Schwartz, R. E.; Linehan, J. L.; Painschab, M. S.; Hu, W.-S.; Verfaillie, C. M.; Kaufman, D. D. S. Defined Conditions for Development of Functional Hepatic Cells from Human Embryonic Stem Cells. **2006**.

(38) Ben-Ze'ev, A.; Robinson, G. S.; Bucher, N. L.; Farmer, S. R. Cell-Cell and Cell-Matrix Interactions Differentially Regulate the Expression of Hepatic and Cytoskeletal Genes in Primary Cultures of Rat Hepatocytes. *Proc. Natl. Acad. Sci. U. S. A.* **1988**, *85*, 2161–2165.

(39) Kim, K.; Ohashi, K.; Utoh, R.; Kano, K.; Okano, T. Preserved Liver-Specific Functions of Hepatocytes in 3D Co-Culture with Endothelial Cell Sheets. *Biomaterials* **2012**, *33*, 1406–1413.

(40) Zhu, S.; Rezvani, M.; Harbell, J.; Mattis, A. N.; Wolfe, A. R.; Benet, L. Z.; Willenbring, H.; Ding, S. Mouse Liver Repopulation with Hepatocytes Generated from Human Fibroblasts. *Nature* **2014**, *508*, 93–97.

(41) Sanal, M. G. Cell Therapy from Bench to Bedside: Hepatocytes from Fibroblasts - the Truth and Myth of Transdifferentiation. *World J. Gastroenterol.* **2015**, *21*, 6427.

(42) Bhanot, H.; Reddy, M. M.; Nonami, A.; Weisberg, E. L.; Bonal, D.; Kirschmeier, P. T.; Salgia, S.; Podar, K.; Galinsky, I.; Chowdary, T. K.; *et al.* Pathological Glycogenesis through Glycogen Synthase 1 and Suppression of Excessive AMP Kinase Activity in Myeloid Leukemia Cells. *Leukemia* **2015**, *29*, 1555–1563.

(43) Lee, Y.-C.; Chang, C.-J.; Bali, D.; Chen, Y.-T.; Yan, Y.-T. Glycogen-Branching Enzyme Deficiency Leads to Abnormal Cardiac Development: Novel Insights into Glycogen Storage Disease IV. *Hum. Mol. Genet.* **2011**, *20*, 455–465.

Chapter V

Preliminary study for 3D Stem Cell Culture:

Layer-by-Layer Surface Modification for

Bone Marrow Stromal Cells Culture in ICC Scaffold

5.1 Abstract

The bone marrow microenvironment containing bone marrow stromal cells (BMSCs) and complex set of chemical and physical cues provides the structural and physiological support for hematopoietic stem cells (HSCs). Better understanding and appropriate tools to control BMSCs signaling are important in emulating HSC niches *ex-vivo.* However, there are difficulties associated with drug discovery for immunotherapy and bone tissue engineering to which BMSCs are essential. Although BMSCs have the potential to replicate as undifferentiated cells

or differentiate to lineages of mesenchymal tissues, including bone, cartilage, fat, tendon, muscle, and marrow stroma, the fate of BMSCs within bone marrow niche in three-dimensional (3D) matrices *in vitro* or *in vivo* are still unknown. In this chapter, we discuss the BMSCs grown in 3D Inverted Colloidal Crystal scaffolds, layer-by-layer 3D surface modification is utilized and allow controllable cues in 3D porous structures. The results show clay/PDDA modified surface in 3D matrice promote BMSC differentiated to Chondrogenic lineages which indirectly influenced from the bone mimetic coating.

5.2 Introduction

The bone marrow microenvironment containing bone marrow stromal cells (BMSCs)[1] and complex set of chemical and physical cues [1–3] provides the structural and physiological support for hematopoietic stem cells (HSCs) by presenting membrane-bound ligands, secreting chemokines and potentially other intercellular signaling processes [4]. A large amount of studies have proved the necessity of BMSCs for the maintenance of HSCs in long-term culture *in vitro*[5–7] that are increasingly applied to regenerative medicine, immune therapies and personalized immune response of new drugs.[8–10] Therefore, comprehensive understanding and appropriate methods of control of BMSCs signaling are important in emulating HSC niches *ex-vivo*.[1,2,8]

BMSCs have the potential to replicate as undifferentiated cells or differentiate to lineages of mesenchymal tissues, including bone, cartilage, fat, tendon, muscle, and marrow stroma.[11–13] Like many stem cells, BMSCs may differentiate into distinct lineages depending on which cues are present in the cell culture environment[14,15] such as growth factors,[16] cell adhesion,[17] cell shape,[18] mechanical forces,[19] and substrate rigidity[20,21]. However, although differentiation fate for hematopoietic stem cells and other stem cells is partially known[8,22,23], the fate of BMSCs co-cultured with them as well as the factors that control the phenotype and morphology are still puzzling. Three dimensional (3D) cultures in engineered scaffolds have been used as a tool to study cell-cell and cell-matrix interactions for recent decade, for instance, to investigate the role of specific cues in affecting HSC fate [9,18,20,21,24–26]. The controllable surface properties and existing data on HSCs in 3D matrices enable the 3D engineered scaffold a promising tool to understand BMSC in bone marrow microenvironment. Surface properties of these scaffolds were often modulated through the attachment of specific functional groups or proteins with necessary biological functions to regulate cellular behavior, however, fewer techniques can be applicable to existing 3D substrates other than two dimensional (2D) biological surface modification methods because of limited diffusivity within the porous internal structures. In addition, physical properties of the scaffolds such as stiffness of the scaffolds are generally modified by changing the composites of materials. Layer-by-layer (LBL) surface coating is a promising technique to modify 3D matrix surface properties with various materials and this

method is able to obtain different physical properties without re-fabricating the scaffolds.[27–29]

In this chapter, Inverted colloidal crystal (ICC) scaffolds with LBL bone mimetic surface modification are used to study the behavior of BMSCs in 3D culture *ex-vivo*. 3D cell culture scaffolds with porous structures can be coated using the LBL technique as long as there is no serious mass transport limitation.[30,31] To provide adequate adhesion of stromal cells, the pore surface of ICC hydrogel scaffolds was coated with clay and Polydiallyldimethylammonium chloride (PDDA) multilayer following the LBL technology[32]. PDDA is a positively charged polymer, while clay is negatively charged nano-sized particles. The thin layer of nano-composite prepared on the surface of the scaffold is mechanically compatible with the hydrogel; the clay layer create a bone-mimetic coated surface of 3D scaffolds with its nanoscale roughness, increased charging on the surface, and created much stiffer film than original composites as hydrogel. [30,31,33,34]

5.3 Materials and Methods

5.3.1 LBL surface modification on ICC scaffolds

Fabrication technology of the primary ICC hydrogel scaffold was described in Chapter 2 and Chapter 4. Polystyrene (PS) beads with diameter of 120um were used instead of glass beads.[34] The surfaces of scaffolds were coated with the sequential deposition of positively charged 0.5 wt%

Polydiallyldimethylammonium chloride (PDDA, Sigma, MW= 200 000) solution for 30 min, and a negatively charged 0.5 wt% clay nanoparticles with average 1 nm thick and 70–150 nm in diameter (Southern Clay Products) dispersion for 30 min. (**Scheme 5.1**) Each adsorption step was followed by rinsing in deionized water for 30 min, and all processes were performed under a gentle flow generated by a stirrer in a beaker. Cyclic repetition of the polymer adsorption, rinsing, clay adsorption and rinsing process was carried out 3, 5 and 7 times and all process ended with clay layer.

5.3.2 Bone marrow stromal cell culture

Human bone marrow stromal cells HS-5 (CRL-11882, ATCC) were cultured with DMEM with 4mM L-glutamine, 4.5g/L glucose, 1.5g/L sodium bicarbonate, 10%(v/v) fetal bovine serum (FBS), and 1%(v/v) penicillin-streptomycin. Firstly, cells are maintained in T-75 culture flasks (Bottom area: 75cm^2). Once cell growth reached approximately 80% confluence, they were detached from the culture flask using 0.25% (v/v) trypsin–EDTA solution and 10^5 cells were seeded on top of UV-sterilized scaffolds which were then placed in a 96-well plate. Culture volume was maintained 250 μL and media was changed every other day. In order to characterize stromal cell growth in 3D scaffolds, HS-5 cells were stained with 5μM cell tracker green CMFDA dye in some cases. HS-5 cells are cultured in scaffolds for 5 days. The cells growing within the LBL-modified scaffolds were imaged under an Zeiss confocal microscope with 10× or 20×

objective. A 488 nm laser was used for excitation and emission signals were collected within 515–550nm window. Transmission image was overlaid with fluorescent image to confirm the location of cells within pores.

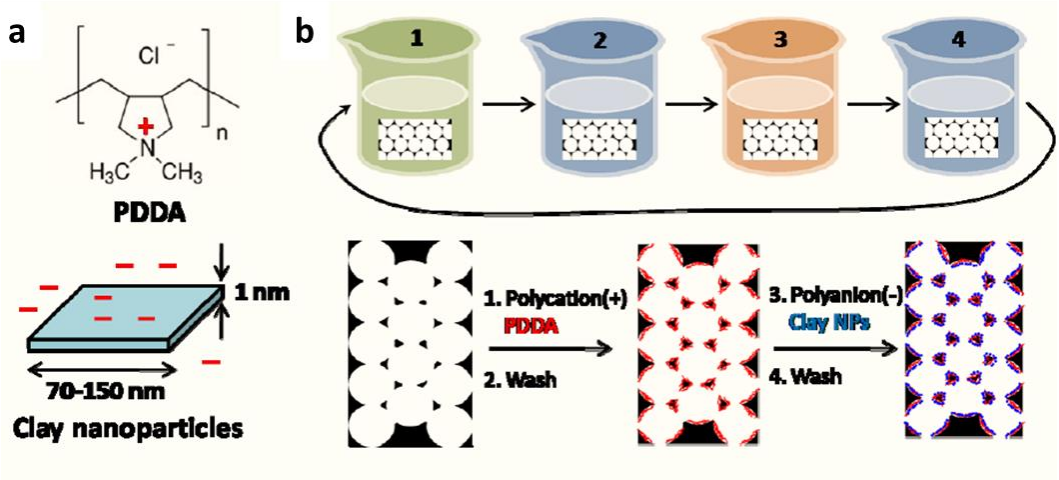

Scheme 5.1 Schematic of clay/PDDA LBL surface coating of ICC hydrogel scaffold. **(a)** Schematic of PDDA and Clay nanoparticles. **(b)** Schematic of LBL surface coating procedure.

5.3.3 Viability of BMSCs in scaffolds

Standard live/dead cell viability assays, were used to observe viability of BMSCs in ICC scaffolds with or without LBL modification. The assay consisted of calcein AM and ethidium homodimer (EthD-1) addressing plasma membrane integrity and esterase activity. The result indicated that the BMSCs proliferate normally in contact with surface of scaffolds. Cell viability was verified by counting the cell number. (**Figure 5.2**)

5.3.4 Immunostaining of bone marrow stromal cells in three potential lineages

Cultured HS-5 cells grown in scaffolds after 7 days and 21 days were fixed with 4% freshly prepared paraformaldehyde for 20min at room temperature. For specific protein detection such as nuclear proteins, the cells were permeated with 0.3% Triton X-100 (Sigma, USA) for 5min at room temperature followed by aspirating the fixative. Cells were washed three times for 5min each with PBS after membrane permeation. Non-specific binding was blocked with PBS containing 1% rabbit serum in PBS for 2h at room temperature.

The cells cultured for 7 days were then incubated with primary antibodies ((Santa Cruz, USA): the chondrocyte-specific marker Sox-9 and collagen type II (COL2A) [35,36], and osteocyte-specific marker, alkaline phosphatase (ALP) and runt-related transcription factor 2 (RUNX2) in 10% rabbit or mouse serum overnight at 4 °C [37–39]. Next, the cells were washed with PBS three times for 5 min each. The cells were then incubated with secondary antibodies anti-rabbit-FITC for (Santa Cruz, USA; 1:500) in 0.1% rabbit or mouse serum at 37 °C for 30min. After giving three washes (5min) with PBS, the cells were exposed to 1mg/ml DAPI (4', 6-diamidino-2-phenylindole) solution for 1min. As a result, the nucleus of cells are stained as blue. After washing the cells twice for 5min each with 1× PBS, they were

ready for confocal imaging. Images were analyzed by ImageJ software (http://rsbweb.nih.gov/ij/). Following 21 days culture period, adipogenic markers peroxisome proliferator-activated receptor (PPARγ2) and acyl-CoA synthetase (ACSL5) were examined by the same method above[40,41].

5.3.5 SEM of bone marrow stromal cells grown in ICC scaffolds

To investigate the attachment, spreading and differentiated morphologies of BMSC layer on scaffolds, the time points 3, 9, and 14 days were selected. After 3, 9, and 14 days of culturing, samples were prepared for scanning electron microscopy as follows. Firstly, the medium on these samples was replaced with 2.5% glutaraldehyde in EMEM without serum and fixed for 30 min at room temperature. Then they were washed by PBS (pH 7.2) for three times (15min). The samples were dehydrated through a graded series of ethanol from 50, 60, 70, 80, 95, and 100%. The specimens were mounted on aluminum holders and sputter-coated with conducting layer of gold platinum for 90 seconds. The samples were examined by scanning electron microscopy, using a voltage of 5 kV.

5.4 Results and Discussion

Surface properties of the scaffolds that determine cell adhesion and other substrate-cell interactions represent some of these factors. In this work, we studied the behaviors of BMSCs in regard to the changes of substrate properties in an artificial bone marrow matrix *in vitro* based on a 3D scaffold with inverted colloidal crystal (ICC) geometry. Highly uniform pores in ICC scaffolds with a diameter of 120 μm mimic the geometry of actual bone marrow matrix[34] (**Figure 5.1a**). Besides that the structure of ICC scaffolds offer other benefits for bone tissue engineering such as a high degree of structural control, complete interconnectivity of cavities, and mechanical robustness.[34] To understand the effect of cell adhesion and substrate property changes on BMSC supportive layer, scaffolds were coated with layers of transparent bone –mimetic nanocomposite. It was created on the surface of ICC scaffolds by LBL assembly from clay nanoplatelets and polydiallyldimethylammonium bromide (PDDA).[27,28] The LBL coating was started with a PDDA layer and finished with a clay layer as to support stromal cell adhesion.[42] Seven bi-layers of clay/PDDA nanocomposite in ICC surface was visualized by confocal microscopy using FITC as fluorescent label that was added to PDDA during the deposition. The feasibility of 3D LBL coating was confirmed by green fluorescence nicely formed 3D clay/PDDA LBL film was observed under confocal microscope. (**Figure 5.1b**)

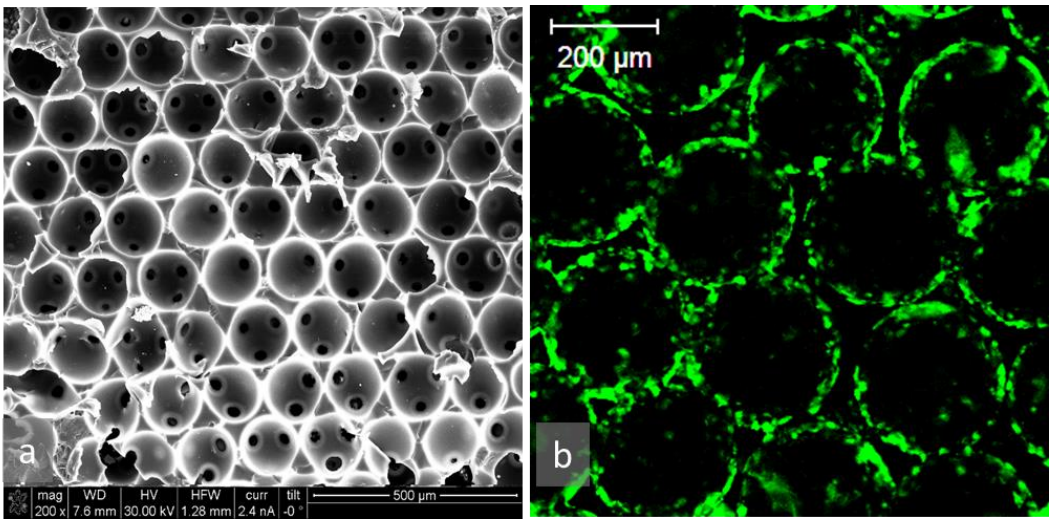

Figure 5.1 ICCs were prepared with PS beads as template (***D***=120µm). (**a**) All pores are open to the outer fluid which facilitates cell motility and media exchange in a dynamic culture condition. Seven bilayers of fluorescent labeled PDDA (green) and clay NPs on ICC hydrogel scaffold soaked in phosphate buffered saline (**b**).

Human bone marrow stromal cell line, HS-5, were used to investigate cellular responses of the support stromal cells to surface properties of bone marrow scaffold *in vitro*, This cell line was stabilized and generally used as support cells for hematopoietic stem cells[7,43], which can provide growth factors and signaling communication to stem cells to mimic the bone marrow stromal tissue function. Established bone marrow stromal cell line HS-5 were seeded in the scaffolds and maintained in specific culture media. Live/Dead Viability/Cytotoxicity kit (Life Technologies), which consisted of calcein AM and ethidium homodimer (EthD-1) addressing plasma membrane integrity and esterase activity, was used to monitor

the growth and viability of BMSCs in the scaffolds on day 3, 9 and 14 under the confocal microscope. In the confocal images, green cells are alive, while cells stained red are dead. Cells in the scaffold with and without LBL coating both appeared in green while there was no cell stained in red. The result indicated the cells maintained good viabilities in both types of scaffolds (**Figure 5.2**). In addition, the confocal images also show the cells have better adhesion on the LBL coated ICC scaffolds and most of the cells formed thick plaques on the pore surface. In contrast, the cells in control scaffolds without LBL coating tend to aggregate in the center of the pores and formed small spherical clusters.

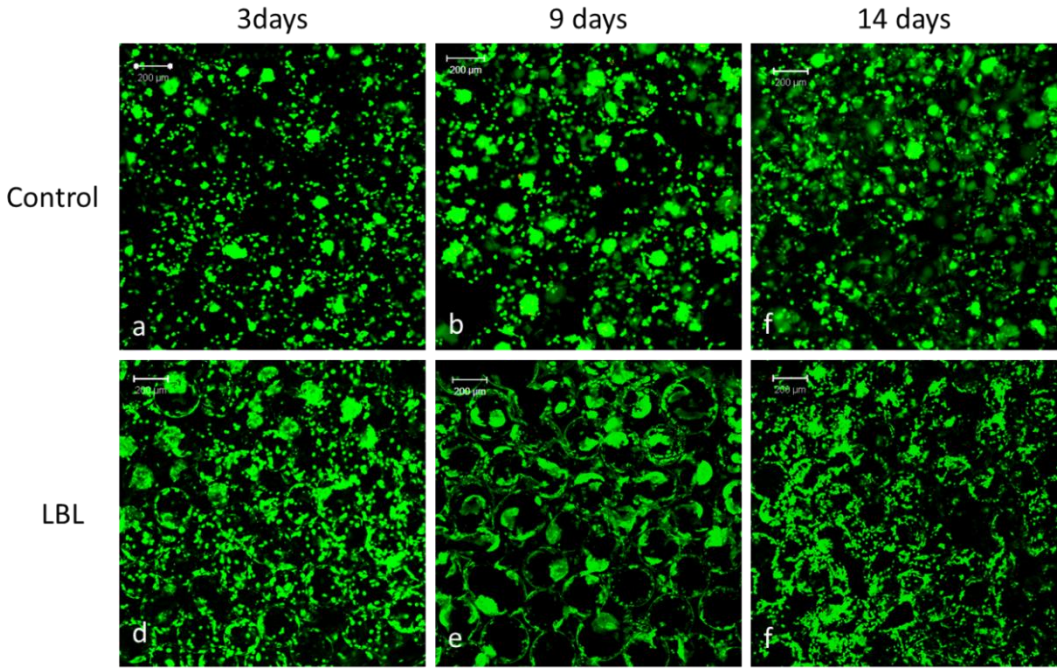

Figure 5.2 HS-5 cells were cultured on non-coated ICC hydrogel scaffolds as control (**a-c**) and scaffolds with 7 bi-layers of PDDA-Clay (**d-f**). Confocal images were taken on day 3, 9 and 14 where cells were stained with Live/Dead Viability/Cytotoxicity kit. Cell density at seeding is 80,000 cells/scaffold for all the groups. Scale bar: 200µm.

This trend became obvious after 9 days of culturing (**Figure 5.2e, f**). Coated clay particles created nanoscale roughness, increased charging on the surface, and created much stiffer film than hydrogel[32,34]. Increase of Young modulus of the scaffolds (**Figure 5.3**) was also a primary factor improving the adhesion of cells to materials [44]. Therefore, the changing of cell aggregation with LBL coating is due to clay surface which enhanced BMSCs adhesion on the substrate, thereby change the shape and morphology of cells.

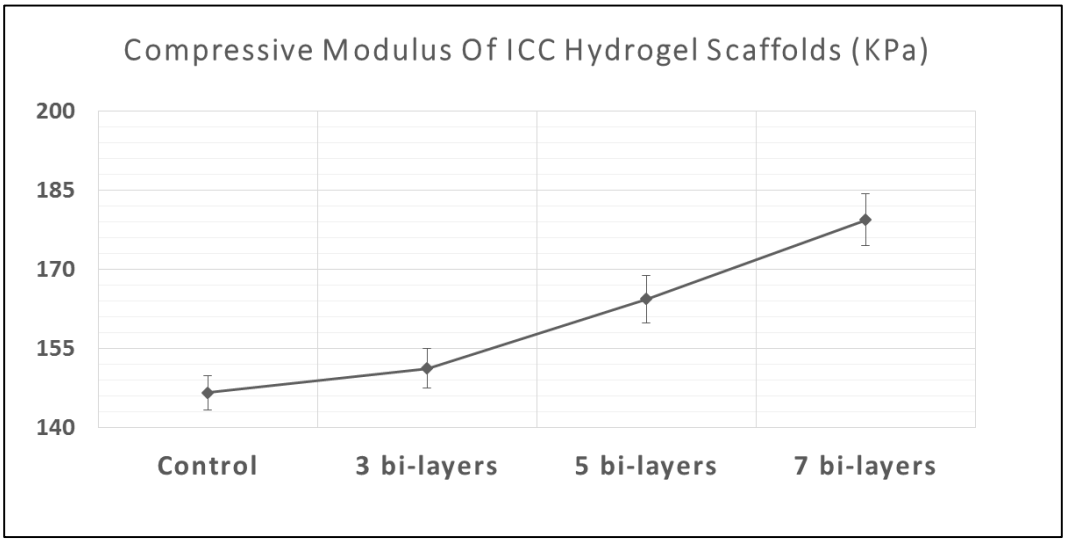

Figure 5.3 Young Modulus. The compressive modulus of ICC scaffolds with 3, 5, 7 bi-layers of clay/PDDA modification. The compressive modulus was within the range of normal articular cartilage and increased with the number of bi-layers by LBL.

The cells were extracted from the scaffolds right after imaging on day 3, 9 and 14 and the density of cells were evaluated in all groups of scaffolds. As a result, without LBL the cells proliferated faster and achieved 1340,000 ±50,000 cells/scaffold comparing to 725,000±25,000 cells/scaffold in the LBL group from the original density (**Figure 5.4**). Two potential factors can be considered to result in difference of cell proliferation. One is that the better adhesion of cells on the LBL-modified surface in scaffold prevented the agitating off the cells from the substrates in the same experimental condition. The other is that BMSCs in LBL-modified scaffolds spontaneously differentiated and transformed to specific lineages of cells, hence the reduction of self-renewal cells and increase of differentiated cells were observed in the 3D culture [45–47]. The LBL-modified scaffolds were examined under optical microscope after trypsin treatment and extraction of cells, however, only few cells still attached on the surface which exclude the former potential cause. Although the phenotypic and functional properties of HS-5 cell line have been characterized [7,43], the fundamental question of how or whether self-renewal is regulated remains unclear. In most cases, HS-5 cells as supporting cells shall maintain potent proliferation with HSCs culturing, however, the differentiation of BMSCs cannot be prevented in long-term cultures[48]. Thereby, the potential differentiation of HS-5 cells may be the primary cause of density difference between control ICC scaffolds without LBL and LBL-modified ICC scaffolds, as well as the morphology change toward plaque-shaped BMSCs clusters in LBL-modified scaffolds.

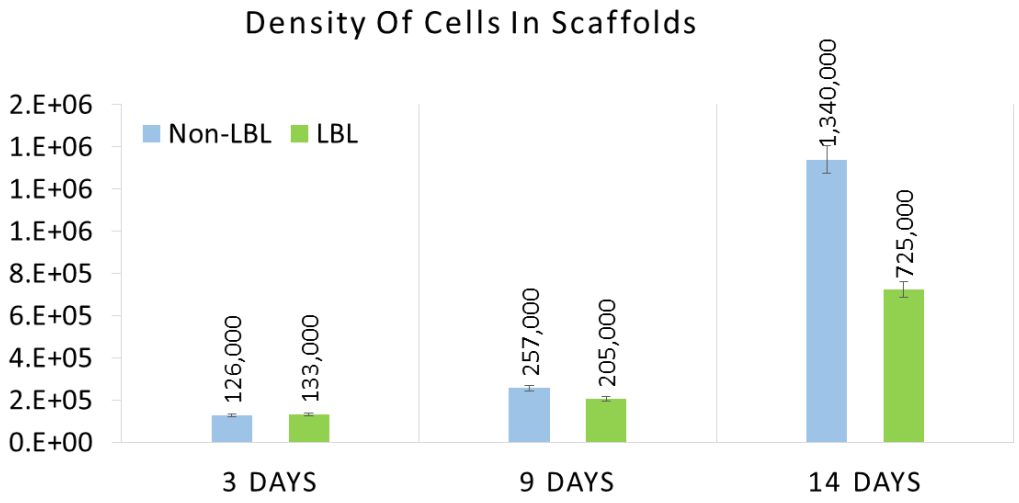

Figure 5.4 HS-5 cells were cultured on ICC hydrogel scaffolds as control (non-LBL) and scaffolds with 7 bi-layers of PDDA-Clay. Cells per scaffold were counted on day 3, 9 and 14 under microscope on hemocytometer.

To verify the morphology change of BMSCs clusters in LBL scaffolds, SEM images were taken after culturing for 9 days. In control ICC scaffold the cells did not strongly adhere to the surface and have been washed away during the sample preparation, even without trypsin treatment (**Figure 5.5a, b**), meanwhile, dense plaques of cells were observed in LBL-modified scaffold (**Figure 5.5c, d**). Noticeably, the scaffolds with LBL still maintained the shape of uniform porous structure comparing to the deformed structure in control scaffold during the dehydration process since LBL coating enhance the stiffness of the 3D matrix.[12] Furthermore, nano-sized porous structure was observed on the surface of the BMSCs plaque (**Figure 5.5b**). This feature shared the similarity of the physical

appearance with cartilage tissue with porous and permeable extracellular environment consisting of chondrocytes *in vivo*.[49]

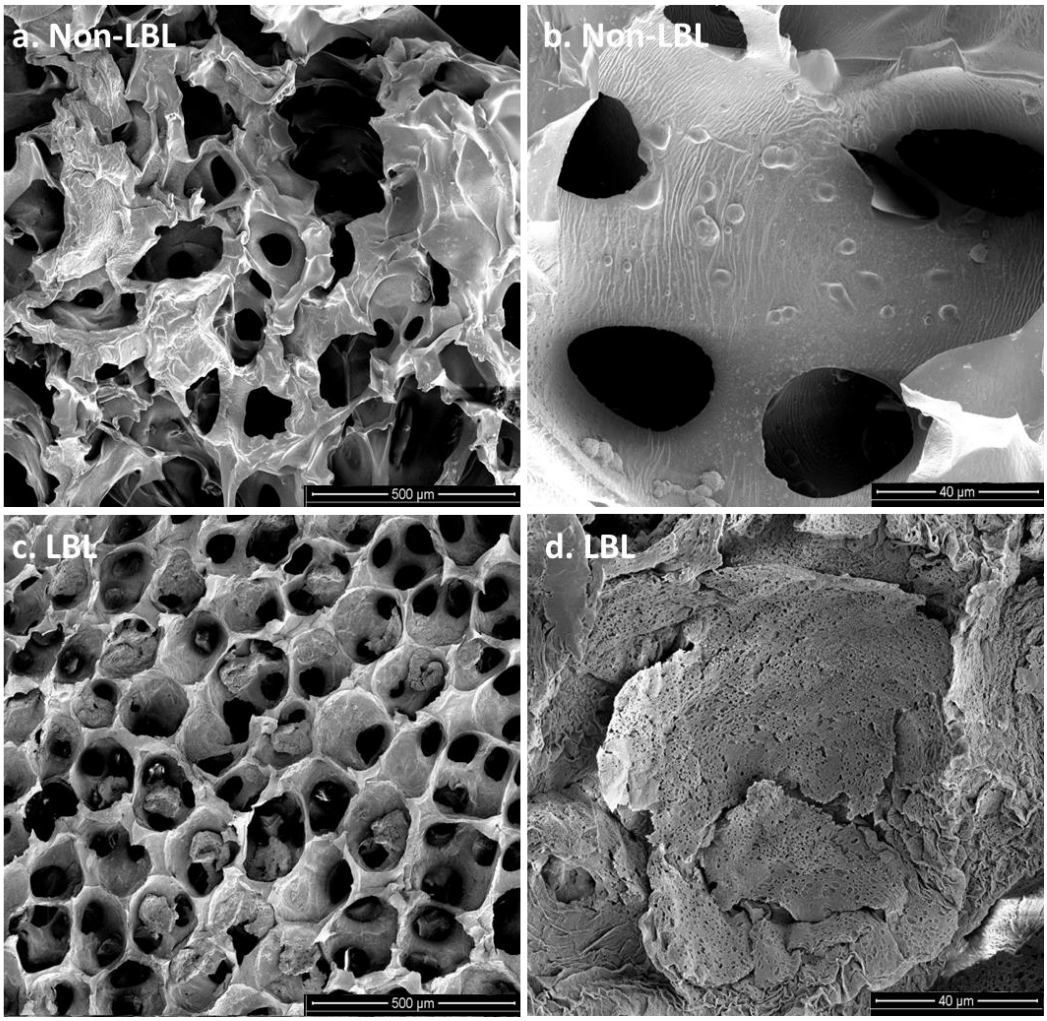

Figure 5.5 SEM images of of HS-5 cells on control scaffolds without coating (**a** and **b**) and on ICC scaffolds with 7 bi-layers of clay/PDDA (**c** and **d**).

As stated previously, BMSCs have the potential to differentiate into multiple lineages of cells in bone tissue such as adipocytes, chondrocytes and osteocytes aroused from the supporting complex structure.[13] LBL bone-mimetic modification on surface of scaffolds stimulated BMSCs forming bone-specific cells. To understand how LBL coating on the supporting scaffold influence cell phenotype change, protein markers of three lineages were studied by immunofluorescence staining. The chondrocyte-specific marker, Sox-9 and COL2A [35,36] (**Figure 5.6**), and osteocyte-specific marker, ALP and RUNX2, [37–39] were examined on day 7 of cell culture **(Figure 5.7**). Afterward, following 21 days culture period, adipogenic markers peroxisome proliferator-activated receptor (PPARγ2) and acyl-CoA synthetase (ACSL5) were observed at the end of the culture[40,41] and show very limited expressions **(Figure 5.8**).

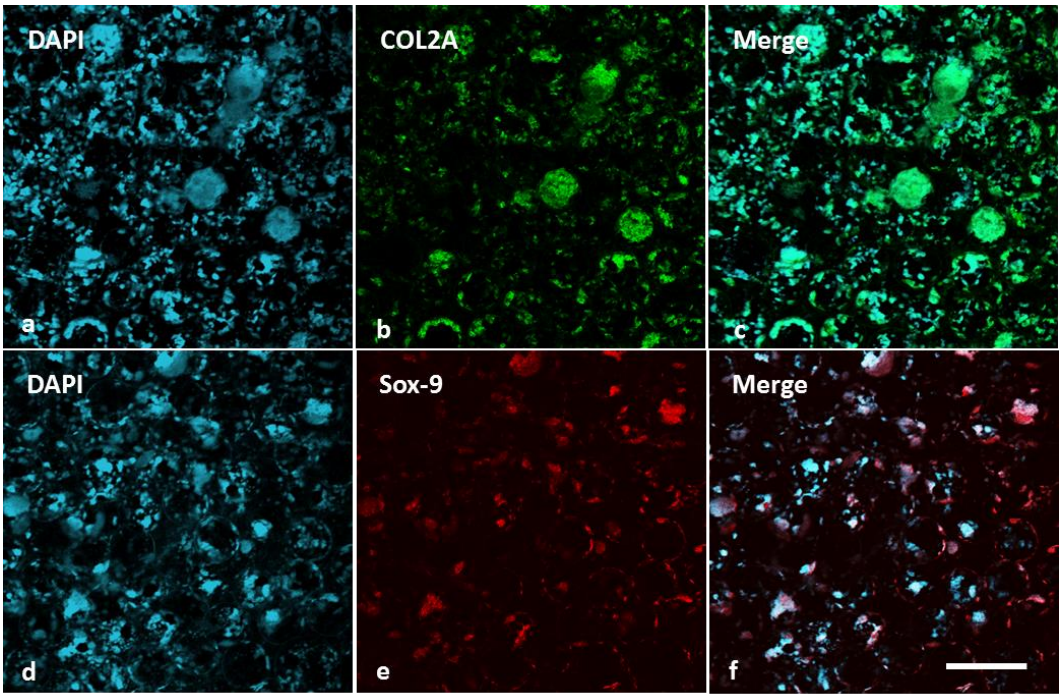

Figure 5.6 Immunofluorescence staining of lineage-specific markers of HS-5 Cells on LBL ICC scaffold with 7 bi-layers of PDDA/Clay coating: markers of chondrocytes (Sox-9 and COL2A). Scale bar: 200µm.

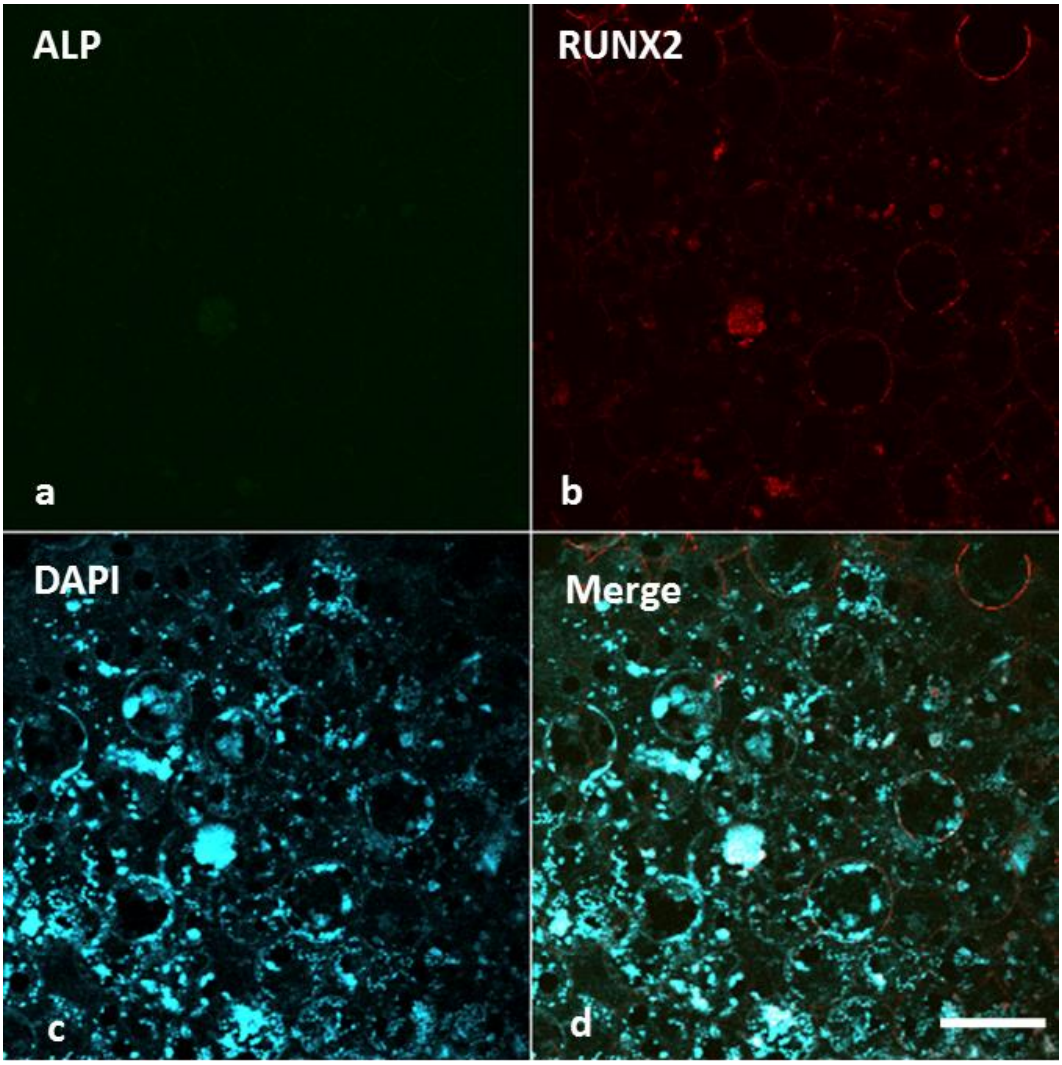

Figure 5.7 Immunofluorescence staining of lineage-specific markers of HS-5 Cells on LBL ICC scaffold with 7 bi-layers of PDDA/Clay coating: markers of osteocytes (ALP and RUNX2). Scale bar: 200μm.

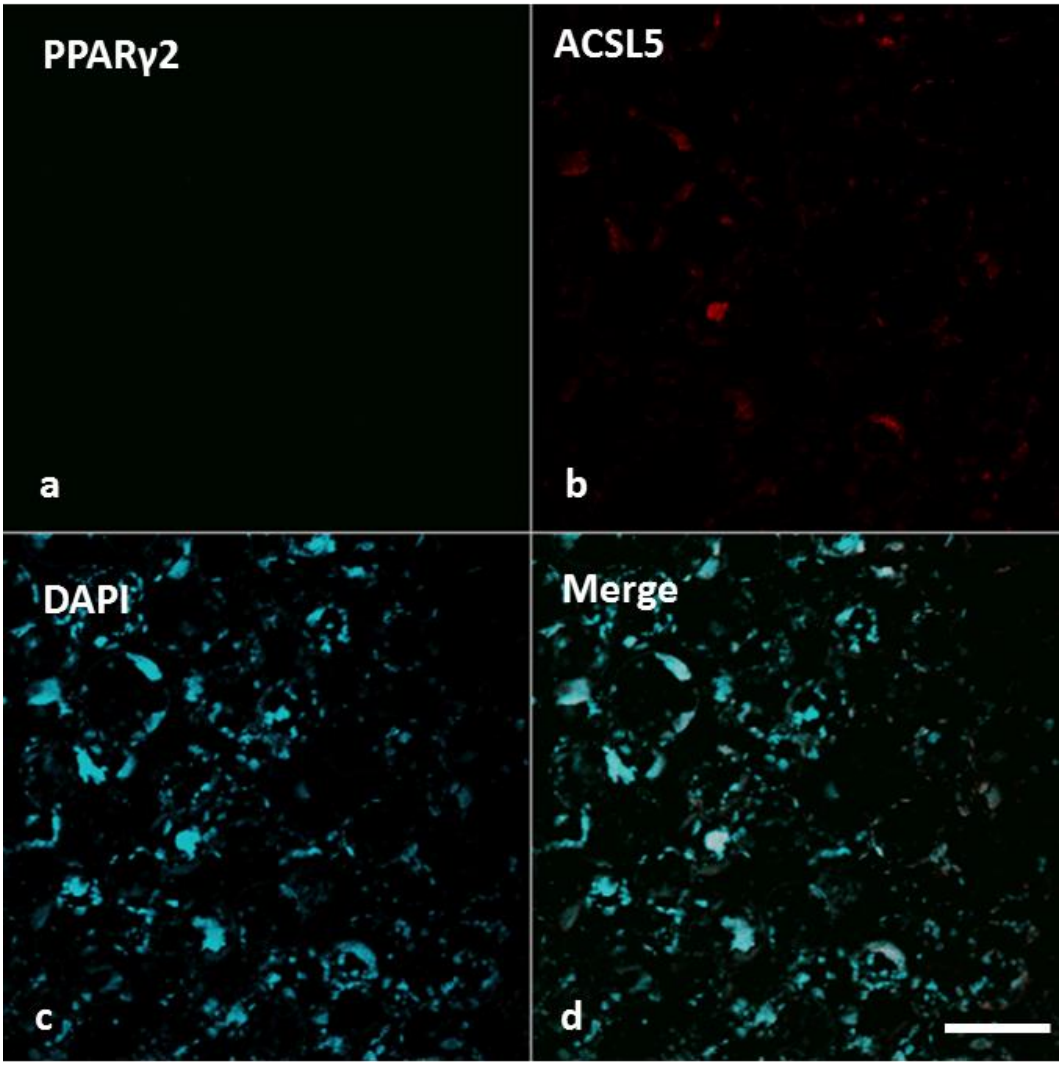

Figure 5.8 Immunofluorescence staining of lineage-specific markers of HS-5 Cells on LBL ICC scaffold with 7 bi-layers of PDDA/Clay coating markers of adipocytes (PPARγ2 and ACSL5). Scale bar: 200µm.

The quantitative analysis by image processing (**Method**) based on confocal images with immunofluorescence staining (**Figure 5.9)**. As a control in 2D culture before seeding in the ICC scaffolds, the expression of all markers for three lineages on day 7 and day 21 are significantly lower than in 3D matrix with LBL modification, which confirmed the gene expressions have changed with the transition of cells during the culturing in LBL ICC scaffolds. Sox-9 expressed 81.2±5.2% of cultured cells, which is a sign of activation in all pre-chondrogenic mesenchymal condensations. Cells with expression of COL2A is 53.2±3.8%, indicating a more active phenotype of chondrogenic status of cells.[35] Osteogentic markers, RUNX2 and ALP are expressed in 27.3±4.7% and 2.89±1.4% of all population respectively. At the early stage of phenotype change, RUNX2 determines the osteoblast lineage from bone marrow multipotent mesenchymal cells, and further induces ALP activity at later stage. Therefore, RUNX2 shows dominate expression comparing to ALP on day 7. However, osteogenic markers are still much lower than chondrogenic markers and shows insufficient features for osteogenesis towards mature osteocyte or osteoblast. Following a 21 day culture period, there was a significant upregulating of preadipocytes gene, ACSL5, in BMSCs compared with 2D cultured cells (**Figure 5.9**), while there is no mature adipocyte marker PPARγ2 expressed in BMSCs cultured on ICC scaffold with LBL coating. The result shows no sufficient adipogenesis in the 3D culture.

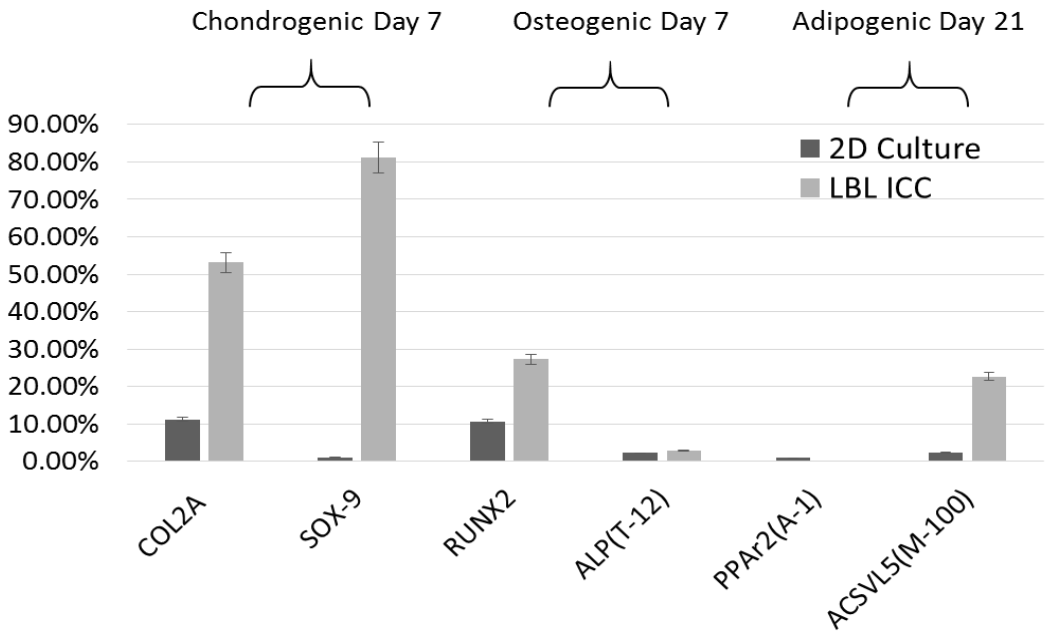

Figure 5.9 Quantitative analysis of expression level with markers of Chondrogenic, Osteogenic and Adipogenic lineages according to immunofluorescence staining images of HS-5 Cells on LBL-modified ICC scaffold coated with 7 bi-layers of PDDA/Clay on Day 7 and day 21. ($P<0.05$)

It was reported largely *in vitro* and *in vivo* osteogenic effects of biomimetic polymer scaffolds on stem cells[50,51]. However, the expression of chondrogenic and osteogenic markers were found related to the location of cells in the porous structure of LBL-modified scaffold. It was noticed that the BMSCs stained with chondrogenic markers, COL2A, were mainly present at the center of the cell plaque (**Figure 5.10a**), whereas cells with osteogenic marker, RUNX2, was predominantly localized at the periphery of the cell plaque or in contact with the clay surface of the pore (**Figure 5.10b**). HS-5 cells often forms a dense "net" of cells after extracted from BMSCs[7,43], which appear to be fibroblastoid and secrete significant

levels of growth factors in traditional 2D cell cultures. In contact with the LBL-modified bone-mimetic surface of scaffolds, osteogenesis of HS-5 cells were promoted. Meanwhile, the center of the cell net could not sense the cues from the environment except the neighbor cells, which promoted chondrogenesis instead.

Quantitative analysis of the counterstaining images for both RUNX-2 and Sox-9 (**Figure 5.10c**) was processed by *ImageJ* to examine the overlap of the two markers. The result indicated large portion of the RUNX-2 positive cells expressed chondrocyte specific markers Sox-9. 21.34±3.2% of HS-5 cells express both markers comparing to 81.2±6.0% chondrocyte-like cells among all the population, and these cells were located in the plaques rather than adhering to the surface of the pore substrate. It was reported RUNX-2 expression in BMSCs can accelerate bone formation in healing of critical-sized defects.[52] Consequently, the increase of expression in center of the HS-5 cell clusters indirectly improve the bone formation in 3D environment although the primary cells in the center have lower chance to contact with physical and chemical cues on the surface.

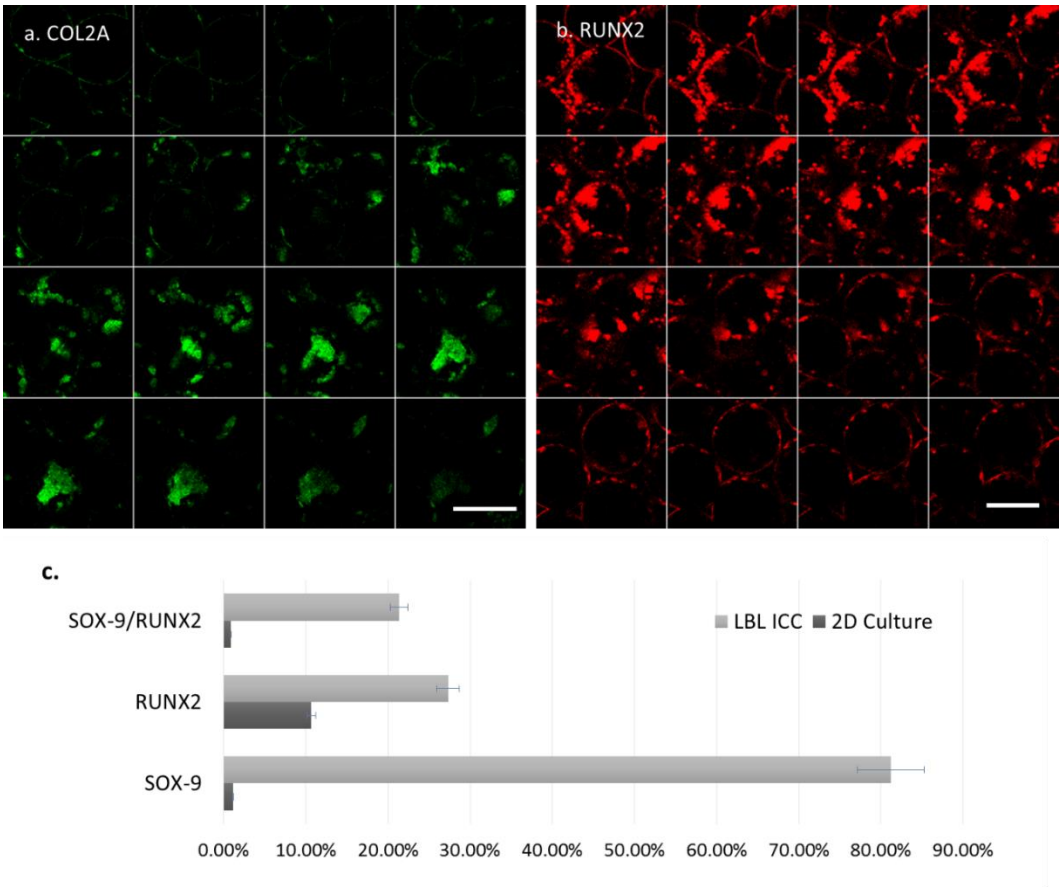

Figure 5.10 Confocal z-stack images of HS-cells aggregates in pores of ICC scaffold cultured were taken every 8µm in depth. Cells were stained with COL2A (**a**) and RUNX2 (**b**) respectively. Scale bar: 100µm.

5.5 Conclusion

The findings reported here indicate that stablished support cells HS-5 line extracted from BMSCs is possible to transit their phenotypes during the culturing within the 3D ICC scaffold with LBL bone mimetic coating of clay and PDDA. This study showed that LBL coating technology applied to 3D tissue engineering matrices, with an appropriate surface and mechanical property, can vary the morphology of cultured BMSCs aggregation and promote chondrogenic differentiation and potentially osteogenic differentiation, at the same time suppressing adipogenic differentiation. In addition, this study provides a scientific basis for creating *in-vitro* bone marrow niches for HSCs with supporting stromal cells, as well as advancing our understanding towards tissue engineering involving BMSCs and surface properties of 3D matrix. LBL surface modification on 3D porous ICC hydrogel scaffolds demonstrated this technique can change the surface ligands and properties of 3D matrices and thereafter control the cell behavior while LBL on 3D structure provides a tool to designing the microenvironment of bone marrow or other stem cells.

5.5 References

(1) Méndez-Ferrer, S.; Michurina, T. V; Ferraro, F.; Mazloom, A. R.; Macarthur, B. D.; Lira, S. A.; Scadden, D. T.; Ma'ayan, A.; Enikolopov, G. N.; Frenette, P. S. Mesenchymal and Haematopoietic Stem Cells Form a Unique Bone Marrow Niche. *Nature* **2010**, *466*, 829–834.

(2) Chan, C. K. F.; Chen, C.-C.; Luppen, C. A.; Kim, J.-B.; DeBoer, A. T.; Wei, K.; Helms, J. A.; Kuo, C. J.; Kraft, D. L.; Weissman, I. L. Endochondral Ossification Is Required for Haematopoietic Stem-Cell Niche Formation. *Nature* **2009**, *457*, 490–494.

(3) Sacchetti, B.; Funari, A.; Michienzi, S.; Di Cesare, S.; Piersanti, S.; Saggio, I.; Tagliafico, E.; Ferrari, S.; Robey, P. G.; Riminucci, M.; *et al.* Self-Renewing Osteoprogenitors in Bone Marrow Sinusoids Can Organize a Hematopoietic Microenvironment. *Cell* **2007**, *131*, 324–336.

(4) Krebsbach, P. H.; Kuznetsov, S. A.; Bianco, P.; Gehron Robey, P. Bone Marrow Stromal Cells: Characterization and Clinical Application. *Crit. Rev. Oral Biol. Med.* **1999**, *10*, 165–181.

(5) Prestwich, G. D.; Healy, K. E. Why Regenerative Medicine Needs an Extracellular Matrix. *Expert Opin. Biol. Ther.* **2015**, *15*, 3–7.

(6) *Biomaterials Surface Science*; Taubert, A.; Mano, J. F.; Rodríguez-Cabello, J. C., Eds.; Wiley-VCH Verlag GmbH & Co. KGaA: Weinheim, Germany, 2013.

(7) Roecklein, B. A.; Torok-Storb, B. Functionally Distinct Human Marrow Stromal Cell Lines Immortalized by Transduction with the Human Papilloma Virus E6/E7 Genes. *Blood* **1995**, *85*, 997–1005.

(8) Morrison, S. J.; Scadden, D. T. The Bone Marrow Niche for Haematopoietic Stem Cells. *Nature* **2014**, *505*, 327–334.

(9) Azab, F.; Muz, B.; Vij, R.; Azab, A. K. Autologous 3D Tissue-Engineered

Bone Marrow For Drug Screening In MM Patients. *Blood* **2013**, *122*, 132.

(10) Torisawa, Y.; Spina, C. S.; Mammoto, T.; Mammoto, A.; Weaver, J. C.; Tat, T.; Collins, J. J.; Ingber, D. E. Bone Marrow-on-a-Chip Replicates Hematopoietic Niche Physiology in Vitro. *Nat. Methods* **2014**, *11*, 663–669.

(11) Pittenger, M. F. Multilineage Potential of Adult Human Mesenchymal Stem Cells. *Science (80-.).* **1999**, *284*, 143–147.

(12) Prockop, D. J. Marrow Stromal Cells as Stem Cells for Nonhematopoietic Tissues. *Science (80-.).* **1997**, *276*, 71–74.

(13) Prockop, D. J. Marrow Stromal Cells as Stem Cells for Continual Renewal of Nonhematopoietic Tissues and as Potential Vectors for Gene Therapy. *J. Cell. Biochem.* **1998**, *72*, 284–285.

(14) Lee, J.; Abdeen, A. A.; Tang, X.; Saif, T. A.; Kilian, K. A. Geometric Guidance of Integrin Mediated Traction Stress during Stem Cell Differentiation. *Biomaterials* **2015**, *69*, 174–183.

(15) Gao, L.; McBeath, R.; Chen, C. S. Stem Cell Shape Regulates a Chondrogenic versus Myogenic Fate through Rac1 and N-Cadherin. *Stem Cells* **2010**, *28*, 564–572.

(16) Mackay, A. M.; Beck, S. C.; Murphy, J. M.; Barry, F. P.; Chichester, C. O.; Pittenger, M. F. Chondrogenic Differentiation of Cultured Human Mesenchymal Stem Cells from Marrow. *Tissue Eng.* **1998**, *4*, 415–428.

(17) Belnoue, E.; Tougne, C.; Rochat, A.-F.; Lambert, P.-H.; Pinschewer, D. D.; Siegrist, C.-A. Homing and Adhesion Patterns Determine the Cellular Composition of the Bone Marrow Plasma Cell Niche. *J. Immunol.* **2012**, *188*, 1283–1291.

(18) Tutak, W.; Sarkar, S.; Lin-Gibson, S.; Farooque, T. M.; Jyotsnendu, G.; Wang, D.; Kohn, J.; Bolikal, D.; Simon, C. G. The Support of Bone Marrow Stromal Cell Differentiation by Airbrushed Nanofiber Scaffolds.

Biomaterials **2013**, *34*, 2389–2398.

(19) Rosa, N.; Simoes, R.; Magalhães, F. D.; Marques, A. T. From Mechanical Stimulus to Bone Formation: A Review. *Med. Eng. Phys.* **2015**, *37*, 719–728.

(20) Pattabhi, S. R.; Lehaf, A. M.; Schlenoff, J. B.; Keller, T. C. S. Human Mesenchymal Stem Cell Osteoblast Differentiation, ECM Deposition, and Biomineralization on PAH/PAA Polyelectrolyte Multilayers. *J. Biomed. Mater. Res. A* **2015**, *103*, 1818–1827.

(21) Parekh, S. H.; Chatterjee, K.; Lin-Gibson, S.; Moore, N. M.; Cicerone, M. T.; Young, M. F.; Simon, C. G. Modulus-Driven Differentiation of Marrow Stromal Cells in 3D Scaffolds That Is Independent of Myosin-Based Cytoskeletal Tension. *Biomaterials* **2011**, *32*, 2256–2264.

(22) Cheung, W.-C.; Van Ness, B. The Bone Marrow Stromal Microenvironment Influences Myeloma Therapeutic Response in Vitro. *Leukemia* **2001**, *15*, 264–271.

(23) Civini, S.; Jin, P.; Ren, J.; Sabatino, M.; Castiello, L.; Jin, J.; Wang, H.; Zhao, Y.; Marincola, F.; Stroncek, D. Leukemia Cells Induce Changes in Human Bone Marrow Stromal Cells. *J. Transl. Med.* **2013**, *11*, 298.

(24) Di Maggio, N.; Piccinini, E.; Jaworski, M.; Trumpp, A.; Wendt, D. J.; Martin, I. Toward Modeling the Bone Marrow Niche Using Scaffold-Based 3D Culture Systems. *Biomaterials* **2011**, *32*, 321–329.

(25) Miyoshi, H.; Ohshima, N.; Sato, C. Three-Dimensional Culture of Mouse Bone Marrow Cells on Stroma Formed within a Porous Scaffold: Influence of Scaffold Shape and Cryopreservation of the Stromal Layer on Expansion of Haematopoietic Progenitor Cells. *J. Tissue Eng. Regen. Med.* **2013**, *7*, 32–38.

(26) Brennan, M. Á.; Renaud, A.; Gamblin, A.; D'Arros, C.; Nedellec, S.; Trichet, V.; Layrolle, P. 3D Cell Culture and Osteogenic Differentiation of Human Bone Marrow Stromal Cells Plated onto Jet-Sprayed or Electrospun Micro-Fiber Scaffolds. *Biomed. Mater.* **2015**, *10*, 045019.

(27) TANG, Z.; WANG, Y.; PODSIADLO, P.; KOTOV, N. A. Biomedical Applications of Layer-by-Layer Assembly : From Biomimetics to Tissue Engineering. *Adv. Mater. 18*, 3203–3224.

(28) Costa, R. R.; Custódio, C. A.; Arias, F. J.; Rodríguez-Cabello, J. C.; Mano, J. F. Layer-by-Layer Assembly of Chitosan and Recombinant Biopolymers into Biomimetic Coatings with Multiple Stimuli-Responsive Properties. *Small* **2011**, *7*, 2640–2649.

(29) Seliktar, D. Designing Cell-Compatible Hydrogels for Biomedical Applications. *Science* **2012**, *336*, 1124–1128.

(30) Shalumon, K. T.; Chennazhi, K. P.; Nair, S. V.; Jayakumar, R. High Thick Layer-by-Layer 3D Multiscale Fibrous Scaffolds for Enhanced Cell Infiltration and It's Potential in Tissue Engineering. *J. Biomed. Nanotechnol.* **2013**, *9*, 2117–2122.

(31) Soman, P.; Kelber, J. A.; Lee, J. W.; Wright, T. N.; Vecchio, K. S.; Klemke, R. L.; Chen, S. Cancer Cell Migration within 3D Layer-by-Layer Microfabricated Photocrosslinked PEG Scaffolds with Tunable Stiffness. *Biomaterials* **2012**, *33*, 7064–7070.

(32) Tang, Z.; Kotov, N. A.; Magonov, S.; Ozturk, B. Nanostructured Artificial Nacre. *Nat. Mater.* **2003**, *2*, 413–418.

(33) Lee, J.; Kotov, N. A. Notch Ligand Presenting Acellular 3D Microenvironments for Ex Vivo Human Hematopoietic Stem-Cell Culture Made by Layer-by-Layer Assembly. *Small* **2009**, *5*, 1008–1013.

(34) Nichols, J. E.; Cortiella, J.; Lee, J.; Niles, J. A.; Cuddihy, M.; Wang, S.; Bielitzki, J.; Cantu, A.; Mlcak, R.; Valdivia, E.; *et al.* In Vitro Analog of Human Bone Marrow from 3D Scaffolds with Biomimetic Inverted Colloidal Crystal Geometry. *Biomaterials* **2009**, *30*, 1071–1079.

(35) Foster, N. C.; Henstock, J. R.; Reinwald, Y.; El Haj, A. J. Dynamic 3D Culture: Models of Chondrogenesis and Endochondral Ossification. *Birth*

Defects Res. C. Embryo Today **2015**, *105*, 19–33.

(36) Lefrebvre, V.; de Crombrugghe, B. Toward Understanding S0X9 Function in Chondrocyte Differentiation. *Matrix Biol.* **1998**, *16*, 529–540.

(37) Shui, C.; Spelsberg, T. C.; Riggs, B. L.; Khosla, S. Changes in Runx2/Cbfa1 Expression and Activity during Osteoblastic Differentiation of Human Bone Marrow Stromal Cells. *J. Bone Miner. Res.* **2003**, *18*, 213–221.

(38) Fujita, T.; Azuma, Y.; Fukuyama, R.; Hattori, Y.; Yoshida, C.; Koida, M.; Ogita, K.; Komori, T. Runx2 Induces Osteoblast and Chondrocyte Differentiation and Enhances Their Migration by Coupling with PI3K-Akt Signaling. *J. Cell Biol.* **2004**, *166*, 85–95.

(39) Tsai, M.-T.; Li, W.-J.; Tuan, R. S.; Chang, W. H. Modulation of Osteogenesis in Human Mesenchymal Stem Cells by Specific Pulsed Electromagnetic Field Stimulation. *J. Orthop. Res.* **2009**, *27*, 1169–1174.

(40) Ren, D. PPARgamma Knockdown by Engineered Transcription Factors: Exogenous PPARgamma 2 but Not PPARgamma 1 Reactivates Adipogenesis. *Genes Dev.* **2002**, *16*, 27–32.

(41) Hall, J. A.; Ribich, S.; Christoffolete, M. A.; Simovic, G.; Correa-Medina, M.; Patti, M. E.; Bianco, A. C. Absence of Thyroid Hormone Activation during Development Underlies a Permanent Defect in Adaptive Thermogenesis. *Endocrinology* **2010**, *151*, 4573–4582.

(42) Podsiadlo, P.; Qin, M.; Cuddihy, M.; Zhu, J.; Critchley, K.; Kheng, E.; Kaushik, A. K.; Qi, Y.; Kim, H.-S.; Noh, S.-T.; *et al.* Highly Ductile Multilayered Films by Layer-by-Layer Assembly of Oppositely Charged Polyurethanes for Biomedical Applications. *Langmuir* **2009**, *25*, 14093–14099.

(43) Graf, L. Gene Expression Profiling of the Functionally Distinct Human Bone Marrow Stromal Cell Lines HS-5 and HS-27a. *Blood* **2002**, *100*, 1509–1511.

(44) Thompson, M. T.; Berg, M. C.; Tobias, I. S.; Rubner, M. F.; Van Vliet, K. J. Tuning Compliance of Nanoscale Polyelectrolyte Multilayers to Modulate Cell Adhesion. *Biomaterials* **2005**, *26*, 6836–6845.

(45) Bianco, P.; Riminucci, M.; Gronthos, S.; Robey, P. G. Bone Marrow Stromal Stem Cells: Nature, Biology, and Potential Applications. *Stem Cells* **2001**, *19*, 180–192.

(46) Collins, C. A.; Olsen, I.; Zammit, P. S.; Heslop, L.; Petrie, A.; Partridge, T. A.; Morgan, J. E. Stem Cell Function, Self-Renewal, and Behavioral Heterogeneity of Cells from the Adult Muscle Satellite Cell Niche. *Cell* **2005**, *122*, 289–301.

(47) Reya, T.; Morrison, S. J.; Clarke, M. F.; Weissman, I. L. Stem Cells, Cancer, and Cancer Stem Cells. *Nature* **2001**, *414*, 105–111.

(48) Weissman, I. L. Translating Stem and Progenitor Cell Biology to the Clinic: Barriers and Opportunities. *Science (80-.).* **2000**, *287*, 1442–1446.

(49) Tetteh, E. S.; Bajaj, S.; Ghodadra, N. S. Basic Science and Surgical Treatment Options for Articular Cartilage Injuries of the Knee. *J. Orthop. Sports Phys. Ther.* **2012**, *42*, 243–253.

(50) Ko, E.; Cho, S.-W. Biomimetic Polymer Scaffolds to Promote Stem Cell-Mediated Osteogenesis. *Int. J. stem cells* **2013**, *6*, 87–91.

(51) Shekaran, A.; García, A. J. Extracellular Matrix-Mimetic Adhesive Biomaterials for Bone Repair. *J. Biomed. Mater. Res. Part A* **2011**, *96A*, 261–272.

(52) Wojtowicz, A. M.; Templeman, K. L.; Hutmacher, D. W.; Guldberg, R. E.; García, A. J. Runx2 Overexpression in Bone Marrow Stromal Cells Accelerates Bone Formation in Critical-Sized Femoral Defects. *Tissue Eng. Part A* **2010**, *16*, 2795–2808.

Chapter VI

Suggested Future Directions and Conclusion

6.1. Suggested future directions

6.1.1. Direction for 3D cell culture model

The size of the cellular spheroids in 3D cell culture used in this dissertation work was selected as the diffusion limit of oxygen in tissues is around 150-200μm[1]. Therefore, cells within spheroids in the model here are not expected to suffer from hypoxia. However, as a tumor grows to a detectable size, its central region usually contains only dead cells. This central region of dead cells is called necrotic core of the tumor[2,3,4] (**Figure 6.1**). This properties of the tumor structure regarding to size of tumor growth shall also change the distribution and penetration of drugs including the nanomedicines due to the different status of cell activities, whereas

the preliminary result of Chapter 4 has shown that size-controlled cellular spheroids range from 100 to 400μm are an adequate model for studying the process of NP transport deep into the different types of tumor.

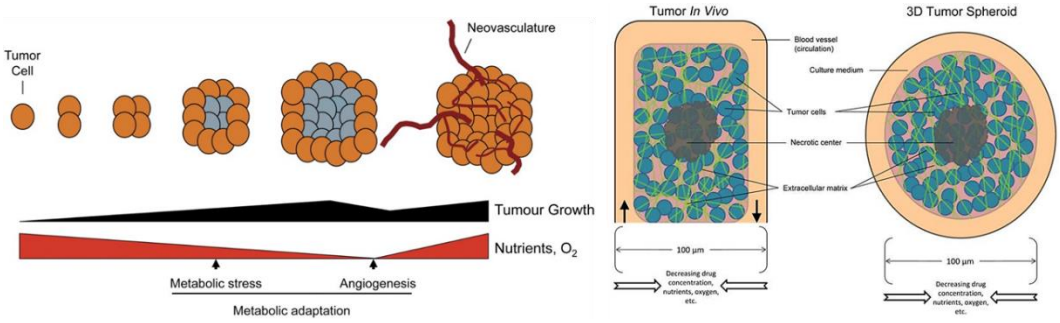

Figure 6.1 Metabolic adaptation of tumor growth as penetration of oxygen and nutrients decrease in the core of tumor. The necrotic center can be formed when the size of tumor spheroid are above 200μm in diameter.[2,4]

In another aspect, the liver carcinoma cell line used in the primary experiments for NP transport study has the limitation to mimic the real human primary tissue. In the future work, the study and validation of NP transport properties shall be implemented in personalized and human-derived cells and tissue. The stem cell culture with sized-controlled EBs successfully incorporated with ICC scaffold and LBL technique have shown in chapter 4 and 5, which can be used for NP transport in human related and patient-specific tumor tissue, and expected to demonstrate unique properties for individual patients and more accurate comparing to *in vivo* animal studies.

6.1.2. Direction for simulation study

The random walk model to study the NP transport as two-phase diffusion in chapter 3 is simplified based on the assumption of equilibrium condition in experimental framework. However, to generalized the model for application of other NPs with higher or faster binding/unbinding activity by cells in the spheroids, this model shall be consist of the transition state such as cell membrane binding and uptake[5,6]. This is essential for targeted NP transport after extravasation. The increase possibility of this transition interrupt the diffusion process and create a diffusion barrier at the out layer of the tissue/tumor, which slows down the apparent diffusivity $\boldsymbol{D_a}$ and results in poor distribution of nanomedicines[7,8]. The simulated structure of spheroids was simulated by the perfect spheres packed in 3D although the cells in the tissue are packed tighter and with uniform intercellular space. Therefore, the structure can be represented in the future study by Voronoi geometries[9] without large pores in 3D domain to improve the accuracy.

6.1.3. Direction for estimation of NP transport in the framework

This frame work can be applied and generalized for other NPs for the diffusion studies. Understanding the effect of charge, size and shape of NPs on diffusion processes in tissues represents an essential part of this project. In the future work, CNTs with a different charge using variation of positively, neutral and negatively charged organic capping agents/stabilizers should be tested to better understand the detailed fundamental mechanism of transport. Shape of NPs can

potentially be a fascinating parameter to vary in respect of permeation studies. Comparison of permeation of graphene NPs (**Figure 6.2**) with small size and aspect ratio will be compared to permeation of CNTs. Surface modification of graphene and carbon nanoparticles can be accomplished the same way as that for CNTs. Moreover, the affinity of NPs with cell membrane influences the transport essencially according to the study in this dissertation. Chiral graphene quantum dots (GQDs) covalent attached with L/D-cysteine moieties to the edges are the potential candidate as the positive control for the framework. The conjugation of L/D-cysteine to GQDs leads to their helical buckling due to chiral interactions at the edges. The preliminary study demonstrated that GQD enantiomer with the left twist has stronger tendency to accumulate within the cellular membrane than the opposite enantiomer. Thereby, although L/D-GQDs has the same core materials and surface ligands, they shall have different diffusivity through cellular spheroid.

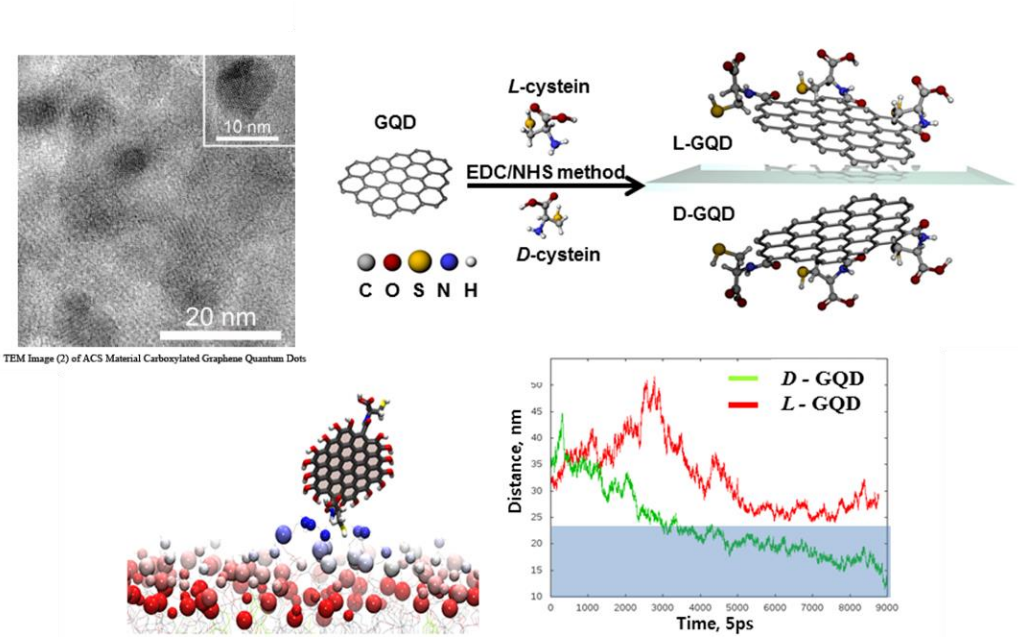

Figure 6.2 TEM images of GQDs and the preliminary data of L/D-cysteine conjugated GQDs interacted with cell membrane by molecular simulation.

6.1.4. Direction for clinical use of targeted CNTs

The management of intraocular tumors include systemic treatments such as external beam radiotherapy, systemic or intra-arterial chemotherapy, and local treatments such as local plaque radiotherapy, removal of eye or in selected cases, laser photocoagulation.[10,11] Recently, intravitreal chemotherapy injection was used in the treatment of selected intraocular tumors such as retinoblastoma or vitreoretinal lymphoma.[12] However, one of the main reason for failure of main retinal tumor response in vitreous is drug penetration. Therefore, drug carriers which are capable of deep and fast penetration through all retinal layers as well as internal limiting membrane are much needed.

Diffusional transport of targeted CNTs was found surprisingly high in the chapter 2 and 3. This anomalous trend is attributed to the planar diffusion of CNTs along cellular membranes reducing effective dimensionality of diffusional space. Preliminary result (**Figure 6.3**) shows CNT conjugated with epithelial cell-specific vitamin, Biotin, (0.1mg/ml) can penetrate through the thick tumor layer of mice after injection for 24 h and access the bottom layer of the eyes where it was targeted. This property of CNT with selected targeting ligand is promising candidate for local injection treatment for intraocular tumors. Intraocular tumors are life-threatening cancers that affect every age. They mostly affect choroidal layer, but the others intraocular layers including ciliary body, iris and retinal layers.

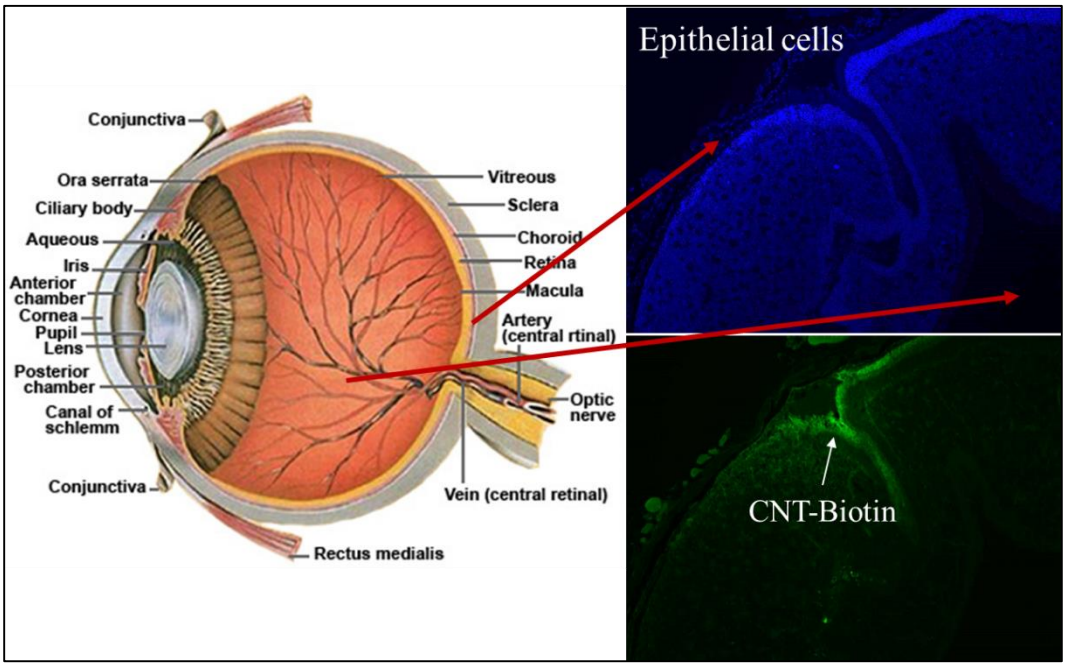

Figure 6.3 Eye structure (Left) and fluorescent images (Right) show the targeted CNT-Biotin (Green) penetrated through tumor cells (Blue) and reached the epithelial cells.

6.2. Concluding remarks

This dissertation mainly focuses on development and establishment of the experimental and conceptual framework for quantitative evaluation of NP transport in the tumor mass using 3D cell culture *ex vivo* and mathematical simulation. The most important achievement was developing a distinctive platform, 3D cellular spheroid culture in ICC scaffolds and further establishing this platform with computer-aided quantification and simulation as a reference system. In addition, this work was successfully extended to size-controlled standardized stem cellular spheroid culture model and further potentially utilized as an *ex-vivo* platform for human-related and patient-specific nanomedicine characterization and transport study.

Firstly, this work started with utilizing the 3D cell culture and looking for the suitable models for NP transport study as the experimental framework. This experimental model based on 3D liver carcinoma cellular spheroids culture demonstrated promising potential of this research with an increase in complexity of structure and functions at closer replication of human tissues, high uniformity for standardized data and high transparency for monitoring NP transport in real time with high-resolution imaging equipment. The quantification of CNT transport extracted from experimental framework contribute tremendously to the finding of the fundamental mechanisms of NP transport in tumor tissue.

Secondly, improvements have been made in fundamental understanding of the mechanisms of transport in tumor tissues. Systematic and quantitative investigation have developed the approach to standardize the comparable parameter as apparent diffusion coefficients. As such, the fast diffusion of targeted CNT was found in chapter 3 contributing to lateral diffusion on cell membrane based on the concept of Monte-Carlo simulation of two-phase diffusion in interstitial space and cell membrane of tumor tissues. The simulated model with measurable inputs of interstitial and membrane diffusion coefficients, equilibrium distribution coefficient and patient/disease-specific tumor volume ratios, provided a powerful tool for prediction and support as a conceptual framework.

In addition, improvement of 3D cell culture models have been made towards the patient-specific and personalized screening because the transport process was highly influenced by cellular membrane interaction with the nanomedicine. Stem cell culture have been applied to the experimental models to create a platform for personalized drug screening, as well as the size-controlled technology by ICC scaffolds fabrication will also provide the promising platform to study the transport of NP at the different stage of tumor spheroids with/without necrotic cores. Layer-by-layer 3D modification of this cell culture models allows more diversity of stem cells culture required supporting cells such as bone marrow stromal cells.

Last but not least, my work on these fundamental behaviors of NPs in human tissues/tumors in an aspect of experimental and computational simulation

make the first steps toward purposeful engineering of NPs for desired depth of tissue penetration. This research carry a significant impact on different fields of knowledge from nanomaterials to biomedical engineering and pharmaceutical science. I hope the overall framework of NP transport evaluation in my work can significantly contribute to the improvement of the application of nanotechnologies to nanomedicine for cancer treatment and human health.

6.3 References

(1) Harris, A. L. Hypoxia--a Key Regulatory Factor in Tumour Growth. *Nat. Rev. Cancer* **2002**, *2*, 38–47.

(2) Rapid Generation of In Vitro Multicellular Spheroids for the Study of Monoclonal Antibody Therapy http://jcancer.org/v02p0507.htm (accessed Nov 12, 2015).

(3) Cui, S. FORMATION OF NECROTIC CORES IN THE GROWTH OF TUMORS: ANALYTIC RESULTS. *Acta Math. Sci.* **2006**, *26*, 781–796.

(4) Jones, R. G.; Thompson, C. B. Tumor Suppressors and Cell Metabolism: A Recipe for Cancer Growth. *Genes Dev.* **2009**, *23*, 537–548.

(5) Xu, X.; Ho, W.; Zhang, X.; Bertrand, N.; Farokhzad, O. Cancer Nanomedicine: From Targeted Delivery to Combination Therapy. *Trends Mol. Med.* **2015**, *21*, 223–232.

(6) Sanna, V.; Pala, N.; Sechi, M. Targeted Therapy Using Nanotechnology: Focus on Cancer. *Int. J. Nanomedicine* **2014**, *9*, 467–483.

(7) Current Approaches for Improving Intratumoral Accumulation and Distribution of Nanomedicines http://www.thno.org/v05p1007.htm (accessed Nov 22, 2015).

(8) Chauhan, V. P.; Jain, R. K. Strategies for Advancing Cancer Nanomedicine. *Nat. Mater.* **2013**, *12*, 958–962.

(9) Yong, Y.; Lou, X.; Li, S.; Yang, C.; Yin, X. Direct Simulation of the Influence of the Pore Structure on the Diffusion Process in Porous Media. *Comput. Math. with Appl.* **2014**, *67*, 412–423.

(10) Gaudreault, J.; Fei, D.; Beyer, J. C.; Ryan, A.; Rangell, L.; Shiu, V.; Damico, L. A. Pharmacokinetics and Retinal Distribution of Ranibizumab, a Humanized Antibody Fragment Directed against VEGF-A, Following Intravitreal Administration in Rabbits. *Retina 27*, 1260–1266.

(11) Mordenti, J.; Cuthbertson, R. A.; Ferrara, N.; Thomsen, K.; Berleau, L.; Licko, V.; Allen, P. C.; Valverde, C. R.; Meng, Y. G.; Fei, D. T.; *et al.* Comparisons of the Intraocular Tissue Distribution, Pharmacokinetics, and Safety of 125I-Labeled Full-Length and Fab Antibodies in Rhesus Monkeys Following Intravitreal Administration. *Toxicol. Pathol. 27*, 536–544.

(12) Heiduschka, P.; Fietz, H.; Hofmeister, S.; Schultheiss, S.; Mack, A. F.; Peters, S.; Ziemssen, F.; Niggemann, B.; Julien, S.; Bartz-Schmidt, K. U.; *et al.* Penetration of Bevacizumab through the Retina after Intravitreal Injection in the Monkey. *Invest. Ophthalmol. Vis. Sci.* **2007**, *48*, 2814–2823.